



HAL
open science

Low-Earth-Orbit satellite communications using LoRa-like signals

Mohamed Amine Ben Temim

► **To cite this version:**

Mohamed Amine Ben Temim. Low-Earth-Orbit satellite communications using LoRa-like signals. Networking and Internet Architecture [cs.NI]. Université de Bordeaux, 2022. English. NNT : 2022BORD0089 . tel-03723714

HAL Id: tel-03723714

<https://theses.hal.science/tel-03723714>

Submitted on 15 Jul 2022

HAL is a multi-disciplinary open access archive for the deposit and dissemination of scientific research documents, whether they are published or not. The documents may come from teaching and research institutions in France or abroad, or from public or private research centers.

L'archive ouverte pluridisciplinaire **HAL**, est destinée au dépôt et à la diffusion de documents scientifiques de niveau recherche, publiés ou non, émanant des établissements d'enseignement et de recherche français ou étrangers, des laboratoires publics ou privés.



THÈSE PRÉSENTÉE
POUR OBTENIR LE GRADE DE

**DOCTEUR DE
L'UNIVERSITÉ DE BORDEAUX**

ÉCOLE DOCTORALE : SCIENCES PHYSIQUES ET DE L'INGÉNIEUR

SPÉCIALITÉ : AUTOMATIQUE, PRODUCTIQUE, SIGNAL ET IMAGE

Par **Mohamed Amine Ben Temim**

**Low-Earth-Orbit satellite communications using
LoRa-like signals**

Soutenue le 21 mars 2022

Membres du jury :

Mme	Karine Amis	Professeur IMT Atlantique	Rapporteur
M.	Olivier Berder	Professeur ENSSAT Lannion	Rapporteur
M.	Yves Louet	Professeur Centrale-Supélec Rennes	Examineur
M.	Guillaume Ferré	Maître de conférence - HDR Bordeaux INP	Directeur de Thèse
M.	Toufik Ahmed	Professeur Bordeaux INP	Co-directeur de Thèse
M.	Romain Tajan	Maître de conférence Bordeaux INP	Co-encadrant

Acknowledgements

First of all, I would like to thank my advisor, Dr. Guillaume Ferré, who believed in me and gave me the opportunity to perform my PhD at the IMS laboratory and Bordeaux university. I deeply admire his ability to provide new paths to solve problems that seem insurmountable, as well as his ability to create an environment where people feel so comfortable to live and work in. I feel very lucky to have him as an advisor. I also would like to thank my co-advisor Dr. Romain Tajan for his great guidance and good friendship all these years.

I would like to thank as well Prof. Yves Louet for acting as the president of my PhD jury, Prof. Karine Amis and Prof. Olivier Berder for serving as external examiners. Their comments and feedback improved the quality of this manuscript.

I would like to thank all the friends that directly or indirectly became part of my PhD studies, mainly in France and Tunisia. Without them my PhD studies would not have been so colorful. Special thanks to all the friends with whom we shared lunch and coffee breaks at the IMS laboratory all these years.

Finally, I would like express my sincere gratitude to my parents, Fawzi and Henda, as well as my sisters, Asma and Eya, and my brother Oussama, for supporting me and all my decisions throughout this long journey.

Title — Low-Earth-Orbit satellite communications using LoRa-like signals

Abstract — Connecting a device to the Internet is nowadays possible through several communication technologies. However, a limited area of the planet is currently connectable to the Internet via terrestrial cellular networks. Therefore, with the development of satellite Internet of Things (IoT) in recent years, it is possible to provide reliable communication services for the places where there is no terrestrial networks. Thus, satellite IoT is very ambitious sector allowing to blanketing the Earth with reliable and ubiquitous coverage. In terms of power, propagation delay and coverage, low-Earth orbit (LEO) satellites are more suitable for IoT communications than other types of satellites.

LEO satellite communications are currently facing two major challenges. The first one stems from their high speed yielding to significant Doppler effects. The second challenge is the huge number of devices that could be connected to the latter satellites due to their field of view (FoV), which leads to high probability of packet collisions. In this thesis, we deal with IoT communications with LEO satellites using low power wide area (LPWA) technologies in unlicensed bands. Typically, we focused on LoRa-like communications using chirp-based waveforms. On one hand, our first contribution is to propose several synchronization algorithms allowing to accurately decode LoRa-like signals received with random arrival times and with significant Doppler effects especially the Doppler time-variation. On the other hand, for energy efficiency reasons, most of LPWA technologies in unlicensed bands adopt uncoordinated channel access schemes which leads to an increase in the probability of packet collisions, given the huge number of objects that can be connected to a LEO satellite. Thereby, our second major contribution consists in proposing novel approaches to decode interfering LoRa-like signals in uplink and downlink contexts, based on the successive interference cancellation (SIC) algorithm.

Keywords — Internet of Things, Low Power Wide Area Network, LoRa, CSS, DCSS, low-Earth orbit satellite, Synchronization, Doppler effects, Collision.

Résumé des travaux de la thèse

Actuellement, les entreprises ont des activités dans le monde entier, et le nombre de leurs actifs se trouvent dans des zones isolées où la connectivité est extrêmement limitée. Elles ont donc besoin d'échanger des données pour connecter leurs ressources et recevoir un retour d'information le plus rapidement possible afin de maintenir le bon déroulement de leurs opérations. Pour relever ces défis, la plupart des entreprises utilisent des infrastructures de réseaux terrestres sans fil, qui permettent de connecter des appareils utilisant plusieurs technologies de communication. Cependant, l'utilisation de ces réseaux n'est pas une solution optimale pour assurer une connectivité à l'échelle mondiale, en particulier dans les zones isolées, où l'infrastructure cellulaire est très limitée. En effet, les réseaux terrestres ne couvrent que 15% de la surface de la Terre [1]. Les stations de base et les passerelles ne peuvent tout simplement pas être déployées à travers les océans, les déserts ou les sommets des montagnes, et elles ne sont pas assez rentables pour être installées dans des zones éloignées et peu peuplées. Par exemple, il est impossible de garder un œil sur un conteneur expédié de la Chine vers les États-Unis via les réseaux cellulaires classiques.

Compte tenu de la nécessité de connecter des objets partout dans le monde, on assiste actuellement à l'émergence de la connectivité de l'Internet des objets (IoT pour Internet of Things en anglais) via des satellites. Cette solution permettrait de connecter théoriquement toute la surface de la Terre. Ces dernières années, plusieurs projets dans le domaine de l'IoT par satellite ont été réalisés. Par exemple, Swarm [2] utilise la technologie IoT LoRa [3] dans sa constellation de satellites en orbite terrestre basse (LEO pour low-Earth orbit en anglais) [4], et Eutelsat [1] a lancé plusieurs nano-satellites pour servir les applications IoT génériques de Sigfox [5] [6]. De nombreux projets industriels utilisent des Low Power Wide Area networks (LPWANs) afin d'établir des communications IoT avec des satellites LEO. Le choix de ces derniers réseaux IoT se justifie par leur capacité à établir des communications à très longue portée, tout en maintenant une faible consommation d'énergie des noeuds, ce qui semble être une solution très intéressante pour atteindre une connectivité globale via des satellites LEO. De plus, en termes de puissance transmise, de délai de propagation et de couverture, les satellites LEO sont plus adaptés aux communications LPWAN que les autres types de satellites. Par con-

séquent, nous étudions dans cette thèse plusieurs aspects des communications LPWAN avec les satellites LEO et nous nous concentrons sur l'amélioration de la couche PHY LoRa afin de faire face aux exigences de ces dernières communications.

Dans la suite de cette introduction, nous discuterons de quelques généralités et des exigences des communications LPWAN en utilisant des satellites LEO, et nous présenterons les contributions et le plan de la thèse.

Communications LPWAN par des satellites LEO

L'Internet des objets ou l'IoT est l'interconnexion entre l'internet et des objets, des lieux et des environnements physiques. L'appellation désigne un nombre croissant d'objets connectés à internet permettant ainsi une communication entre nos biens dits physiques et leurs existences numériques. Dans quelques années, un grand nombre des appareils que nous utilisons dans notre vie quotidienne seront connectés à l'internet via des technologies IoT. En effet, le nombre d'objets connectés a considérablement augmenté ces dernières années, et devrait croître encore plus rapidement dans les années à venir [7, 8]. Comme on peut l'imaginer, les applications des réseaux IoT sont innombrables. Elles englobent les applications de villes intelligentes, la surveillance de l'agriculture, la surveillance de la santé, les compteurs intelligents, la localisation et le suivi, la logistique, etc [1, 9].

De nombreuses applications IoT entrent dans la catégorie des transmissions à faible débit, telles que des relevés de température, d'humidité et de pression, à intervalles réguliers. Compte tenu de cette connectivité massive qui ne fait pas appel à des réseaux à haut débit, nous avons assisté au cours de la dernière décennie à l'émergence des LPWANs. Comme son nom l'indique, les LPWANs doivent permettre aux terminaux de transmettre de manière autonome sur de longues distances et pendant de nombreuses années. Pour atteindre ce dernier objectif, des protocoles de transmission à très faible puissance sont utilisés. En effet, la majorité des LPWANs déploient des protocoles de transmission basés sur des schémas d'accès aléatoires aux canaux de fréquence, tels que le protocole ALOHA. En offrant une connectivité massive à longue portée, les LPWANs pourraient être de bons candidats pour les communications par satellite LEO.

Néanmoins, afin d'établir des communications fiables avec les satellites LEO, la technologie sans fil déployée doit répondre à plusieurs exigences. En effet, l'un des principaux défis d'une telle communication est la présence des effets Doppler importants dus à la vitesse élevée de ces satellites. Ces effets Doppler induisent un décalage de la fréquence porteuse entre l'émetteur et le récepteur. Dans le cas des LPWANs, qui sont considérés dans cette thèse, l'effet Doppler le plus gênant est celui qui varie dans le temps pendant la durée du paquet. Étant donné le faible débit de données utilisé dans les LPWANs, qui donne lieu à de longs paquets, et la vitesse élevée de la variation Doppler (plusieurs centaines de Hz/s), il est très probable que cette variation ait

un impact significatif sur la démodulation de ces paquets.

Le deuxième défi majeur de ces communications est le nombre massif d'objets qui peuvent être connectés à un satellite LEO, en raison de son champ de vision. Cette connectivité massive entraîne des collisions de paquets très probables, en particulier si l'on tient compte des schémas d'accès au canal non coordonnés, tels qu'ils sont déployés par la majorité des LPWANs. Ces techniques d'accès aléatoire sont déployées pour réduire la consommation d'énergie des noeuds. En outre, étant donné que LoRa, comme la majorité des LPWANs, utilise les bandes de fréquences industrielles, scientifiques et médicales (ISM) sans licence, il devrait faire face à la collision de paquets provenant de noeuds utilisant d'autres technologies, comme Sigfox, qui effectue des communications à bande ultra étroite (UNB pour ultra narrow band en anglais). De plus, les signaux de plusieurs noeuds LoRa peuvent être reçus simultanément sur la même bande de fréquence, ce qui pourrait créer des collisions destructives. Ainsi, les collisions de paquets, générées par des noeuds utilisant la même technologie ou des technologies différentes, est un problème majeur lorsqu'on envisage l'IoT par satellite via les technologies LPWAN.

Dans cette thèse, nous considérons l'une des technologies LPWAN sans licence les plus populaires, à savoir LoRa. LoRa utilise la modulation à spectre étalé chirpé (CSS pour chirp spread spectrum en anglais) pour atteindre une connectivité à longue portée et une résilience au bruit et aux interférences à bande étroite. Les contributions de cette thèse consistent principalement à traiter les deux problèmes mentionnés ci-dessus dans le contexte de communications de type LoRa avec des satellites LEO.

Contributions et plan de la thèse

Les contributions de la thèse sont les suivantes :

1. Une étude de l'impact des désynchronisations de temps et de fréquence sur l'estimation des symboles LoRa en cas de communication avec un satellite LEO.
2. Une modification de la couche PHY LoRa pour être plus robuste aux erreurs de synchronisation en temps et en fréquence, en particulier celui causé par la variation du Doppler. La couche PHY proposée est basée sur la mise en oeuvre d'un processus différentiel.
3. Un premier émetteur-récepteur basé sur la couche PHY 2/ combinée avec un algorithme de synchronisation original permettant de décoder des signaux de type LoRa en présence d'effets Doppler importants. L'émetteur-récepteur proposé serait donc un bon candidat pour les communications par satellite LEO.
4. Un deuxième émetteur-récepteur basé sur la couche PHY 2/ combinée avec une synchronisation temporelle classique et à l'utilisation d'une forme d'onde non-chirpée dans le

préambule. La forme d'onde proposée est insensible à la variation temporelle de la phase et, par conséquent, la synchronisation temporelle peut être effectuée indépendamment des décalages de fréquence. Ainsi, cette approche permet de profiter de la robustesse de la couche PHY 2/ aux décalages de fréquence, et peut donc être déployée pour communiquer avec les satellites LEO.

5. Une étude sur l'impact des signaux d'interférence à bande ultra étroite sur les communications de type LoRa. Nous fournissons les modèles d'interférence et montrons plusieurs résultats de simulation basés sur ceux-ci.
6. Un récepteur capable de décoder plusieurs signaux de type LoRa en collision destructive. Nous proposons une approche dans un contexte de liaison montante, où les noeuds transmettent vers un satellite; l'algorithme est basé sur l'annulation successive des interférences (SIC). Notre proposition permet d'augmenter de manière significative l'efficacité spectrale et la capacité des réseaux basés sur la technologie LoRa.
7. Une approche pour décoder les signaux de type LoRa en collision destructive dans un contexte de liaison descendante, où un satellite LEO envoie des messages aux noeuds. Nous avons proposé de contrôler la désynchronisation temporelle des signaux superposés afin de pouvoir les décoder sans avoir recours à l'algorithme SIC.
8. Un algorithme de détection de paquets utilisant des préambules de type LoRa. Cet algorithme performe d'une manière efficace avec un nombre aussi bien élevé que faible de noeuds connectés, comme c'est le cas pour les communications avec des satellite LEO, qui couvrent aussi bien les villes denses que les montagnes et les océans.

Le plan de la thèse est structuré comme suit :

Chapitre 1 : Dans ce chapitre, nous abordons les principaux aspects des communications LEO, tels que la trajectoire du satellite, le champ de vision, la fenêtre de visibilité, les effets Doppler et le bilan de liaison. De plus, étant donné que l'objectif de la thèse est d'établir des communications fiables par satellite LEO en utilisant l'une des technologies LPWAN les plus populaires, à savoir LoRa, nous donnons un aperçu de plusieurs d'entre elles. Ensuite, nous discutons de quelques défis de déploiement de ce type de technologies dans le contexte du satellite LEO et nous évaluons leur capacité à faire face à ces défis. Enfin, nous présentons quelques travaux industriels dans le domaine de l'IoT par satellite.

Chapitre 2 : Dans ce chapitre, nous détaillons le principe de modulation et de démodulation dans la couche PHY LoRa. Ensuite, nous formalisons l'impact d'une synchronisation imparfaite sur l'estimation des symboles des signaux de type LoRa. Sur la base de ces modèles, nous discutons plusieurs approches de synchronisation de la littérature utilisant un préambule

spécifique. Compte tenu de la sensibilité aux désynchronisations temporelles et fréquentielles, notamment la variation temporelle du Doppler, nous proposons une modification de la couche PHY LoRa que nous appelons CSS différentiel (DCSS). Nous prouvons, par plusieurs simulations, la capacité de cette technique à améliorer la robustesse contre les effets Doppler par rapport à la modulation CSS conventionnelle. Ainsi, sur la base de la technique DCSS et d'algorithmes de synchronisation originaux, nous proposons deux émetteurs-récepteurs adaptés aux communications par satellite LEO.

Chapitre 3 :

Dans ce chapitre, nous abordons la problématique de collision de paquets causée par le champ de vision d'un satellite LEO, qui permet de connecter un grand nombre d'objets. Comme nous l'avons expliqué précédemment, les communications LoRa étant déployées dans les bandes ISM libres, elles sont affectées par des signaux parasites, qui peuvent être générés par des noeuds utilisant des technologies identiques ou différentes. Actuellement, les technologies qui peuvent coexister avec LoRa, pour les communications par satellites LEO dans les bandes ISM, sont principalement basées sur des couches PHY UNB, comme Sigfox. Ainsi, nous commençons ce chapitre par étudier l'impact des signaux parasites UNB sur les communications de type LoRa afin de quantifier la robustesse de cette dernière forme d'onde dans un tel scénario. Ensuite, nous évaluons la robustesse d'un signal de type LoRa aux interférences générées par d'autres noeuds LoRa. Sur la base de ces résultats, nous présentons un nouveau récepteur capable de décoder plusieurs signaux superposés de type LoRa dans un scénario de liaison montante, en utilisant l'algorithme SIC. De plus, nous développons une approche similaire dans un cas de communication en liaison descendante en ajoutant une diversité de puissance qui peut remplacer l'algorithme SIC dans plusieurs configurations. Enfin, nous fournissons un algorithme original de détection de paquets adapté à la connexion d'un nombre très élevé d'objets aux satellites LEO ainsi qu'aux scénarios de faible connectivité, lors de la couverture de montagnes, d'océans, etc.

Contents

Introduction	16
1 Dedicated LPWA Technologies for LEO satellite communication	22
1.1 Low Earth Orbit communication	22
1.1.1 Principle	22
1.1.2 Theory of satellite Motion	24
1.1.2.1 Orbital trajectory	24
1.1.2.2 Orbital velocity	25
1.1.2.3 The satellite period around the Earth	25
1.1.2.4 Keplers Equation	26
1.1.3 Field of View	27
1.1.4 Satellite window of visibility	28
1.1.5 Doppler effects	28
1.1.6 Link Budget Calculation	30
1.2 Low Power Wide Area communication	32
1.2.1 Long range	33
1.2.2 Low energy consumption	34
1.2.3 Low cost	34
1.3 LPWAN technologies for LEO communication	35
1.3.1 Challenges of LPWAN communication with LEO satellite	35
1.3.2 Narrow Band IoT (NB-IoT)	36
1.3.2.1 Principle	36
1.3.2.2 Bit error rate under AWGN channel	37
1.3.2.3 Deployment with LEO satellite	38

1.3.3	Sigfox	40
1.3.3.1	Principle	40
1.3.3.2	Bit error rate under AWGN channel	41
1.3.3.3	Deployment with LEO satellite	42
1.3.4	LoRa - Chirp Spread Spectrum	43
1.3.4.1	The LoRa modulation	44
1.3.4.2	Bit error rate under AWGN channel	44
1.3.4.3	Deployment with LEO satellite	45
1.3.5	Long Range-Frequency Hopping Spread Spectrum	48
1.3.5.1	Principle	48
1.3.5.2	Bit error rate under AWGN channel	49
1.3.5.3	Deployment with LEO satellite	50
1.4	Industrial IoT deployments in LEO satellite communication	51
1.5	Conclusion	54
2	LoRa-like synchronization approaches for LEO satellite communications	57
2.1	LoRa PHY layer	58
2.1.1	Modulation	58
2.1.2	Demodulation principle	59
2.1.3	Channel coding and interleaving in LoRa	61
2.2	Insights on strategies used to synchronize LoRa signals	62
2.2.1	Model of received signals	62
2.2.2	Impact of the CFO on symbol estimation	64
2.2.3	Impact of the DR on the symbol estimation	65
2.2.4	Impact of the STO on the symbol estimation	66
2.3	State of the art on synchronization algorithms with LoRa signals	67
2.3.1	Structure of the synchronization signal	67
2.3.2	Time and frequency synchronization algorithms	68
2.3.2.1	Fractional CFO estimation	69
2.3.2.2	Fractional STO estimation	70
2.3.2.3	Integer CFO and integer STO estimation process	71
2.3.3	Limits of the synchronization algorithms	72
2.4	Differential Chirp Spread Spectrum	74

2.4.1	Modulation	74
2.4.2	Demodulation	74
2.4.3	Fine estimation of the symbols	75
2.4.4	DCSS Performance evaluation and comparison with CSS	76
2.4.4.1	Perfect synchronization case	77
2.4.4.2	Robustness against the CFO and STO	78
2.4.4.3	Robustness against Doppler time-variation	78
2.5	Proposed DCSS Transceiver using chirped preamble	80
2.5.1	Proposed synchronization signal	80
2.5.2	Proposed synchronization algorithm	81
2.5.2.1	Preamble detection	83
2.5.2.2	Coarse time synchronization	83
2.5.2.3	Doppler rate estimation	85
2.5.2.4	Fractional CFO estimation	86
2.5.2.5	Fractional STO estimation	86
2.5.2.6	DR, fractional CFO and fractional STO compensation	87
2.5.3	Results and Discussions	88
2.5.3.1	Synchronization algorithm numerical results	88
2.5.3.2	Decoding performance of the proposed receiver	89
2.6	Dual Waveform DCSS Transceiver	93
2.6.1	Proposed Transmitted Signal	94
2.6.2	Proposed Receiver	95
2.6.3	Results and Discussions	96
2.7	Conclusion	99
3	Interference management of LoRa-like communications with LEO satellites	102
3.1	Impact of UNB interfering signals on LoRa	103
3.1.1	Interference Model	103
3.1.2	Results and Discussions	106
3.2	Inter- SF and same- SF interference in LoRa	108
3.2.1	State of the art	108
3.2.2	Impact of inter- SF interference	110
3.2.3	Impact of same- SF interference	111

3.2.3.1	Problem modeling	111
3.2.3.2	Strategies to deal of same- SF interference	114
3.3	Proposed uplink approach to process the multiple Reception of non-orthogonal LoRa-like signals	115
3.3.1	System model	116
3.3.1.1	Model of transmitted signals	116
3.3.1.2	Model of received signals	117
3.3.2	Proposed algorithms to process the reception of multiple non-orthogonal LoRa-like signals	119
3.3.2.1	Detection of the strongest signal	119
3.3.2.2	Time and frequency synchronization of the strongest signal	122
3.3.2.3	Decoding the strongest signal	122
3.3.2.4	Strongest signal cancellation	123
3.3.2.5	Processing of superimposed peaks	123
3.3.3	Results and Discussions	126
3.3.3.1	Simulation results on synthesized signals	126
3.3.3.2	Experimental validation using Software Defined Radio	133
3.4	Proposed downlink approach to help nodes processing the multiple Reception of non-orthogonal LoRa-like signals	135
3.4.1	System model	136
3.4.1.1	Model of transmitted signals	136
3.4.1.2	Model of received signals	137
3.4.2	Proposed receiver	137
3.4.2.1	Strategy based on the power diversity	139
3.4.2.2	Strategy based on the power diversity and a SIC approach	140
3.4.3	Results and Discussions	141
3.4.3.1	Impact of the Power Ratio and the SIC	141
3.4.3.2	Impact of the SF and the coding rate	142
3.5	Proposed packet detection algorithm based on chirped signals	144
3.5.1	Eutelsat specifications	144
3.5.2	Structure of the preamble	145
3.5.3	Proposed algorithm	146
3.5.3.1	Preambles detection without interference	146

3.5.3.2	Management of the multiple packets reception	149
3.5.4	Results and Discussions	152
3.6	Conclusion	155
	Conclusion and perspectives	158
	List of Publications	161
	List of Figures	166
	List of Tables	167
	Bibliography	167

Introduction

Businesses today have operations around the world, and many of their assets are in remote areas with extremely limited connectivity. Thereby, they need to exchange data in order to connect to their resources and receive feedback as soon as possible in order to keep their operations running smoothly and efficiently [1]. To conquer these challenges, most of companies deploy terrestrial wireless networks infrastructure, which allow to connect devices using several communication technologies. However, the use of these networks is not an optimal solution to assure world-wide connectivity especially in remote areas, where the cellular infrastructure is very limited. Indeed, terrestrial networks only cover 15% of the Earth's surface [1]. Base stations and gateways simply cannot be deployed across oceans, deserts or mountain tops, and they are not cost-effective enough to be installed in remote and sparsely populated areas. For instance, it is impossible to keep an eye on a container shipped from China to the United States of America (USA) via the conventional cellular networks.

Moreover, in some cases, although the terrestrial coverage exists, multiple networks could be deployed to travel between several places, which entails the roaming fees.

Giving the latter need to connect objects wherever in the globe, we currently witness the emergence of the Internet of Things (IoT) connectivity via the satellites. This solution would allow to theoretically connect the total surface of the Earth. In the recent years, several projects in the field of satellite IoT have been fulfilled. For instance, Swarm [2] uses the popular IoT technology LoRa [3] in their low-Earth orbit (LEO) satellites constellation [4], and Eutelsat have launched several nano satellites to serve Sigfoxs [5] generic IoT applications [6]. Many industrial projects employ low-power wide-area networks (LPWANs) in order to establish IoT communications with LEO satellites. The choice of the latter IoT networks is justified by their capacity to establish extremely long range communications, while maintaining low energy consumption of the devices, which seems to be very attractive solution to reach a global connectivity via LEO satellites. Furthermore, in terms of transmitted power, propagation delay and coverage, LEO satellites are more suitable for LPWAN communications than other types of satellites. Hence, we study in this thesis several aspects of LPWAN communications with LEO satellite and we will focus on the enhancement of LoRa PHY layer in order to cope with the

requirements of the latter communications.

In the remainder of this introduction we will discuss some generalities and requirements of the LPWAN communications using LEO satellites, and present the contributions and an outline of the thesis.

Low Power Wide Area Networks communications using LEO satellites

IoT is the interconnection between the Internet and physical objects, places and environments. The term designates a growing number of objects connected to the internet, thus allowing communication between our so-called physical assets and their digital existence. In a few years, almost every device that we use in our everyday life would be connected to the internet via IoT technologies. Indeed, the number of connected objects has vastly increased in the last years, and is expected to grow even more rapidly in the years to come [7, 8]. As we can imagine, there are countless applications for IoT networks. With uses ranging from smart grid applications to agricultural monitoring, health monitoring, smart metering, localization and tracking, logistics, and smart city applications [1, 9].

A lot of IoT applications fall into the category of low data-rate transmission of small amount of information, such as temperature, humidity, and pressure values, at regular intervals. Given this massive connectivity that does not employ high data-rate application, we witnessed in the last decade the emergence of LPWANs. As its name indicates, LPWANs allow devices to autonomously transmit at long ranges and for many years. To achieve the last goal, very low power transmission protocols are employed. In fact, the majority of LPWANs deploy transmission protocols based on uncoordinated channel access schemes, such as the ALOHA protocol. They also tend to be long-ranging, to cut down on the amount of other infrastructure required to deploy a large-scale IoT project [10]. By affording massive long range connectivity that guarantees low energy consumption of the devices and low deployment cost of the network, LPWANs could be good candidates for LEO satellite communications.

Nevertheless, in order to establish reliable communications with a LEO satellites, the deployed wireless technology should fulfill several requirements. In fact, one of the main challenges of such communication is the presence of significant Doppler effects due to the high speed of these satellites. These Doppler effects induce an offset in the carrier frequency between the transmitter and the receiver. In the case of LPWANs, which are considered in this thesis, the most inconvenient Doppler effect is when the latter is time-varying along the packet duration. Giving the low data-rate used in LPWANs, yielding long packets, and the high speed of the Doppler variation (i.e. several hundreds of Hz/s), it is very likely that this variation would

have a significant impact on the demodulation of these packets.

The second main challenge of such communications is the massive number of devices that could be connected with a LEO satellite, caused by its Field of View (FoV). This massive connectivity yield to high probability of packet collision, especially giving the uncoordinated access schemes to frequency channels as deployed by the majority of LPWANs in order to reduce the energy consumption of the nodes. Moreover, given that LoRa, as the majority of LPWANs, employs the unlicensed Industrial, Scientific, and Medical (ISM) frequency bands, it would deal with packet collision from nodes using other technologies, such as Sigfox which is based on the ultra narrow band (UNB) PHY layer. Also, signals from several LoRa nodes can be simultaneously received over the same frequency channel, which could create destructive collisions. Thereby, packet collision, generated by node using the same technology or different technologies, is a serious problem when considering satellite IoT via LPWAN technologies.

In this thesis, we consider one of the most popular unlicensed LPWAN technologies, namely LoRa. LoRa uses chirp spread spectrum (CSS) modulation to achieve long-range connectivity and resilience to noise and narrow band interference. The contributions of this thesis consist mainly in dealing with the above-mentioned two problems in the context of LoRa-like communications with LEO satellites.

Thesis contributions and outline

The thesis contributions are the following:

1. A study of the impact of time and frequency desynchronizations on the LoRa symbol estimation when communicating with a LEO satellite.
2. A modification of the LoRa PHY layer to be more robust to time and frequency offsets, especially the one caused by the Doppler time variation. This proposed PHY layer is based on the well-known differential process.
3. A first transceiver based on the PHY layer 2/ combined with an original synchronization algorithm allowing to decode LoRa-like signals in the presence of significant Doppler effects. Hence the proposed transceiver would be a good candidate for LEO satellite communications.
4. A second transceiver based on the PHY layer 2/ combined with a classical time synchronization and the use of a non-LoRa waveform in the preamble. The proposed waveform is insensitive to phase time-variation, and thus, the time synchronization can be performed regardless to the frequency offsets. Thereby, this approach allows to take advantage of

robustness of the proposed waveform to frequency offsets, and thus, can be deployed to communicate with LEO satellites.

5. A study on the impact of UNB interfering signals on LoRa-like communications. We provided the models of interference and showed several simulation results based on them.
6. A receiver able to decode several LoRa-like signals in destructive collision. We proposed an approach in an uplink context, where nodes transmit to a the satellite, which is based on the successive interference cancellation (SIC) algorithm. Currently, if such collision occur all the superposed packets will be re-transmitted, or using the capture effect only the strongest signal will be accurately decoded if it has a received power 6 dB greater than the second powerful signal [11, 12, 13]. Hence, our approach would significantly increase the spectral efficiency and the capacity of LoRa-based networks.
7. An approach to decode LoRa-like signals in destructive collision in a downlink context, where a LEO satellite sends messages to the nodes. We proposed to control the time desynchronization of the superposed signals in order to be able to decode them without needing the SIC algorithm.
8. A packet detection algorithm using LoRa-like preambles. This algorithm is suited for low and massive connectivity as it is the case for LEO satellite, which covers dense cities as well as mountains and oceans.

The dissertation outline is structured as follows:

Chapter 1: In this chapter, we discuss the principle aspects of LEO communications, such as the satellite trajectory, the field of view, the window of visibility, Doppler effects and the link budget. Moreover, given that the objective of the thesis is to establish reliable LEO satellite communication using one of the most popular LPWAN technologies, namely LoRa, we give an overview on several of them. Then, we discuss several challenges of deploying this type of IoT technologies in the context of LEO satellite and we evaluate their capacity to cope with these challenges. Finally, we provide some industrial works in the field of satellite IoT.

Chapter 2: In this chapter, we detail the modulation and demodulation principle in LoRa PHY layer. Then, we formalize the impact of imperfect synchronization on the symbol estimation of LoRa-like signals. Based on these models, we discuss several synchronization approaches from the literature using a specific preamble. Given the sensitivity to time and frequency desynchronizations, especially the Doppler time-variation, we proposed a modification of the LoRa PHY which we refer to as differential CSS (DCSS). We prove, through several simulations, the capacity of this proposed technique to enhance the robustness against Doppler effects compared to the conventional CSS modulation. Thereby, based on the DCSS technique

and original synchronization algorithms, we proposed two transceivers suited for LEO satellite communications.

Chapter 3: In this chapter, we deal with the issue of packet collision caused by the FoV of a LEO satellite, which allow to connect huge number of end-devices. As explained previously, since LoRa communications are deployed in the free ISM bands, they are affected by interfering signals, that can be from nodes using the same or different technologies. Currently the technologies that may coexist with LoRa, for LEO satellite communications in ISM bands, are mostly based on the UNB PHY layer, such as Sigfox. Thus, we start this chapter by studying the impact of UNB interfering signals on LoRa-like communications to quantify the robustness of the latter waveform in such scenario. Then, we evaluate the robustness of a LoRa-like signal of interest to interference generated by other LoRa-like nodes. Based on these results, we present a novel receiver able to decode several superposed LoRa-like signals in an uplink scenario, using the SIC algorithm. Moreover, we develop a similar approach in a downlink communication case by adding a power diversity that can replace the SIC algorithm in several configurations. Finally, we provide, an original packet detection algorithm suited to the massive connectivity with LEO satellite as well as low connectivity scenarios, when covering mountains, oceans, etc.

CHAPTER 1

Dedicated LPWA Technologies for LEO satellite communication

In this chapter, we aim to discuss the principle aspects of low-Earth orbit (LEO) communication (i.e. satellite trajectory, Field of view, window of visibility, Doppler effects, link budget). Moreover, given that the objective of the thesis is to establish reliable LEO satellite communication using the popular LPWAN technology LoRa, we provide an overview on several LPWAN technologies. Then, we discuss the challenges of deploying this type of IoT communication in the context of LEO satellite. Finally, we provide some industrial works in the field of satellite IoT.

1.1 Low Earth Orbit communication

This section is dedicated to provide some basic principles on LEO satellite motion and its impact on the link satellite-ground terminal (GT). In this study we consider an uplink scenario, where the GTs transmit their messages to a LEO satellite which is considered as a gateway that gathers and process their information.

1.1.1 Principle

A Low Earth orbit is generally defined as one with an altitude between 500 and 2000 km. Communication via LEO satellite begins only when the GT is under its Field of View (FoV). It is notable that the largest coverage area is achieved under elevation of 0° . However, the range under the lowest elevation angle represents the worst link budget case, since that range represents the maximal possible distance between the GT and the satellite which means that

the quality of transmitted signals are subject to degradation through the atmosphere due to natural barriers. Therefore, the minimal elevation angle is considered in the range of $(2-20)^\circ$. Given these characteristics of LEO satellite FoV, global coverage requires a large number of spacecrafts [14]. These concepts will require major changes in satellite operations, including manufacturing and the supply chain, since they ask more of a satellite and shorten its average life span (estimated to be about five years with Starlink, the SpaceX constellation, for example) [15].

Since LEO satellites move too fast over the Earth, the footprint moves also, along with it, leaving the GT out of the footprint and consequently losing the communication. Thus, to precisely determine the duration of the visibility and the communication duration for each LEO satellite pass over the GT and prepare the GTs antenna in advance to wait for the upcoming pass of the satellite for an eventual transmission. Indeed, satellites trajectory known as orbits can be easily tracked using Kepler's laws of planetary motion. Whereas, to offload the complexity from the GT, the latter can transmit a packet whenever is ready and hoping the visibility of an intended LEO satellite from a defined satellite constellation.

Another point of emphasis is that a high satellite velocity implies Doppler effects causing a variation of certain signal properties between its emission and its reception. Subsequent, the received signal may experience significant time-varying carrier frequency offset (CFO) caused by Doppler distortion due to the relative motion between transmitter and receiver. Hence, in the case of LEO satellite communication, Doppler shift and Doppler rate (DR) estimation can be performed at the receiver for correct demodulation of the received signal [16]. It worth noting here that the Doppler shift can be also compensated at the transmission stage knowing the ephemeris of the satellite.

To understand the study on the LEO communication provided in this section, lets go through the classic orbital elements (COEs) that are used to visualize properly how the orbit looks in space, thus:

- To specify the Orbital size, the semi-major axis a is used.
- To describe the Orbital shape, the eccentricity e is defined.
- Orientation of the orbital plane in space uses inclination i (the tilt of the orbital plane with respect to the equatorial plane).
- Orientation of the orbit within the plane is defined by argument of perigee ω_0 (the angle between the ascending node and perigee measured in the direction of the spacecrafts motion) and finally spacecrafts location in the orbit is represented by true anomaly θ (the angle between perigee and the spacecrafts position vector measured in the direction of the spacecrafts motion).

Using the latter COEs, we provide in the next paragraph some basic information about the satellite orbital trajectory.

1.1.2 Theory of satellite Motion

In this paragraph we detail some basics on the satellite motion. Indeed, several expressions of the orbital trajectory, the orbital velocity, the orbital period around the earth of the satellite, are provided.

1.1.2.1 Orbital trajectory

When rockets launch satellites, they put them into orbit in space. Under the hypothesis that the effects of all the gravitational influence of bodies other than the Earth are neglected, as depicted in Fig. 1.1, the satellite is revolving in an elliptical orbit with the Earth at one focus (according to Keplers 1st law [17]). As shown in this figure, the primary focus F_1 is the location of the attracting body, while the secondary (vacant) focus F_2 has no physical significance. Therefore, the relative position vector remains bounded, having its smallest magnitude at perihelion r_{min} and moving away from the Earth to aphelion r_{max} in a periodic movement. If the two turning points coincide; the ellipse becomes a circle of radius $r_{min} = r_{max}$.

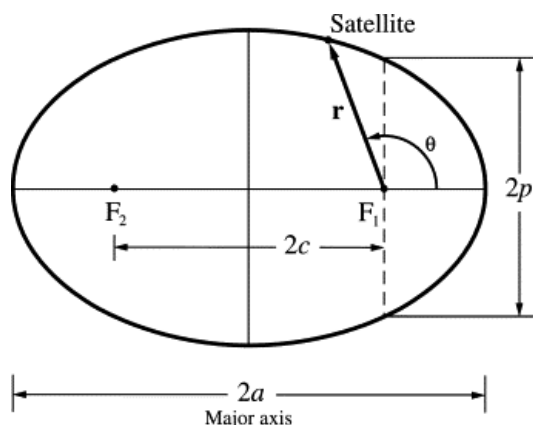


Figure 1.1: Description of the Elliptical orbit from [18]

In polar coordinate system, the equation of the satellite's elliptical orbit is the following:

$$r = \frac{h^2}{\mu} \cdot \frac{1}{1 + e \cos \theta} \quad (1.1)$$

Where

- h is constant. It represents the relative angular momentum of the satellite per unit mass, that is, the specific relative angular momentum. The unit of h is m^2/s .

- μ is the gravitational parameter (constant, m^3/s^2). In fact: $\mu = GM_E$ where G is the gravitational constant ($m^3Kg^{-1}s^{-2}$) and M_E is the mass of the Earth.

It worth noting that the constant p , depicted in Fig. 1.1, is called the parameter or semilatus rectum [18] and is equal to:

$$p = \frac{h^2}{\mu}$$

Whereas, in Cartesian coordinate system, the coordinate of the orbit is given by the following equation:

$$\frac{x^2}{a^2} + \frac{y^2}{b^2} = 1 \quad (1.2)$$

Where

- a is the semi-major axis.
- b is the semi-minor axis.

In addition, we have to note that:

$$r_{min} = \frac{\frac{h^2}{\mu}}{1 + e}$$

and

$$r_{max} = \frac{\frac{h^2}{\mu}}{1 - e}$$

1.1.2.2 Orbital velocity

Concerning the orbital velocity, as the gravity which is a central and conservative force is the only force doing work, the total mechanical energy of the system is conserved. Hence, by using the conservation of energy at the perihelion and the aphelion, it can be shown that the satellite's speed at any position is given by:

$$v = \sqrt{\mu \left(\frac{2}{r} - \frac{1}{a} \right)}$$

For instance, the orbital velocity of a satellite, with an altitude of 550 km, is in the order of 7.8 km/s.

1.1.2.3 The satellite period around the Earth

The period of elliptical orbits is given by the following expression:

$$T_E = 2\pi \sqrt{\frac{a^3}{\mu}}$$

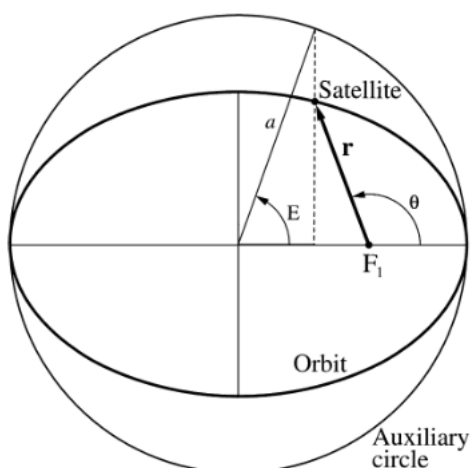


Figure 1.2: Ellipse and the circumscribed auxiliary circle from [18].

And by substituting μ by GM_E , we easily prove that the ratio $\frac{a^3}{T_E^2}$ is the same for all satellites orbiting around the Earth. This is Kepler's third law.

Typically, orbital periods, for LEO satellites, are of the order of 90 minutes [17].

1.1.2.4 Keplers Equation

To define the position of a body that is moving along an elliptic Kepler orbit, three angular parameters called anomalies are defined: true anomaly θ , mean anomaly M_e and the eccentric anomaly E . The mean anomaly M_e is the azimuth position (in radians) of a fictitious body moving around the ellipse at the constant angular speed $\eta = \frac{2\pi}{T_E}$. For a circular orbit, the mean anomaly and the true anomaly θ are identical [19]. The mean anomaly M_e , which is an equivalent angle that changes linearly in time, can be written as:

$$M_e = \eta t \quad (1.3)$$

Hence, to determine the position of an object moving in an elliptic orbit, knowing the mean anomaly M_e , we define the eccentric anomaly E as the angle depicted in Fig. 1.2 and can be expressed as:

$$E = \arccos \frac{e + \cos \theta}{1 + e \cos \theta}$$

Thus, the angular position of the satellite can be found at any later time by solving Keplers Equation:

$$E - e \sin E = M_e$$

It should be noted that this equation does not have a closed-form solution for E given M_e . An accurate solution requires an iterative, trial and error procedure, and Newtons method is one

of the more common and efficient methods to apply to the solution of Keplers equation. We have just to form the function:

$$f(E) = E - e \sin E - M$$

and seek the value of eccentric anomaly that makes

$$f(E) = 0$$

Finally, as will be detailed in the next paragraph, the eccentric anomaly is used to compute the distance between the satellite and the GT. For more details and proofs, reader can refer to [19, 18].

After giving a brief overview on the satellite elliptic orbit, we propose in next paragraph to compute the distance between a satellite and any point in Earth, then we formalize its FoV.

1.1.3 Field of View

The position of the satellite within its orbit considered from the GT point of view is defined by azimuth (A_z) and elevation (ϵ_0) angles. The azimuth is the angle of the direction of the satellite, measured in the horizon plane from geographical north in clockwise direction. The range of azimuth is 0° to 360° . The elevation is the angle between a satellite and the GTs horizon plane. The range of elevation is 0° to 90° .

The distance d from the GT to the satellite is called the slant range and it is expressed through elevation angle ϵ_0 . It changes over time since the satellite flies too fast above the GT. Hence, based on the previous definition and giving that R_E is the Earth radius, we have:

$$d = \sqrt{a^2(\cos E - e)^2 + a^2(1 - e^2) \sin^2 E - R_E^2 \cos^2 \epsilon_0 - R_E \sin \epsilon_0} \quad (1.4)$$

Therefore, the coverage angle Ψ_{FoV} between the sub-satellite point, the center of the Earth and the edge of coverage which determines the radius of the FoV is given by the following equation:

$$\Psi_{FoV} = \frac{\pi}{2} - \epsilon_{min} - \arcsin\left(\frac{R_E(1 + e \cos(\omega - \omega_0))}{a(1 - e^2)} \cos \epsilon_{min}\right) \quad (1.5)$$

Where ω is the angle from the ascending node to the satellite, ω_0 is the argument of perigee of the elliptical orbit and ϵ_{min} is the minimum elevation angle. Thus, the circle of coverage of

the satellite around the GT is defined by the latitude u and longitude q as follows:

$$\sin(u) \sin(u_{gt}) + \cos(u) \cos(u_{gt}) \cos(q) = \cos(\Psi_{FoV}) \quad [20]. \quad (1.6)$$

with u_{gt} being latitude of this GT. For more details and proofs, reader can refer to [20, 21]

1.1.4 Satellite window of visibility

The visibility duration is the time between the GT entering and leaving the coverage area of the satellite. One simplification is performed to obtain the analytical expression of the visibility duration of the satellite at a terminal is that the angular velocity of the satellite is assumed to be constant.

Thus, an analytical method has been developed to screen out non-visibility periods between the satellite and a specific GT and we obtain the maximum duration of the visibility window as follows:

$$T_{vis} = \frac{2}{\omega_F} \arccos\left(\frac{\cos(\Psi_{min})}{\cos(\Psi_{max})}\right)$$

Where Ψ_{min} is the central angle at epoch of minimum elevation angle for visibility, Ψ_{max} is the central angle at epoch of maximum elevation angle for visibility and ω_F is given by the following equation:

$$\omega_F = \omega_s - \omega_E \cos i$$

Where:

- ω_s is the angular velocity of the satellite.
- ω_E is the angular velocity of the Earth rotation.
- The inclination i is the tilt of the orbital plane with respect to the equatorial plane.

As already mentioned, orbital periods, for LEO satellites, are of the order of 90 minutes, which means that satellites will only be visible from 5 to 20 minutes per orbit (depending on altitude) [17].

1.1.5 Doppler effects

The Doppler shift is observed when a source of waves is moving in relation to an observer or vice versa. This movement produces a change in frequency in relation to observer. Due to the high speed movement of LEO satellites, Doppler frequency shift is one of the most severe problems in such communications. Indeed, Doppler shift is defined as the observed changes in

frequency of transmitted signals when relative motion exists between the satellite and the GT. Therefore, an estimation of latter shift would be one of the most important factors to enhance performance of LEO satellite communication system.

The Doppler frequency shift is represented only during the visibility window of the satellite at the GT or the terminal. Then, to predict the shape of the Doppler effect variation over the visibility duration, the relative velocity between the satellite and the GT should be determined. Hence, the following equation captures Doppler frequency shift f_d :

$$f_d = \frac{f_c}{c} \cdot \sqrt{\frac{GR_E}{1 + H/R_E}} \cdot \frac{\sin(\psi)}{\sqrt{(1 + H/R_E)^2 - 2(1 + H/R_E) \cos(\psi) + 1}} \quad (1.7)$$

Where

$$\psi = \frac{\sqrt{G/R_E}}{(1 + H/R_E)^{3/2}} \cdot t \quad (1.8)$$

Here c is the speed of the light in vacuum and H is the satellite orbit height. For more details and proofs, reader can refer to [22] and can find other expressions to define the Doppler frequency shift as in [23].

Based on (1.7), we can easily deduce that the Doppler effect is mainly related to the signal carrier frequency and the satellite orbit height [22]. Moreover, given the expression of (1.7) the Doppler shift and the Doppler time variation (i.e. DR) are represented in Fig. 1.3 as function of the time in the visibility window. These results are obtained from an Eutelsat [1] nano-satellite with a typical altitude of $H = 550$ km and given the carrier frequency of the LoRa signals 868 MHz. It can be seen that the maximum Doppler shift of LoRa signal is about 19 kHz, and the maximum DR is about 280 Hz/s. Hence, for a long packets duration, this variation will considerably impact the decoding performance of the technology used to communicate with LEO satellite. Moreover, it should be noted here that the visibility window of the latter satellite is 320s, which is very low to ensure a continuous connectivity of the GT. Hence, as we can see in the next paragraph, several companies have launched constellation of multiple LEO satellites to guarantee the required connectivity.

Finally, dealing with significant Doppler effects should be attentively considered when choosing the wireless technology to assure the communication with LEO satellite. An other requirement that must be fulfilled by the deployed technology is a link budget allowing to establish reliable LEO satellite communication. Subsequent, in the next paragraph, we provide a study on the link budget of LEO satellite communication with a GT.

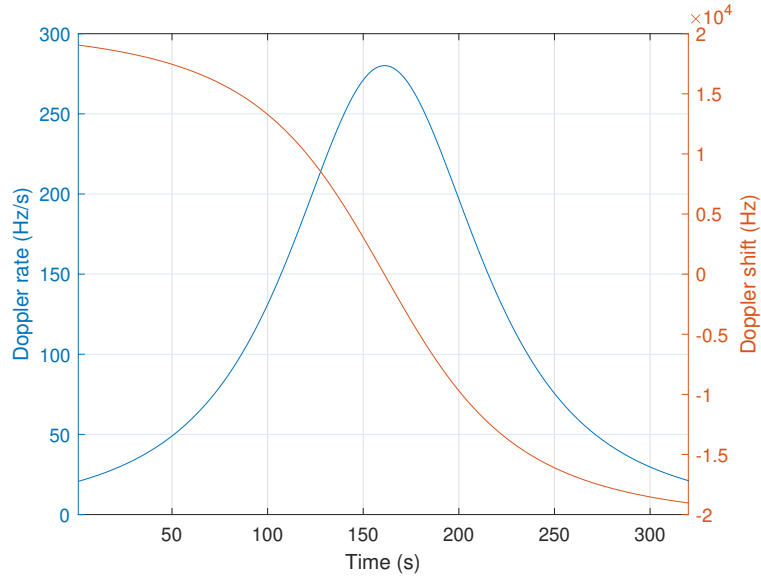


Figure 1.3: Doppler shift and Doppler rate evolution from an Eutelsat nano-satellite with a typical altitude of 550 km and given the carrier frequency of 868 MHz

1.1.6 Link Budget Calculation

In all communication systems, one of the most important steps is the computation of the link budget. A link budget of a radio frequency (RF) communication is a set of parameters that describe a link in terms of power levels required to establish reliable communication between the transmitter and the receiver [24]. A measure of the performance of a satellite link is the ratio of the measured signal strength to noise power at the receiver input, and link budget calculations are often concerned with determining this ratio.

We recall here that uplink communication scenario is considered. Thus, to measure the link budget of such communication, we provide hereafter some details of the components or factors that contributes to gain along this communication link. Detailed reviews of these factors are provided in the following items:

- **Equivalent Isotropic Radiated Power**

The Equivalent Isotropic Radiated Power ($EIRP$) of the transmitter is a measure of the transmitted power and is calculated as follows:

$$EIRP = P_{TX} \Big|_{\text{dBW}} - L \Big|_{\text{dB}} + G_{TX} \Big|_{\text{dBi}}$$

Where P_{TX} is the transmitted power, L is the transmission line loss and G_{TX} is the gain of the transmitter antenna.

- **Free Space Loss**

Free space path loss is the loss in strength of an electromagnetic signal as it travels through free space in a line-of-sight path from a transmitting antenna to a receiving antenna. Its expression is given by the following equation:

$$L_{FS} = 20 \log_{10} \left(\frac{4\pi df_c}{c} \right)$$

Where f_c is the uplink carrier frequency.

- **Atmospheric Loss**

As the signal travels through the atmosphere, the different molecules that compose the air absorb its energy at different rates depending on carrier frequency. Therefore, atmosphere loss can be categorized as attenuation of signal energy. One of the most important atmospheric loss is the rain penalty, which is frequency-dependant, and generally higher for higher frequencies. Commercially used bands, notably Ku, K and Ka bands are much more effected than bands below 1 GHz [24, 25].

- **Polarization coupling loss**

The polarization coupling loss is due to any polarization mismatch between the antennas. For instance, when transmitting and receiving antennas are of different polarizations, for example, with horizontal and vertical polarization, respectively, then the angle between the radiated fields is 90° and no power is transferred between the antennas.

Hence, the calculation of the signal to noise ratio of an uplink communication case is given by the following equation:

$$\text{SNR} = \text{EIRP} - L_{FS} - L_{At} - L_P + G_{RX} - 10\log_{10}(k_B T_N B) \quad (1.9)$$

where $k_B = 1.38 \times 10^{-23}$ J/K is the Boltzmann constant, L_P is the Polarization loss, L_{At} is the atmospheric loss, B is the received signal bandwidth, T_N is the equivalent noise temperature and G_{RX} is the receiver antenna gain.

To quantify the capacity of a receiver to decode signals with low power, we usually compute the receiver sensitivity, which is the measure of the minimum signal strength that the receiver can detect and process, as follows:

$$S \Big|_{\text{dBm}} = \text{SNR}_{th} \Big|_{\text{dB}} - 174 + 10\log_{10}(B) + NF \Big|_{\text{dB}} \quad (1.10)$$

- S : Receiver sensitivity
- NF : Noise factor

- SNR_{th} : Signal to noise ratio sensitivity threshold, which is the minimum SNR that provides a defined Quality of Service (QoS). For all the upcoming measurements of the receiver sensitivities in this chapter, SNR_{th} is defined as the minimum SNR that give a bit error rate lower than 10^{-5} . Hence, a signal received at the satellite can be accurately decoded only if $\text{SNR} \geq \text{SNR}_{th}$.

To note that the latter expression of the receiver sensitivity is done with $T_N = 293$ K (20°). We have $10\log_{10}(1.38 \times 10^{-23} \times 293 \times 1000) = -174$ dBm/Hz. Given the expression of (1.10), the receiver sensitivity S can be reduced by lowering either SNR_{th} or B . A detailed study on link budget calculations is provided in [24].

In the following section, we introduce the LPWAN principle and main requirements. Then, we will discuss the challenges of deploying the latter networks in LEO satellite communication scenario. Finally, we provide an overview on several LPWAN technologies.

1.2 Low Power Wide Area communication

Low Power Wide Area networks (LPWANs), which emerged in the 2010 decade, represent a communication paradigm, which will complement traditional cellular and short range wireless technologies in addressing diverse requirements of IoT applications [26]. LPWANs allow to connect, with a long range, a large number of objects, which occasionally transmit small amounts of information, while maintaining low power consumption, most often powered by a battery that should last several years. In other terms, LPWAN technologies offer unique sets of features including wide-area connectivity for low power, low cost and low data rate devices, not provided by legacy wireless technologies.

Both industry and academic are already making significant strides toward a mass IoT solution deployment. Indeed, multiple technologies with different physical and MAC layer standards have been developed to address constrained connected object challenges [27]. LPWAN technologies are accessible to support both licensed and unlicensed spectrum.

On the one hand, IoT technologies in licensed spectrum, are an evolution of existing 3GPP cellular standards. For this reason the physical (PHY) and medium-access control (MAC) layers of these technologies are relatively complex. Cellular IoT standards cover many use cases and use licensed frequency bands to provide robustness and security. Since cellular standards have been designed to cover high data rate services for smaller number of devices, they face the challenge of a fundamental paradigm shift to low data rate services for a much larger number of devices [28].

In the other hand, free bands are mostly the Industrial, Scientific, and Medical (ISM) frequency bands. The ISM bands are designated RF bands as defined by the ITU radio regulations.

These frequency bands were set aside for RF use for purposes other than telecommunications. Hence, using the ISM bands for telecommunications is possible, but telecommunications devices using these frequencies must be able to withstand the interference from other RF and microwave technologies. Subsequently, the primary advantage of such communication in free bands is license cost effectiveness. Nevertheless, the main downside of uncontrolled channel access is the high interference levels. To reduce the impact of the latter severe issue, regulation impose some constraints such as the maximum transmitted power and the communication time duration. However, boundary of maximum transmitted power will impact the range of the LPWAN technology operating in ISM bands and the constraint of the duty cycle would reduce the number of possible connections per day.

In order to be LPWAN, the following requirements should be fulfilled:

- Long range,
- Low power,
- Low cost.

These features will be detailed in the next paragraphs.

1.2.1 Long range

The first requirement of LPWAN technologies is the long range communications. Hence, nodes using the latter technologies usually transmit small messages with low data which makes the transmitted signals occupy a narrow bandwidth. This propriety, allow to reduce the receiver sensitivity and thus increase the link budget of the communication. Moreover, deploying narrow bandwidth and low data rate improve reliability of the communication and alleviate the detrimental effects of interference arising from jamming, multi-path propagation. Furthermore, to guarantee the long range aspect, LPWAN technologies usually deploy sub-GHz frequency bands, which have favorable propagation properties.

Given the expression of the receiver sensitivity, as depicted in (1.10), the long range propriety is assured by reducing either the bandwidth B or the SNR sensitivity threshold. Thus, several LPWAN technologies based on ultra narrow band (UNB) or narrow band PHY layers are emerged in one hand. In the other, very low SNR_{th} could be reached for LPWANs deploying channel coding and/or spread spectrum techniques like the chirp spread spectrum modulation (CSS) [29].

1.2.2 Low energy consumption

The second requirement of a LPWAN communication is the low power aspect. Hence, several techniques have been implemented to reduce the energy consumption of the end-devices. For instance, regulations could impose some constraints to that end and to reduce the impact of interference especially in free access bands. Indeed, regulations vary from region to region; for example, regulations in the USA rely on electrical field strength and harmonic strength, while European Union (EU), regulations are based on duty cycle (DC) and maximum transmission power [30]. The DC is defined as the maximum amount of time devices are allowed to transmit or the ratio of the cumulated sum of transmission time per observation period [30]. Moreover, the latter constraint are frequency band-specific; e.g. the ETSI standard N° EN300220 defines the DC and the maximum transmitted power in 868MHz 868.6MHz bands as 1% and 25mW respectively [31]. Subsequently, after transmitting a packet, the node must wait for a minimum duration before starting an other transmission. This duration is referred to as time off air T_{off} and can be expressed as follows:

$$T_{off} = \frac{T_{on}}{DC} - T_{on}$$

with T_{on} is the time on air giving the packet duration.

As an example to illustrate the impact of the duty cycle. If we consider a packet with $T_{on} = 2$ s and a DC = 1%. Hence, the T_{off} is equals to 198s, which give a 430 connections/day.

An other technique to reduce the energy consumption of the end-devices is the light-weighting of the MAC layer by adopting the random access to the radio channel. For instance, the use of ALOHA-based access protocols. This processing would reduce considerably the energy consumption of the nodes since there is no need for network synchronization. The nodes transmit their messages whenever they are ready, which allow to offload the complexity from end-devices. In addition, if downlink communication are necessary, mechanism must be applied (wake up at a scheduled time agreed with the gateway).

Furthermore, the waveform used in the PHY layer of a LPWAN technology should remain at constant envelope, which allows an optimal use of the power amplification function [32]. Finally, high complexity algorithms are implemented at the gateway to offload the transmitter complexity.

1.2.3 Low cost

LPWAN applications are particularly sensitive to device and deployment costs. Indeed, the large number of involved devices imposes major constraints on cost, operating expenses and a requirement for low power consumption. The ability to upgrade software without changing hardware is a key attribute that must be addressed. Hence, it is imperative for LPWANs to

support scalability, ease of installation and low cost maintenance. In this context, the design of small-sized low complexity devices is an essential requirement. Reducing the complexity of the hardware structure allows for lower power consumption in battery-powered devices without sacrificing too much performance. The devices are generally expected to handle low processing capabilities, and simple network architecture and protocols that are needed to be supported by the hardware [33]. For instance, network synchronization is not supported by the majority of LPWANs, for sake of deployment simplicity and minimizing the energy consumption and the hardware cost.

In the next section, we provide a study over several LPWAN technologies and evaluate their capacity to establish a reliable communication with LEO satellite, particularly in terms of link budget feasibility.

1.3 LPWAN technologies for LEO communication

LPWAN technologies are accessible to support both licensed and unlicensed spectrum. Some examples of 3GPP cellular technologies in licensed spectrum are Long Term Evolution for Machine Type Commutation (LTE-M) and Narrow Band IoT (NB-IoT). Whereas, in the meantime, Sigfox [5] and Long Range (LoRa) [3] have reinvented connectivity for ongoing IoT ecosystem growth in unlicensed bands.

Subsequently, in this section, we give an overview on some of the latter LPWAN technologies that are potentially good candidates for satellite IoT communications. Hence, we explain at first the challenges of such communications. Then, we evaluate the capacity of each technology to overcome the constrains of the latter communications. Finally, we provide details on some of the industrial projects in the field of satellite IoT.

1.3.1 Challenges of LPWAN communication with LEO satellite

After studying the principle aspects of LEO satellite communication and giving an overview on LPWAN communication principles, we propose in this paragraph to discuss the main challenges of deploying LPWAN technologies in this context. The first challenge is the Doppler effects caused by the satellite motion with high speed. The static Doppler shift can be bypassed using several techniques. However, the Doppler time variation is a serious problem typically for long packet duration, as the case of LPWAN technologies, which provide low data rate transmissions. The second challenge is caused by the satellite FoV, which allows to connect huge number of devices. Moreover, giving the random access protocols to the radio channel, packet collisions would be very likely, which would increase the number of lost packets. Hence, this problem would degrade considerably the throughput of LPWANs and increase the energy consumption

of the nodes since lost packets are usually re-transmitted after a random period. Thereby, it is important to reduce the impact of the latter two issues in order to make LPWANs good candidates for LEO satellite communications. The third challenge concerns the capacity of LPWAN technologies to provide sufficient link budget for the latter communication.

In the next paragraphs, we will study several LPWAN technologies in licensed and unlicensed bands, and then evaluate their ability to handle the challenges of LEO satellite communications.

1.3.2 Narrow Band IoT (NB-IoT)

1.3.2.1 Principle

NB-IoT is derived from the LTE standard, therefore it supports most LTE functionalities with many simplifications and some optimizations to support long range, very low power consumption, low cost equipment, and low data rate IoT services [34, 35]. Indeed, NB-IoT is a brand-new standard for supporting long-range IoT, following the LPWAN paradigm, operating on licensed-based frequency bands, instead of the legacy cellular network one. This standard is introduced by 3GPP in 2016 for better serving IoT use cases. The downlink transmission uses the conventional Orthogonal Frequency Division Multiple Access (OFDMA) with 15 kHz subcarrier spacing (SCS), whereas the uplink transmission uses the Single Carrier Frequency Division Multiple Access (SC-FDMA) with 3,75 SCS or 15 kHz SCS. For the uplink, both single-tone (ST) and multi-tone (MT) transmissions (i.e., 3, 6, and 12 subcarriers) are supported. Thus, they can be integrated into a LTE carrier as a physical resource block (PRB) (whose width is exactly 180 kHz) that can be either allocated in-band or in the guard band. Moreover, the third frequency allocation method is called Stand-alone operation, in which the NB-IoT carrier can substitute a GSM one, whose width is equal to 200 kHz.

In order to satisfy the stringent energy consumption requirement for IoT applications served by LPWAN technologies, NB-IoT adopts some protocol enhancement like: extend Discontinuous Reception (eDRX), Power Saving Mode (PSM). Furthermore, to ensure an improved coverage, a high number of repetitions is used for initial network access and data transmission [34, 36]. Finally, to guarantee an ultra-low-complexity of the devices, they use only one receive antenna, with half-duplex operation only, and convolutional coding instead of Turbo coding on the downlink. They adopt also reduced peak data rates by limiting the maximum transport block sizes and employing the quadrature phase-shift keying (QPSK) modulation [34, 37]. Indeed, the peak data rate for NB-IoT is 26 Kbps in downlink and 66 Kbps in uplink [38].

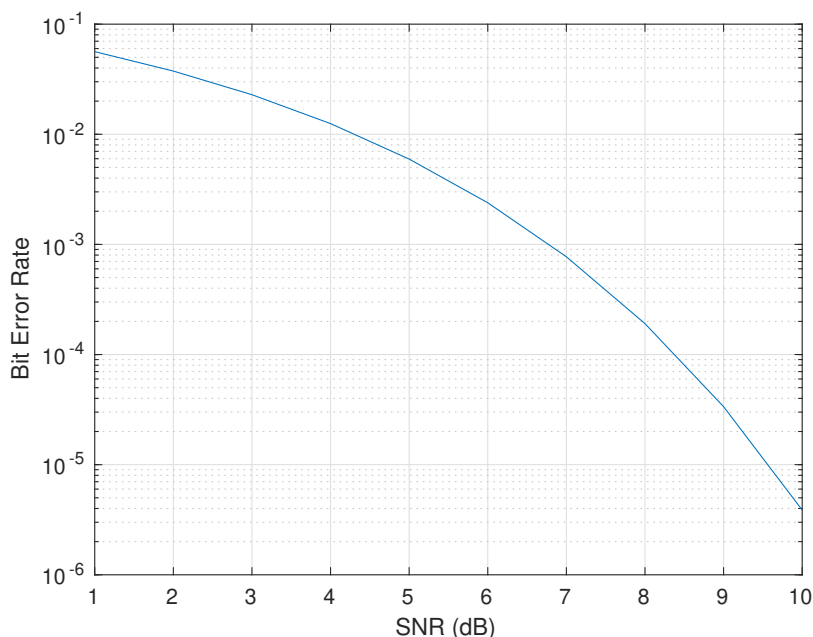


Figure 1.4: BER of NB-IoT using the uncoded QPSK modulation

1.3.2.2 Bit error rate under AWGN channel

In this paragraph, we aim to evaluate the decoding performance of NB-IoT in an uplink scenario in order to be able to measure the theoretical range limit of the latter technology.

Hence, We consider a Line of Sight (LoS) communication through an Additive White Gaussian Noise (AWGN) non-frequency selective channel. This choice is relevant giving the narrow bandwidth deployed in this standard. To note also that we consider the worst case scenario by evaluating the performance of the QPSK modulation without any further coding process.

To quantify the decoding performance of the latter modulation in these conditions, we represent in Fig. 1.4, the bit error rate (BER) as function of the signal to noise ratio (SNR). For the sake of clarity, it is worth mentioning that the SNR is computed in this simulation and the upcoming ones as $\frac{P}{\sigma_w^2}$, with P being the power of the received signal and σ_w^2 is the variance of the AWGN signal. As depicted in the latter figure, the SNR sensitivity threshold SNR_{th} is equal to 9.5 dB. This value will be used in the next paragraph to compute the receiver sensitivity. We recall here that the latter result is obtained with uncoded QPSK modulation. Hence, we evaluate the worse case scenario, and we will do the same for the other LPWAN technologies for sake of fairness.

1.3.2.3 Deployment with LEO satellite

In this paragraph, we propose to measure the receiver sensitivity using (1.10), in the case of NB-IoT uplink communication. By this measurement, we aim to validate the capacity of NB-IoT to close a link budget typical to LEO satellite communication. To this end we consider the configuration in Table 1.1:

Table 1.1: NB-IoT Parameters

$EIRP$ (dBm)	23
Carrier frequency f_c (MHz)	890
Bandwidth (kHz)	3.75, 15, 180
Subcarrier spacing (kHz)	3.75, 15
SNR_{th} (dB)	9.5
Noise Figure NF (dB)	6

As depicted in latter table the two possible subcarrier spacing is tested, in addition to the ST and the MT transmission modes. Given the latter configurations, we obtain the measurements of the receiver sensitivity S and the link budget LB , which is equal to $EIRP - S$, in Table 1.2.

Table 1.2: Receiver sensitivity and link budget for NB-IoT transmission.

Transmission mode	ST - 3.75 kHz	ST - 15 kHz	MT - 12×15 kHz
S (dBm)	-122.8	-116.73	-104.94
LB (dB)	145.8	139.73	127.94

One can notice that using the narrowest possible bandwidth with the transmission mode ST 3.75 kHz has the best link budget. Whereas, when using the largest bandwidth of 180 kHz with the transmissions mode MT 12×15 kHz, we obtain the lowest link budget, but this mode guarantees the highest data rate.

As we have already mentioned, communicating with a LEO satellite can be considered as free space LoS. Thus, given the expression in (1.9), the received power at the satellite can be written as:

$$P_{RX} = EIRP - L_{FS} - L_{At} - L_P + G_{RX} \quad (1.11)$$

Hence, to compute the maximum distance d_{max} that a NB-IoT signal could reach and still be accurately decoded, we take $P_{Rx} = S$. In addition, we consider $L_{At} = 1$ dB and $L_P = 3$ dB as typical values [39] for LEO satellite communications and $G_{RX} \in \llbracket 3, 10 \rrbracket$ dBi. By adopting the latter parameters, we represent in Fig. 1.5, the maximum range of NB-IoT without any coding scheme for the aforementioned transmission modes. It can be seen that when we increase the satellite antenna gain G_{RX} and the transmission mode (i.e. changing the bandwidth), the range of the communication is considerably improved. Moreover, we notice that only the transmission

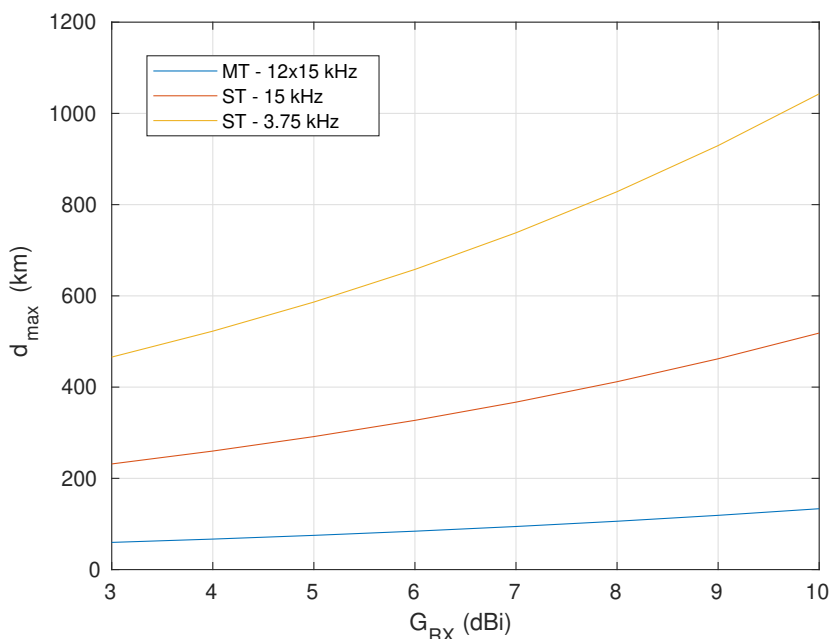


Figure 1.5: The range of NB-IoT with different transmission modes

mode ST - 3.35 kHz allows to reach a maximum distance d_{max} greater than 1000 km if $G_{RX} > 9.6$ dBi. Whereas, for the other modes, a coverage of 500 km cannot be exceeded. Hence, only the former mode can be deployed for the majority of LEO satellites which have an altitude usually less than 1000 km [40].

After studying the capacity of NB-IoT transmission to close the link budget of LEO satellite communication, we propose to discuss briefly the impact of interference, which is a serious problem in such scenario. Given that NB-IoT is deployed in licensed bands, their communications are not perturbed by interference from other technologies except for the 4G transmission since they share the same bandwidth. Fortunately, 4G uplink transmission does not have a link budget allowing to be received at LEO satellites. Subsequently, the challenge of NB-IoT is set up an efficient uplink resource scheduling, as in [41], to increase the throughput and the capacity of the network. Furthermore, the high speed motion of LEO satellites induces significant Doppler effects, resulting in inter-carrier interference. To deal with this issue several classical approaches are proposed in the literature to estimate and compensate the Doppler shift in such communication [42, 43, 44]. It is worth noting that the presence of high DR (up to 300 Hz/s) can impair the demodulation of NB-IoT signals, especially for long packet durations with the lowest data rates. Hence, in order to estimate the DR, one possibility is suggested in [43], which consists in computing the difference between the carrier frequencies at the beginning and the end of the packet.

In the next paragraph, we discuss the feasibility of deploying Sigfox [5], one of the most

popular LPWAN technologies in ISM bands, for LEO satellite communications.

1.3.3 Sigfox

Sigfox is a Toulouse-based company, founded in 2009. Its foundation gave rise to the first operator dedicated to the IoT communications. To conquer this challenge, Sigfox has developed and implemented the UNB technology. By definition, UNB systems occupy a very small part of the spectrum for signal transmission. This bandwidth (typically a few hundreds of Hz) is very small compared to the channel bandwidth. The first system of this type, based on VMSK (Very Minimum Shift Keying) modulation, was proposed in 2004 [45, 46]. The objective was to compress the data transmission into the smallest possible bandwidth. However, in practice, this technique did not allow to reach the very low occupation as announced, which leads Sigfox to propose another proprietary approach.

1.3.3.1 Principle

The UNB PHY layer used by Sigfox is based on a Differential Binary Phase Shift keying (DBPSK) modulation in uplink and Gaussian frequency shift keying (GFSK) in downlink, to transmit data at a very low rate (100 bps in uplink and 600 bps in downlink) in the 868 MHz ISM band in EU [47]. The transmitted signal therefore occupies a band of about 100 Hz around the carrier, within an available band of several hundreds of kHz (as an example 192 kHz in 868 MHz ISM bands in EU).

The UNB guarantees a very large coverage with a single base station (several tens of kilometers in terrestrial communications), with a low energy consumption. In theory, in free space LoS communications, the link budget makes it possible to evaluate the coverage to several hundreds of kilometers. However, in a real environment, the observed range is of 60 km. Moreover, the low spectral congestion allows for the simultaneous transmission via a very large number of nodes, thus meeting the needs of the IoT market. Thereby, the low spectral occupation also makes the technology resistant to interference, which is a key feature in the ISM band.

In the uplink scenario with a data rate up to 100 bps, a maximum number of 140 messages per day or almost 1 message every 10 minutes can be send. The payload size limit is set at 12 octets which is enough to transmit small and infrequent data [5]. Deploying narrow bandwidth and low rate to transmit information permits to Sigfox to improve reliability and alleviate the detrimental effects of interferences arising from jamming, multi-path propagation and the multiple-access communication on the same channel. Moreover, in order to decrease the data loss probability, at a cost of a shorter battery life for battery powered applications, the same Sigfox packet is transmitted three times in sequence on random carrier frequencies. For instance, in EU there are 333 Sigfox channels of $B_{sig} = 100$ Hz each in the ISM bands between

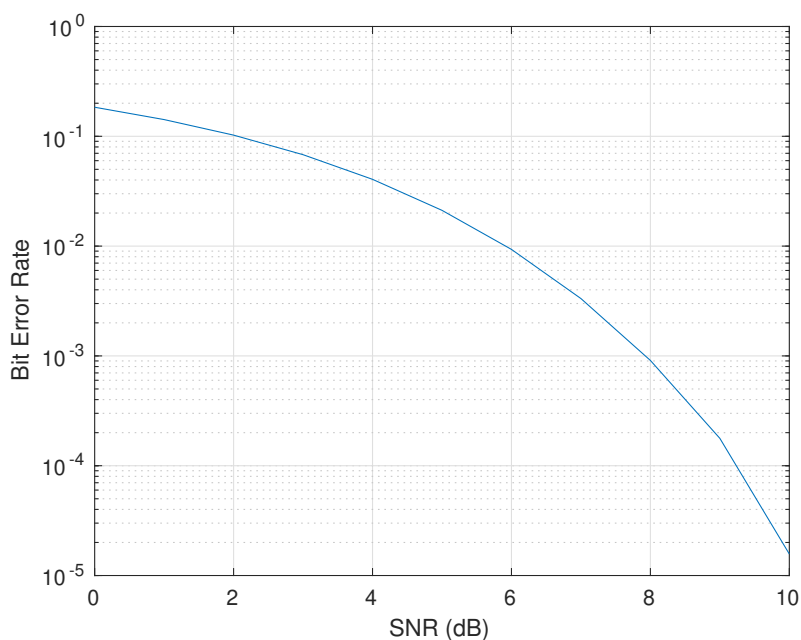


Figure 1.6: BER Sigfox DBPSK on AWGN channel

868.034 MHz and 868.226 MHz [47], and a frequency hopping is supported using a pseudo-random method of 3 out of the latter channels. Furthermore, the access to the channel is done in a random way in time (Aloha-based protocol), but also in frequency, leading to a protocol called Random Frequency and Time Division Multiple Access (RFTDMA).

In order to guarantee a high QoS, a spacial diversity is also implemented. Indeed, uplink messages are decoded by all the base stations within the range and the duplicates are then processed in the core network. Finally, after transmitting a message, a downlink transmission is available if needed.

1.3.3.2 Bit error rate under AWGN channel

In this paragraph, we aim to evaluate the decoding performance of Sigfox in an uplink scenario in order to be able to measure the theoretical range limit of this UNB technology.

To this end, we consider a LoS communication through an AWGN channel.

Given the use of the DBPSK modulation, the BER of Sigfox as function of the SNR, which is computed as previously detailed in the case of NB-IoT, is given in Fig. 1.6.

As we can see in the latter figure, the SNR sensitivity threshold SNR_{th} , which is the minimum SNR that gives a BER lower than 10^{-5} , is equal to 10 dB. The latter value will be used in the next paragraph to compute the receiver sensitivity.

1.3.3.3 Deployment with LEO satellite

In this paragraph, we propose to compute the receiver sensitivity using (1.10), in the case of Sigfox uplink communication. By these measurements, we aim to validate the capacity of Sigfox end-devices to communicate with LEO satellite, given the constraint of maximum transmitted power as defined by regulations in ISM free bands [31]. Finally, we discuss the robustness of the former technology against interference and Doppler effects.

If we consider the bandwidth B_{sig} , $SNR_{th} = 10$ dB and $NF = 6$ dB, the latter sensitivity is equal to -138 dBm. This value of sensitivity is very low and allows Sigfox end-devices to communicate with very long range.

To compute the link budget of Sigfox uplink communication, we consider the parameters in Table 1.3: Hence, the link budget is equal to $LB = EIRP - S = 152$ dB.

Table 1.3: Sigfox Parameters

EIRP	f_c	S
14dBm	868MHz	-138dBm

Hence, to compute the maximum distance d_{max} that a Sigfox signal could attend and still be accurately decoded, we consider $P_{RX} = S$ in (1.11). In addition, we consider $L_{At} = 1$ dB and $L_P = 3$ dB as typical values [39] and $G_{RX} \in \llbracket 3, 10 \rrbracket$ dBi. The measurement results are given in Fig. 1.7. We notice that when we increase the satellite antenna gain G_{RX} , the range of the communication is considerably improved. For instance, the maximum distance d_{max} that could be reached by a Sigfox transmission is greater than 1000 km if G_{RX} is above 3.2 dBi. This range is quite sufficient to establish Sigfox communications with LEO satellite since the altitude of LEO is usually less than 1000 km [40].

Furthermore, in order to be compliant with LEO satellite communication, Sigfox signals should be resilient to inter and intra-technology interference. Indeed, The UNB aspect of Sigfox allows to considerably reduce the impact of intra-system interference. Each UNB message uses a very small bandwidth, which guarantees high spectrum efficiency. More messages can hence fit into an assigned frequency band without overlapping with each other, enabling more devices to effectively operate at the same time without interfering with each other. This improves overall network capacity and system scalability. Whereas, to improve the resistance of Sigfox transmissions against inter-system, frequency hopping helps avoiding congested channels and makes signals difficult to intercept. However, the main advantage of UNB signals, their small bandwidth, makes them more sensitive to frequency drifts that are particularly present in the case of LEO satellite systems. Hence, Sigfox transmissions are done using time/frequency random access techniques, where the carrier frequency is a parameter unknown by the receiver. In addition, the DR in such communications is in the order of hundreds of hertz per second,

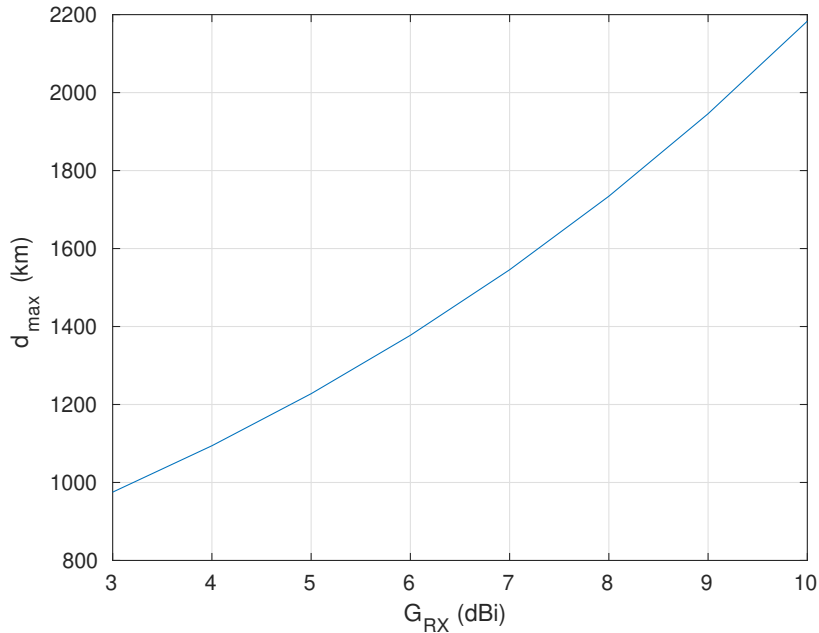


Figure 1.7: Range of Sigfox uplink transmissions as function of the satellite antenna gain G_{RX} , with $B_{sig} = 100$ Hz and $EIRP = 14$ dBm.

which is in the same order of an UNB signal bandwidth [48]. The change of frequency over the packet duration caused by the DR would, on the one hand, increases the probability of packet collision, but on the other hand, the collisions are less destructive since two superposed signals are rarely completely overlapping in this case. A detailed study on the impact of intra-system collision when considering LEO satellite communications using UNB signals is provided in [48]. Finally, in order to achieve the theoretical sensitivity claims when using Sigfox technology, it is mandatory to estimate the Doppler shift and DR. To conquer this challenge several algorithms are proposed in the literature, for instance we cite the one detailed in [49].

In the next paragraph, we will provide a study on LoRa, one of the most popular LPWAN technologies and Sigfox’s major competitor in the ISM bands.

1.3.4 LoRa - Chirp Spread Spectrum

The name, LoRa [3], is a reference to the extremely long-range data links that this technology enables. This technology was developed by a french company called Cycleo, and then acquired and patented by Semtech [3] which is at present selling LoRa chips. LoRa provides for long-range communications: up to several kilometers in urban areas, and up to 15 kilometers or more in rural areas. A key characteristic of the LoRa-based solutions is ultra-low power requirements, which allows for the creation of battery-operated devices that can last for up to 10 years. Deployed in a star topology, a network based on the open LoRaWAN [50] protocol is perfect for

applications that require long-range or deep in-building communication among a large number of devices that have low power requirements and that collect small amounts of data [51].

1.3.4.1 The LoRa modulation

LoRa PHY layer is based on the Chirp Spread Spectrum (CSS) modulation, which relies on sine waves whose instantaneous frequency evolve linearly with time over a specific bandwidth B . These specific waves are called chirps. A raw chirp frequency varies linearly from an initial frequency f_i to a final frequency f_f during the symbol time T , with $B = |f_f - f_i|$. When $f_i > f_f$, the chirp is considered as down chirp while it is considered an up chirp otherwise. To note here that the CSS waveform has a constant envelop, which reduces the energy consumption of the transmitter.

Initially, the binary information flow to transmit is divided into subsequences, each of length SF . The set of SF consecutive bits constitutes a symbol. The number of possible symbols is hence equal to $M = 2^{SF}$. $SF \in \{7, \dots, 12\}$ indicates the spreading factor and the relation between the bit rate D_b and the symbol rate D_s can be written as: $D_s = D_b/SF$.

For digital communication systems with no spreading spectrum, the bandwidth used by the transmitted signal is proportional to the symbol rate. The coefficient of proportionality that depends on the shaping filter, which is in general a half Nyquist one. In CSS, the signal bandwidth is fixed by B which has the following relationship with T [52]:

$$M = B \times T.$$

Hence, as depicted in Fig. 1.8, for a fixed bandwidth, we can deduce that an increase of SF leads to a longer symbol duration (i.e. increasing the SF by 1 doubles the symbol duration). Subsequently, the highest SF has the lowest data rate. However, as we will see later, the more we spread the signal over time (i.e. increasing the symbol time), the more we increase the communication range. More details on the LoRa PHY layer, especially the modulation and demodulation of the symbols, will be revealed in the next chapter.

1.3.4.2 Bit error rate under AWGN channel

In this paragraph, we aim to evaluate the decoding performance of LoRa PHY layer in an uplink scenario in order to be able to measure the theoretical range limit of this technology.

As previously, we consider a communication through a non-frequency selective channel. Thus, in a perfect synchronization case without any interferences, the received signal is only disturbed by the receiver AWGN signal. Given this use-case, we represent in Fig. 1.9, the BER of LoRa signal, as function of the SNR, for all the possible SFs . As previously mentioned, the decoding

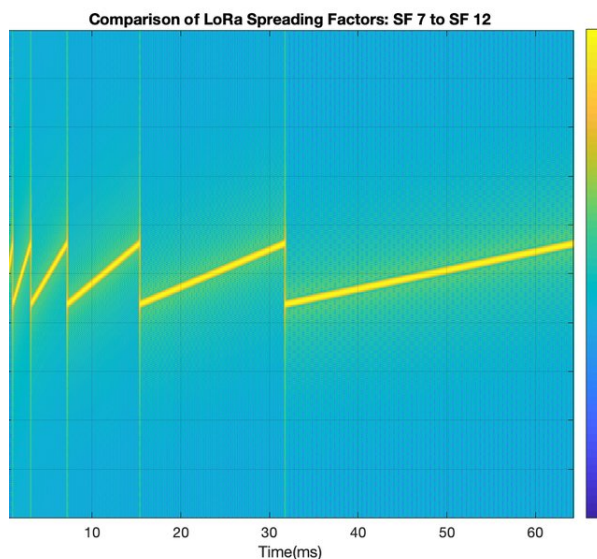


Figure 1.8: LoRa CSS modulation; raw up chirps representation for $SF \in \{7, \dots, 12\}$ with a bandwidth of 125 kHz. From the left to the right the SF is increased by 1.

performance of LoRa signals depend on the value of the SF . Many works in the literature [52], provided the theoretical models of the BER and proved that increasing the SF leads to a lowering of the SNR sensitivity threshold, and thus a greater communication range.

One can notice in Fig. 1.9 that increasing the SF by 1 can improve the processing gain by almost 3dB. The results prove that the higher the SF , the further the communication can go.

1.3.4.3 Deployment with LEO satellite

In this paragraph, we aim to measure the link budget of LoRa uplink communication, then, prove the possibility to establish reliable communication with LEO satellites. To this end, we represent in Table 1.4, the receiver sensitivity for each SF , which are obtained using the SNR sensitivity thresholds deduced from Fig. 1.9. To note here that the sensitivity thresholds

Table 1.4: Receiver sensitivity for each SF ,

SF	Bandwidth (kHz)	SNR_{th} (dB)	Receiver sensitivity (dBm)
7	125	-6	-123
8	125	-9	-126
9	125	-12	-129
10	125	-15	-132
11	125	-17.5	-134.5
12	125	-20	-137

depicted in Table 1.4 are the same than the ones of LoRa chip SX1276. It worth noting here

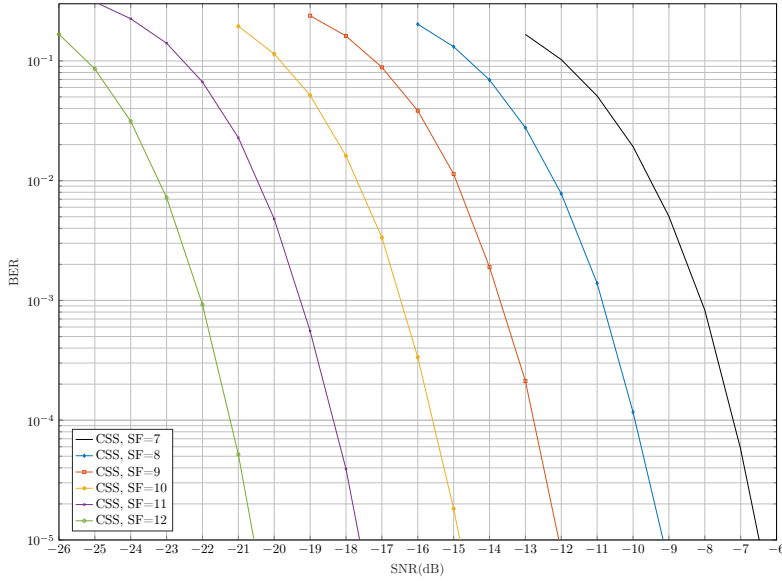


Figure 1.9: BER of CSS in a perfect synchronization case

that the receiver sensitivity are reduced in the new LoRa chips, which is down to -148 dBm [53]. If we consider the EIRP of transmitted LoRa signal equals to 14 dBm, we obtain the measurements of the link budget for each SF are given in Table 1.5:

Table 1.5: Link budget for LoRa signal with $B = 125$ kHz and EIRP = 14 dBm.

SF	7	8	9	10	11	12
LB (dB)	137	140	143	146	148.5	151

After computing the link budget for each SF , we propose to measure the maximum distance d_{max} that a LoRa signal could reach while maintaining accurate decoding performance. To this end, we considered the same configuration as in (1.11). The ranges of all SF 's as function of G_{RX} , with $B = 125$ kHz, are given in Fig. 1.10. To note here that we considered the same link losses (i.e. L_{At} and L_P) configuration as in the case of Sigfox transmission.

Based on the results in Fig. 1.10, we deduce that when we consider $B = 125$ KHz and $EIRP = 14$ dBm, only $SF12$, $SF11$ and $SF10$ can be deployed with the majority of LEO satellite, since they have a range that exceed 1000 km for G_{RX} equal to 4.2 dBi, 6.7 dBi and 9.2 dBi respectively. Moreover, if we reduce the bandwidth B other SF 's could be deployed, as will be proved in the next chapter.

The second challenge of LEO satellite communication is the high probability of packet collisions given the huge number of end-devices that can be connected. In this context, LoRa, with its CSS modulation, is resilient to narrowband and UNB interference. As will be proved in Chapter 3, the decoding performance of LoRa signals are more degraded as long as we increase the bandwidth of the interfering signal. Whereas, the severe issue of LoRa-based networks is the

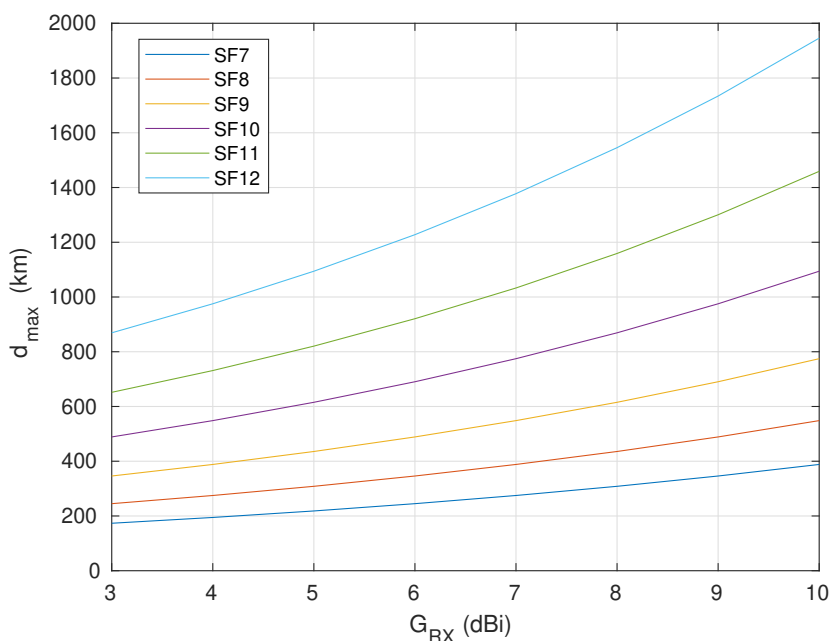


Figure 1.10: Range of LoRa uplink transmissions as function of the satellite antenna gain G_{RX} , with $B = 125$ kHz and $EIRP = 14$ dBm.

intra-technology interference. Indeed, two signals having different SF are almost orthogonal. However, if two or more signal are simultaneously received with the same SF over the same channel, a destructive collusion occurs. Thus, it is very likely that all the collided packets must be re-transmitted unless the capture effect is deployed. Indeed, if the received packet has a power 6 dB greater than the interfering signal, its information can be retrieved using the capture effect [54, 55, 56, 57, 11]. The interference issue in LoRa will be extensively studied in Chapter 3.

The third challenge of of LEO satellite communication is the Doppler effects. In this context, LoRa-like signals face serious problems to overcome this issue, especially for signals having the largest symbol time (i.e. larger SF for a defined bandwidth B), and hence lower data rate and larger time on air. Indeed, if the common LoRa bandwidth $B = 125$ kHz is used, the decoding performance of the highest SF s (i.e. $\{10, 11, 12\}$) are considerably impacted by the Doppler time-variation. These results will be proved in the next chapter and are discussed in [58]. However, as already mentioned, with $B = 125$ kHz, only $SF12$, $SF11$ and $SF10$ have a link budget allowing to communicate with LEO satellites. Thus, several treatments should be introduced to the former configurations to bypass the impact of the DR. Furthermore, the synchronization algorithms deployed LoRa-like receivers are accurately performed only if the carrier frequency offset do not exceed the quarter of the bandwidth B . Nevertheless, with the significant values that can be reached by the Doppler shift, it is very likely that the latter offset

Region	European Union (ETSI, 863-870 MHz)				United States (FCC, 902-928 MHz)	
	DR8	DR9	DR10	DR11	DR5	DR6
LoRaWAN data rate alias	7	4	7	4	8	
LR-FHSS number of channels	137		336		1523	
LR-FHSS OCW (kHz)	488					
LR-FHSS OBW (Hz)	488					
Minimum separation between LR-FHSS hopping carriers (kHz)	3.9				25.4	
Number of physical carriers available for frequency hopping in each OCW channel	280 (8x35)		688 (8x86)		3120 (52x60)	
Number of physical carriers usable for frequency hopping per end-device transmission	35		86		60	
Coding rate	1/3	2/3	1/3	2/3	1/3	2/3
Physical bit rate (bits/s)	162	325	162	325	162	325
Max. MAC payload size (bytes)	58	123	58	123	125	125
Max. MAC payload fragments	61	64	61	64	130	65
Header replicas	3	2	3	2	3	2
PHY header duration per replica (seconds)	0.233	0.233	0.233	0.233	0.233	0.233
PHY time on air (seconds)	0.70 + 3.06	0.47 + 3.19	0.70 + 3.06	0.47 + 3.19	0.70 + 6.48	0.47 + 3.24

Table 1.6: LR-FHSS main specifications and parameters for EU and US regions [60, Table. 1].

exceeds $\frac{B}{4}$, especially if a bandwidth lower than 125 kHz is used.

In the following paragraph, we will examine the new PHY layer LR-FHSS, which was patented by Semtech in order to increase the capacity of networks using the LoRaWAN protocol.

1.3.5 Long Range-Frequency Hopping Spread Spectrum

1.3.5.1 Principle

Long Range-Frequency Hopping Spread Spectrum (LR-FHSS) [59, 60] is an extension of the LoRa physical layer that has been recently announced by Semtech, and will be supported on their chips SX1261 and SX1262. This new PHY layer is designed to address extremely long-range and large-scale communication scenarios, such as satellite IoT. This PHY layer is based on Frequency Hopping Spectrum (FHSS) to increase the network capacity in dense deployments and it is deployed only in the uplink. In the downlink, the current LoRa PHY layer based on CSS modulation is employed. The end device listens on a full channel bandwidth with the ALOHA channel access mechanism and the gateway is then able to gather the complete payload with the information contained in the header.

- **LR-FHSS channels and sub-carriers**

With LR-FHSS, the frequency band is split into different Operating Channel Width (OCW). Each OCW represents a grid of several Occupied Band Width (OBW) of 488 Hz each. LR-FHSS transmissions are divided in different data-rates (DR) which are detailed in Table 1.6. Depending on the used DR, the division of the bandwidth is different to complies with EU or North America policies. For instance, in the DR8 of EU, each OCW is divided into 8 grids of 35 OBW sub-carriers, then, to comply with EU policies, those carriers are separated from 3.9kHz.

- **LR-FHSS packet transmission**

A LR-FHSS packet is composed of a SyncWord, a PHY Header, a payload, and the payload Cyclic Redundancy Check (CRC). The uplink device first sends 2 or 3 replicas of the PHY Header depending on the DR at a fixed bit rate for a duration of 0.233 s. Those replicas are sent on different sub-carriers to minimize the collision probability and increase the reception probability. A header contains all information to gather all the fragments of a packet. This includes, payload length, DR, number of header replicas and coding rate. Contrary to the PHY Header, one copy of the packet payload is transmitted and split into fragments of a fixed duration of ~ 50 ms.

- **Frequency Hopping**

Every device sending LR-FHSS packets owns a 9-bit random number x used to compute the frequency hopping sequence. The device first select an available grid randomly to send a packet. Then, for every fragment, the device computes an input

$$i_k = x + k \times 2^{16}$$

where k is the fragment number. Every input i_k is then processed in a 32-bit hash function to get a pseudo random (PR) number which is taken modulo the number of OBW per grid (35 in DR8 for example). The list of generated numbers is then multiplied by the minimum distance between 2 sub-carriers (3.9 kHz in Europe as an example) to comply with European or North America policies.

1.3.5.2 Bit error rate under AWGN channel

LR-FHSS is a new PHY layer, so few details about the digital modulation are revealed [59, 60]. Thereby, to evaluate the decoding performance of this technology and thus measure its link budget, we did a reverse engineering work. Indeed, we knew from [59] that LR-FHSS deploys a one bit per symbol digital modulation and has a link budget similar to the one of LoRa with $SF = 12$ and $B = 125$ kHz. Thereby, we represent in Fig 1.11, the BER as function of $\frac{E_b}{N_0}$ of several digital modulations, using the Viterbi (hard and soft) decoder [61] and the occupied bandwidth is 488 Hz. To note that E_b is the energy per bit and N_0 is the noise spectral density. Hence, $\frac{E_b}{N_0}$ is defined as the normalized signal to noise ratio (SNR), or SNR per bit. Subsequently, $\frac{E_b}{N_0} = \frac{\text{SNR}}{\rho}$, with ρ is the spectral efficiency. In this case, all the tested digital modulations have one bit per symbol, hence, ρ is equal to 1 bps/Hz. It worth noting also that the code rate and the constraint length for the convolutional code are well known and are respectively equal to $\frac{1}{3}$ and 8. The latter parameters are extracted from [62].

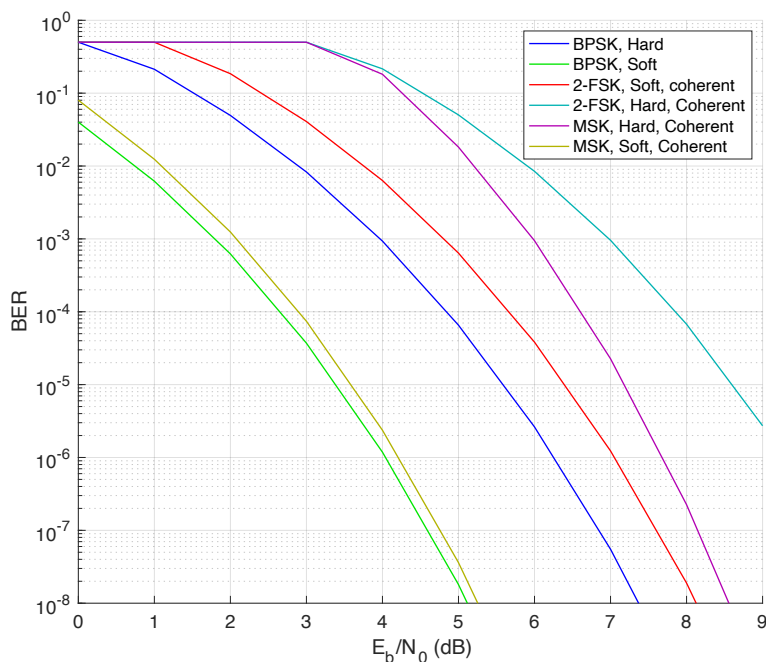


Figure 1.11: BER of possible modulations used in LR-FHSS.

As we can see in Fig. 1.11, the BPSK and MSK modulations, with Viterbi soft decision decoder, have the better performance. We notice that their SNR sensitivity threshold is equal to 3.5 dB, which gives a receiver sensitivity of -137.6 dBm when $B = 488$ Hz.

1.3.5.3 Deployment with LEO satellite

In the previous paragraph, we showed that BPSK and MSK modulations, with Viterbi soft decision decoder, have the best decoding performance among the tested digital modulations. Moreover, we proved that their receiver sensitivity is almost equal to LoRa transmission with $SF = 12$ and $B = 125$ kHz. In the previous subsection, we demonstrate that using the latter configuration have a link budget allowing to establish reliable communication with LEO satellites.

LR-FHSS is proposed by Semtech to expend the use of LoRaWAN worldwide, especially by focussing in satellite IoT connectivity. Thus, this PHY layer features high interference resistance that alleviate packet collisions by increasing spectral efficiency with the uplink frequency hopping modulation. Indeed, by breaking up each data packet into small pieces randomly spreading them over a defined frequency bandwidth, it is possible to considerably increase the number of simultaneous connection, with a low probability of packet collisions. LR-FHSS can support millions of end nodes and delivers a new level of reliability for IoT services [63]. Furthermore, in the case of LR-FHSS communications, the Doppler shift should be estimated in order to identify the first received fragment of the payload and then all the other ones are

recognized using the hopping sequence depicted in the PHY header. In addition, given the deployment low data rates as shown in Table 1.6, the high values of DR could impair the identification process of the payload fragments.

In the next paragraph, we present several industrial IoT projects in the field of via LEO satellites in order to highlight their world-wide omnipresence.

1.4 Industrial IoT deployments in LEO satellite communication

Several industrial IoT LEO constellation projects exist worldwide. A detailed description of each industrial IoT LEO constellation project can be seen in Table 1.7. The information was obtained from NewSpace's index and Celestrak's satellite catalog (SATCAT) [64].

With regard to the company geographical distribution, one can observe that these projects are carried by companies from 24 different countries (see Figure 1.12).

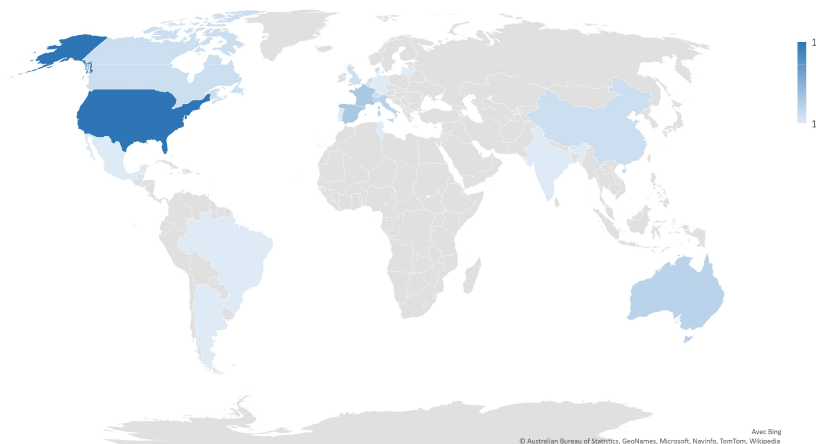


Figure 1.12: Geographical distribution of the industrial IoT LEO constellation projects

It is to be noted that slightly more than half of the projects (56%) are devoted solely to IoT / M2M while the rest of them (44%) have complementary application fields (Internet, Earth observation, AIS, etc.).

In terms of progress phase, most of the projects (65%) are either in the prototype development phase or in the prototype launch phase and only one of the constellations (OrbComm's OG2) is in its final stage. A status summary of the existing constellation projects is presented below :

- Concept : 1
- Early Stage : 5

Chapter 1. Dedicated LPWA Technologies for LEO satellite communication

Company (Constellation name)	Country	Fields	Status	Form factor	Launched	Satellites names
Aistech Space (DANU, HYDRA)	Spain	IoT / M2M, ADS-B, AIS, IR imaging	Prototype(s) launched	2U, 6U	2 / 150	AISTECHSAT-2 (2018) AISTECHSAT-3 (2019)
Alya Nanosatellites	Brazil	Earth observation, IoT / M2M	Early stage	6U	0 / ?	-
Artemis Space (BEACON)	Cyprus	IoT / M2M	Concept (Dormant?)	CubeSat	0 / ?	-
AstroCast	Switzerland	IoT / M2M	Prototype(s) launched	3U	7 / 80	ASTROCAST 0.1 (2018) ASTROCAST 0.2 (2019) ASTROCAST-0101 (2021) ⋮ ASTROCAST-0105 (2021)
AT&T	US	IoT / M2M	Prototype development	CubeSat?	0 / ?	-
BHDynamics	Spain	IoT / M2M	Early stage	PocketQube	0 / ?	-
Bitlinq Space	Netherlands	Internet, IoT / M2M	Unknown	CubeSat?	0 / ?	-
Blink Astro	US	IoT / M2M	Prototype(s) launched	3U	1 / ?	M6P (2019)
Commsat	China	Internet, IoT / M2M, AIS	Prototype(s) launched (Cancelled?)	Microsat, 6U, 3U	8 / 72	Juvenile LadyBird-2 ⋮ LadyBird-7
Elbit Systems (NANOVA)	Italy	IoT / M2M	Prototype(s) launched	3U	1 / ?	TYVAK-0092 (2019)
Eutelsat (CubeSats)	France	IoT / M2M	Prototype(s) launched	3U, CubeSat	1 / 25	TYVAK-182A (2021)
Fleet Space	Australia	IoT / M2M	Prototype(s) launched	3U, 12U, 1.5U, 6U	5 / 100	PROXIMA I (2018) PROXIMA II (2018) CENTAURI-1 (2018) CENTAURI-2 (2018) CENTAURI-3 (2021)
Fossa Systems	Spain	IoT / M2M	Prototype development	PocketQube	1 / ?	FOSSASAT-1 (2019)
German Orbital Systems	Germany	IoT / M2M	Prototype(s) launched	3U	4 / ?	ISAT (2018) D-STAR ONE (SPARROW) (2018) D-STAR ONE (LIGHTSAT) (2019) D-STAR ONE (EXOCONNECT) (2019)
GomSpace	Denmark	IoT / M2M, SSA	Cancelled	6U	0 / 10	-
GP Advanced Projects (FEES Cluster)	Italy	IoT / M2M	Prototype(s) launched	0.25U	0 / ?	FEES (2021)
Gravity Space	US	IoT / M2M	Prototype development	16U	0 / ?	-
Guodian Gaoke (Apocalypse)	China	IoT / M2M	Being launched	6U	10 / 38	TIANQI-1 TIANQI-2 TIANQI-3 TIANQI-4A TIANQI-4B TIANQI-5 (2020) TIANQI-6 (2020) TIANQI-8 (2020) TIANQI-12 (2021) TIANQI-14 (2021)
Helios Wire (EchoStar)	Canada	IoT / M2M	Prototype(s) launched	6U, 16U	2 / 30	Helios Wire BIU SIRION PATHFINDER-2 (2018)
Hiber	Netherlands	IoT / M2M	Prototype(s) launched	6U, 3U	4 / 48	HIBER-1 (2018) HIBER-2 (2018) HIBER-3 (2021) HIBER-4 (2021)
Innova Space (Libertadores de América)	Argentina	IoT / M2M	Early stage	PocketQube	0 / 100	-
Kepler Communications	Canada	Store-and-Forward, IoT / M2M, Internet	Being launched	3U, 6U, ?	15 / 360	KIPP (2018) KEPLER-1 (2018) ⋮ KEPLER-15 (2021)
Kineis (CLS)	France	IoT / M2M, AIS	Prototype development	Microsat	0 / 15	-

Chapter 1. Dedicated LPWA Technologies for LEO satellite communication

Company (Constellation name)	Country	Fields	Status	Form factor	Launched	Satellites names
Lacuna Space	UK	IoT / M2M	Being launched	3U, 6U	5 / 240	M6P (2019) R2 (2020) Faraday-1* LACUNASAT-3 (2020) LACUNASAT-2B (2021)
Lynk	US	IoT / M2M, Internet, Direct-to-phones, Satellite-to-cell	Prototype(s) launched	Hosted, CubeSat?	1 / 1000	ULTP (2020)
Mission Space	Latvia	Space Weather, IoT / M2M	Early stage	?	0 / ?	-
Myriota	Australia	IoT / M2M	Prototype(s) launched	3U	2 / 50	BRIO (2018) MYRIOTA 7 (TYVAK-0152) (2021)
NanoAvionics	Lithuania	IoT / M2M, Constellation-As-A-Service	Prototype development	6U, 12U?	3 / 72	LITUANICASAT-2 (2017) M6P (2019) R2 (2020)
NuSpace	Singapore	IoT / M2M	Prototype development	CubeSat	0 / ?	-
Omnispace	US	IoT / M2M, 5G	Prototype development	12U	0 / 200	-
OQ Technology	Luxembourg	IoT / M2M	Prototype development	CubeSat, 1U?	0 / ?	-
Orbcomm (OG2)	US	IoT / M2M, AIS	Launched and replenishing	Microsat, Smallsat,	60 / ?	ORBCOMM-X (1991) ORBCOMM FM01 (1995) ⋮ ORBCOMM FM41 (2008) ORBCOMM OG2 (2012) ORBCOMM FM103 (2014) ⋮ ORBCOMM FM119 (2015)
Orbitare (space Loop)	Switzerland	IoT / M2M	Early stage	CubeSat	0 / ?	-
Prométhée	France	Earth observation, IoT / M2M	Prototype development	CubeSat?	0 / ?	-
Ragnarok Industries	US	Internet, IoT / M2M	Cancelled	CubeSat	0 / ?	-
SAS (Sky and Space)	UK, Australia	IoT / M2M	Prototype(s) launched (Cancelled?)	8U, 6U, 3U	3 / 200	DIAMOND RED (2017) DIAMOND GREEN (2017) DIAMOND BLUE (2017)
Sateliot	Spain	IoT / M2M, Direct-to-phones, Satellite-to-cell	Prototype(s) launched	3U	1 / 100	3B5GSAT (SATELIOT 1) (2021)
Space JLTZ (Gemini)	Mexico	Earth observation, Hyperspectral, IoT / M2M	Prototype development	6U	0 / 200	-
Sternula (MARIOT)	Denmark	VDES, IoT / M2M, AIS	Prototype development	CubeSat?	0 / 50	-
Swarm Technologies	US	IoT / M2M	Being launched	0.25U, 1U	93 / 600	SPACEBEE-1 (2018) ⋮ SPACEBEE-87 (2021) SPACEBEENZ-1 (2020) ⋮ SPACEBEENZ-6 (2020)
Tekever	Portugal	Earth observation, AIS, ADS-B, IoT / M2M	Prototype development	Microsat	0 / 12	-
Telnet	Tunisia	IoT / M2M	Prototype(s) launched	3U	1 / 30	CHALLENGE ONE (2021)
Totum Labs	US	IoT / M2M	Prototype development	CubeSat?	0 / 24	-
Tyvak	US,Italy	IoT / M2M	Cancelled	CubeSat	0 / ?	-
4Skies	France	IoT / M2M	Cancelled	Microsat	0 / ?	-
Dunvegan Space Systems (BitSat)	US	IoT / M2M, Data storage	Cancelled	3U	0 / 24	-
Vesta Space Technology	India	IoT / M2M, 5G, Internet	Prototype development (Cancelled?)	?	0 / 35	-

Table 1.7: Industrial IoT LEO Deployments

- Prototype development : 14
- Prototype(s) launched : 17
- Being launched : 4
- Launched and replenishing : 1
- Cancelled : 5
- Unknown : 1

It is important to precise that these IoT constellations are not the only ones to be put into the LEO orbit. Indeed, they come in addition to other projects such as:

- *OneWeb* (UK-Bharti-Eutelsat) is a company whose project is to develop a global communications network powered by a constellation of 650 LEO satellites. A total of 182 satellites have been deployed so far and the network is operational.
- *Starlink* (SpaceX) is a LEO satellite internet constellation. Currently, more than 1,600 satellites have been put in orbit and the goal is to have 42,000 in space by mid-2027. Internet service is already available in six countries and is expected to reach global coverage by the end of 2021.

1.5 Conclusion

In this chapter, we discussed the fundamental aspects of LEO satellite communications. Given the constraint of communicating in ISM band (i.e. maximum transmitted power and duty cycle), we proved that several LPWAN technologies have a link budget allowing to establish a reliable communication in this scenario. Furthermore, we discussed the challenges of deploying LPWAN technologies to communicate with LEO satellite. The first challenge is to maintain accurate decoding performance in the presence of significant Doppler effects, especially the Doppler time variation, which will considerably impact the decoding process giving the long duration of LPWAN packets. Whereas, the second challenge is caused by the field of view of LEO satellite, which allows to connect a massive number of end-devices. Moreover, giving the random access deployed in the majority LPWAN technologies, the probability of packet collisions will be very high. These collision will make the packet loss more likely, which would reduce the throughput of LPWANs and increase the energy consumption of the end-devices since lost packets should be re-transmitted.

As a summary, we represent in Table 1.8 the capacity of each from the aforementioned LPWAN technologies to bypass the constraints of LEO satellite communications. As we can

Table 1.8: Related works comparison

LPWAN \ KPI	Verify LEO satellite Range	Robustness to Doppler shift	Robustness to DR	Robustness to interference
NB-IoT	✓	to be compensated	to be compensated	✓
Sigfox	✓	to be compensated	to be compensated	✓
LoRa	✓	to be compensated	good for some configurations	to improve in intra-technology interference
LR-FHSS	✓	to be compensated	to be compensated	To be verified

see in the latter Table, Sigfox and LR-FHSS can be deployed in LEO satellite communication in free ISM bands since they overcome the three aforementioned principle constraints. Hence, LR-FHSS is proposed by Semtech as an alternative PHY layer of LoRa, that can be deployed for the uplink communication with LEO satellites.

Currently, the lowest data rates in LoRa, that allow to close the link budget of a LEO satellite communication, can not be deployed due to their high sensitivity to the DR. To deal with this issue, an alternative proposed by Swarm is to incorporate LoRa on Very High Frequency (VHF) frequencies for uplink and downlink communications [4] and deploy high power LoRa-like transmissions with the highest data rates (e.g. $SF = 7$ with $B = 125$ kHz), which have good robustness to the DR as will be proved lately in the next chapter. This method allows to close the link budget of LEO satellite communications, but can not be used in ISM free bands due to the maximum transmitted power limitation. Subsequently, it is important to implement synchronization algorithms allowing all the configurations in LoRa, especially the lowest data rates to be more resilient to the DR. Hence, in the next chapter, we provide several algorithms to deal with the latter problem using LoRa-like signals.

CHAPTER 2

LoRa-like synchronization approaches for LEO satellite communications

In the previous chapter, we have discussed the fundamental aspects of LEO satellite communications and we provided an overview on several LPWAN technologies used in this purpose. We showed that several PHY layers can fulfill the requirements of the latter communication in terms of link budget, energy consumption and resilience to interference and Doppler effects. In this chapter, we will focus on a well known LoRa-like PHY layer using the chirped signals. In particular, we detail in Section 2.1, the modulation and demodulation principles in LoRa PHY layer. Then, in Section 2.2, we formalize the impact of imperfect synchronization on the symbol estimation of LoRa-like signals. Based on these models, we discuss in Section 2.3 several synchronization approaches from the literature using a specific preamble. It will be seen that the current synchronization algorithms lead to a constraint on the maximum carrier frequency offset (CFO) estimable equals to the quarter of the bandwidth. To alleviate this constraint, we propose in Section 2.4, a modification of the LoRa PHY layer which we refer to as differential CSS (DCSS). We will demonstrate the capacity of this proposed technique to enhance the robustness against Doppler effects (i.e. Doppler shift and DR) compared to the conventional CSS modulation. It should be noted that the synchronization approaches in the literature did not deal with the DR, which is the case when communicating with a LEO satellite. Thereby, based on the DCSS technique, two transceivers suited for the LEO satellite communications are proposed in sections 2.5 and 2.6.

2.1 LoRa PHY layer

In this section, we propose a more detailed study on the LoRa PHY layer than the one presented in the previous chapter. To this end, We will present the process of generating the modulated chirps. Then, we will provide the demodulation principle in LoRa when perfect time and frequency synchronizations are considered.

2.1.1 Modulation

As already explained, LoRa PHY layer is based on the CSS modulation. Initially, the binary information flow generated from the MAC layer is divided into subsequences, each of length SF bits which constitute a symbol. The number of possible symbols is hence equal to $M = 2^{SF}$. To distinguish between the M different symbols of the constellation, M orthogonal chirps have to be defined so that each symbol exhibits a specific instantaneous phase trajectory. This chirp is obtained based on the raw chirp and using $\gamma_p = \frac{S_p}{B}$ which allows to perform a cyclic shift as depicted by Fig.2.1 (b) and (c). It should be noted that $S_p \in \llbracket 0, M - 1 \rrbracket$ is an integer coded on SF bits that corresponds to the transmitted symbol at time $[(p - 1)T, pT)$. The different trajectories are obtained by performing modulo T operations of a raw chirp.

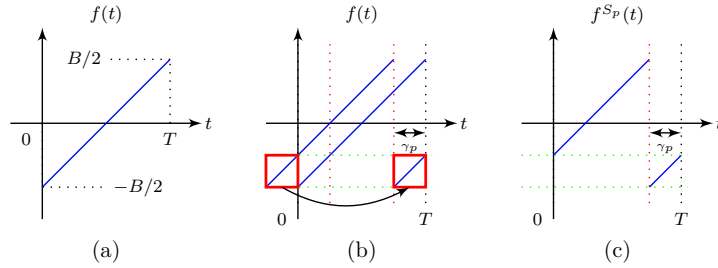


Figure 2.1: Symbol \rightarrow chirp association process - (a) up raw chirp - (b) process principle - (c) associated chirp.

The raw chirp defined for $t \in [0, T)$ is given by:

$$f^0(t) = B \left(\frac{t}{T} - \frac{1}{2} \right) \quad (2.1)$$

Then, the modulated chirp instantaneous frequency, corresponding to the k^{th} transmitted symbol S_p , can be defined as:

$$\forall t \in [0, T), f^{S_p}(t) = f^0 \left(\left(t + \frac{S_p T}{M} \right) \bmod T \right) \quad (2.2)$$

We denote $f_p(t)$ the p th transmitted chirp by LoRa-like node, uniformly distributed within the set $\{f^0(t), f^1(t), \dots, f^{M-1}(t)\}$. Each chirp $f_p(t)$ is assumed to be transmitted during the period $t \in [(p-1)T, pT)$, thereby, the complex envelope of a CSS signal $s(t)$ is a succession of random chirps such that:

$$s(t) = \sum_{p=1}^{N_s} e^{j\phi_p(t-(p-1)T)} \mathbb{1}_{[(p-1)T, pT)}(t) \quad (2.3)$$

Where N_s is the number of transmitted symbols and the chirp $f_p(t)$, corresponding to an instantaneous frequency, such that $f_p(t) = f^{S_p}(t)$, can be expressed as the derivative of the instantaneous phase $\phi_p(t)$:

$$f_p(t) = \frac{1}{2\pi} \frac{d\phi_p(t)}{dt} \quad (2.4)$$

Therefore, we obtain for $t \in [0, T - \gamma_p)$:

$$\phi_p(t) = 2\pi M \left[\left(\frac{t}{2T} \right)^2 + \left(\frac{S_p}{M} - \frac{1}{2} \right) \frac{t}{T} \right] \quad (2.5)$$

And for $t \in [T - \gamma_p, T)$:

$$\phi_p(t) = 2\pi M \left[\left(\frac{t}{2T} \right)^2 + \left(\frac{S_p}{M} - \frac{3}{2} \right) \frac{t}{T} \right] \quad (2.6)$$

with $S_p \in \{0, \dots, M-1\}$.

2.1.2 Demodulation principle

In order to explain the CSS demodulation principle, we consider a perfect time and frequency synchronizations of the received signal. According to [65, 66, 67, 68, 69], the transmitted symbols are detected by multiplying every T -long sequence of the received signal by the conjugate of a reference signal $x_{ref}(t) = e^{j\phi_p(t)}$, with $S_p = 0$ (i.e. an unmodulated chirp). It should be noted that the demodulation of the payload is done after the time and frequency synchronization using a specific preamble structure, that will be detailed latter in this chapter. Moreover, the received signal should be sampled at $T_s = \frac{1}{B}$ in the demodulation stage [67, 66]. A discrete-time version of $x_{ref}(t)$ sampled at T_s is given by:

$$x_{ref}(n) = e^{j2\pi \left(\frac{1}{2M} n^2 - \frac{1}{2} n \right)}, \quad n \in \llbracket 0, M-1 \rrbracket \quad (2.7)$$

Moreover, the discrete-time version of instantaneous phase $\phi_p(t)$ of the p^{th} transmitted symbol, sampled at T_s , can be expressed as:

$$\phi_p(n) = \begin{cases} 2\pi \left[\frac{1}{2M}n^2 + \left(\frac{S_p}{M} - \frac{1}{2}\right)n \right] & \text{for } n \in \llbracket 0, M - S_p - 1 \rrbracket \\ 2\pi \left[\frac{1}{2M}n^2 + \left(\frac{S_p}{M} - \frac{3}{2}\right)n \right] & \text{for } n \in \llbracket M - S_p, M - 1 \rrbracket \end{cases}$$

Subsequently, the discrete-version of the received signal can be expressed as:

$$y(n) = \sqrt{P}s(n) + w(n) \quad (2.8)$$

with $s(n) = \sum_{p=1}^{N_s} e^{j\phi_p(n-(p-1)M)} \mathbb{1}_{\llbracket (p-1)M, pM \rrbracket}(n)$, $w(n)$ is the complex AWGN signal with σ_w^2 its variance and P is the received signal power.

Then, considering a perfect time and frequency synchronizations, an estimation of the p^{th} transmitted symbol, can be obtained based on a M -point Fast Fourier Transform (FFT) as follows:

$$Y[k, p] = \frac{1}{\sqrt{M}} \sum_{n=0}^{M-1} \underbrace{y_p(n) \overline{x_{ref}(n)}}_{u_p(n)} e^{-j2\pi \frac{nk}{M}} \quad (2.9)$$

with $y_p(n) = y(n + pM)$, $n \in \llbracket 0, M - 1 \rrbracket$, is the complex envelope of the p^{th} transmitted chirp, $k \in \llbracket 0, M - 1 \rrbracket$ and $\overline{x(n)}$ is the complex conjugate of the function $x(n)$. Given the expressions of $y_p(n)$ and $x_{ref}(n)$, $u_p(n)$ can be written as:

$$u_p(n) = \sqrt{P}e^{j2\pi n \frac{S_p}{M}} + w(n) \overline{x_{ref}(n)} \quad (2.10)$$

Finally, in a non-coherent receiver a symbol estimate \hat{S}_p is obtained as:

$$\hat{S}_p = \underset{k \in \llbracket 0, M-1 \rrbracket}{\operatorname{argmax}} (|Y[k, p]|). \quad (2.11)$$

Whereas, in a coherent receiver a symbol estimate \hat{S}_p is obtained as:

$$\hat{S}_p = \underset{k \in \llbracket 0, M-1 \rrbracket}{\operatorname{argmax}} (\Re(Y[k, p])). \quad (2.12)$$

where, $\Re(z)$ stands for the real part of the complex number z .

In the next paragraph, we will discuss the channel coding stage deployed in LoRa PHY layer.

2.1.3 Channel coding and interleaving in LoRa

In order to increase the robustness of LoRa modulation against the AWGN and the interfering bursts, bits are encoded before the chirp generation. The encoding stages are as follows [70]:

- **Whitening**

The data transmitted in the payload may contain long sequences of either ones or zeros, introducing a DC-bias which results in the signal to have non-uniform power distribution over the transmission bandwidth [71]. Moreover, such long sequences of ones or zeros introduce data dependencies on the receiver side, before the decoder [71], since the same LoRa symbol may be received multiple consecutive times. For the above reasons, the LoRa transceiver includes a whitening and dewatering block, which perform an XOR of the information bits with a pseudo-random sequence [28, 72].

- **Forward error correction**

LoRa uses simple schemes for error detection and error correction. The forward error correction (FEC) is used for controlling errors in data transmission over unreliable or noisy communication channels. In LoRa, Hamming (k, n) FEC is used with a variable codeword size n ranging from 5 to 8 bits [71]. Furthermore, the data size per codeword k is set to 4 bits, which allow to define the coding rate as $\frac{4}{4+CR}$, with $CR \in \{1, \dots, 4\}$ is the code rate or also the number of redundancy bits. The $(4, 6)$ Hamming code is a punctured version of the standard $(4, 7)$ Hamming code, and can detect all single-bit errors as well as some double-bit errors. The standard $(4, 7)$ Hamming code can correct all single-bit errors. The $(4, 8)$ Hamming code, which is an extended version of the $(4, 7)$ Hamming code, can correct all single-bit errors, and in addition, can detect all double-bit errors or correct some double-bit errors. The $(4, 5)$ Hamming code is a parity check code and it is the default coding in LoRa nodes.

- **Interleaving**

Interleaving is a process that scrambles data bits throughout the packet. It is often combined with FEC to make the data more resilient to bursts of interference [73]. According to the patent [71], diagonal interleaver is implemented in LoRa chips. Indeed, the combination of interleaving with the FEC leads to a higher probability of correctly decoded codewords since most codewords will not contain more than a signal bit error.

- **Gray mapping**

LoRa uses a reverse Gray code for the mapping from bits to symbols. Hence, off-by-one demodulation errors only causes a single bit error, which can always be corrected by the Hamming

codes (4, 7) and (4, 8) . This property is particularly useful if the time/frequency synchronization can not be accurately fulfilled, which typically leads to off-by-one demodulation errors [67, 68, 69, 74]. Finally, the transmission and reception chains of LoRa are summarized in Fig. 2.2.

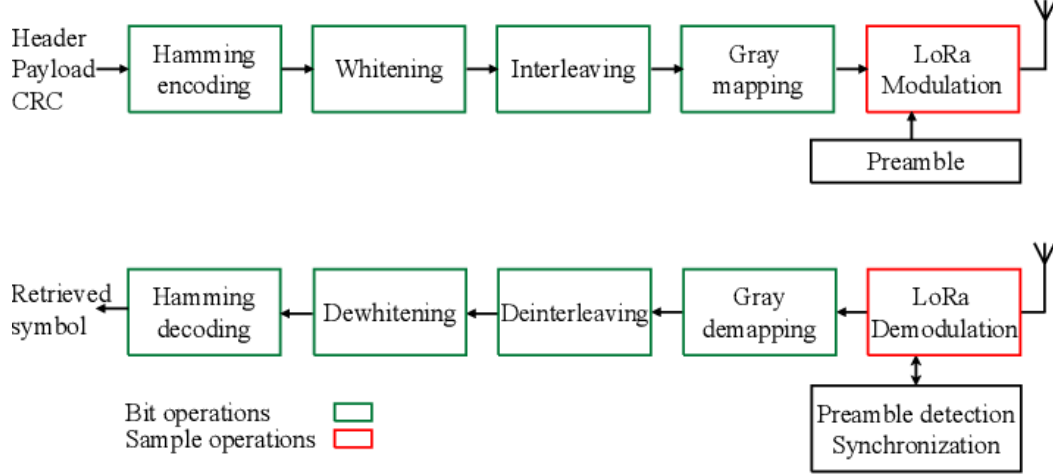


Figure 2.2: Illustration of LoRa PHY transmission and reception chains [70].

2.2 Insights on strategies used to synchronize LoRa signals

In this section, we aim to model the impact of time and frequency desynchronizations in the LoRa symbol estimation, in the context of LEO satellite communications.

2.2.1 Model of received signals

The symbol estimation of LoRa-like signals in imperfect synchronization case have been addressed by several works in the literature [66, 67, 68, 69]. In this section, our objective is to derive and analyze a closed-form expression of the signal used to estimate the symbol in the presence of:

- a time varying Doppler frequency shift, $f_d(t) = c_d t + v_d$, with c_d being the DR and v_d being the Doppler shift. Indeed, given the Doppler trajectory as presented in Fig. 1.3, we made the assumption, without loss of generality, that $f_d(t)$ is a linear function along the the packet duration. Hence, c_d and v_d are respectively in the ranges $[-DR_{max}, DR_{max}]$ and $[-v_{d_{max}}, v_{d_{max}}]$ (e.g. in Fig. 1.3, $DR_{max} = 280$ Hz/s and $v_{d_{max}} = 19$ kHz).
- an uniformly distributed sampling time offset (STO) $\Delta\tau \in [-\frac{T}{2}, \frac{T}{2}]$.

It should be noted that the static CFO Δf is equal to $v_d + v_o$, with v_o is frequency mismatch in the local oscillators (LOs) between the transmitter and the receiver. The overall CFO is equal

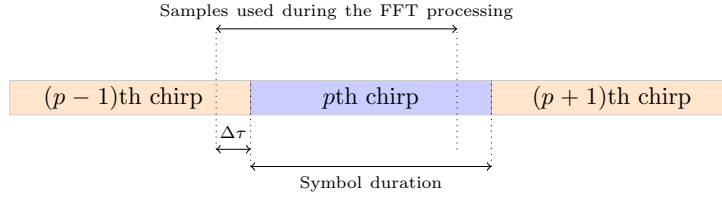


Figure 2.3: Time desynchronization illustration

to $\Delta f + c_d t$, which is composed of static and time varying offsets. However, without loss of generality, we will recall Δf as the CFO and the time-varying offset is characterized by the DR.

Based on the latter notations, the continuous-time base-band received signal is expressed as:

$$y(t) = \sqrt{P} s(t - \Delta\tau) e^{j(2\pi\nu_0 t + \varphi_0)} e^{j2\pi \int_0^t f_d(\tau) d\tau} + w(t) \quad (2.13)$$

where $s(t)$, $t \in \mathbb{R}$, is the continuous-time version of $s(n)$, P is the received signal power, φ_0 is the initial phase and $w(t)$ is the complex AWGN signal with σ_w^2 its variance. We consider here a non frequency selective channel, which make sense when LPWANs are considered and even more for LEO communications.

To correctly obtain the radio frequency signal, perform accurate time/frequency synchronization and due to the CFO, the analog to digital converter (ADC) output signal should be sampled at the frequency f'_s greater than the Nyquist rate $f_{s_{min}} = B$. However, to be compliant with the low complexity of the CSS demodulation principle [71] and to quantify the impact of imperfect synchronization on it, we consider in the following the sub-sampled signal at $T_s = \frac{1}{f_{s_{min}}}$, which gives the discrete-time version of (2.14) as:

$$y(n) = \sqrt{P} s\left(n - \frac{\Delta\tau}{T_s}\right) e^{j2\pi(\Delta f n T_s + \frac{c_d (n T_s)^2}{2})} e^{j\varphi_0} + w(n) \quad (2.14)$$

To perform our analysis, we propose to focus our attention on the decoding process of the p^{th} transmitted chirp. We notice that in the presence of a timing offset, the signal processed by the FFT at the receiver is composed of two consecutive chirps as illustrated on Fig. 2.3. Thus the signal in the p^{th} T -long sequence can be expressed, after the dechirping process, as follows:

$$\begin{aligned} z(n, p) &= y(n, p) \overline{x_{ref}(n)} \\ &= \sqrt{P} (v_{p-1}(n) + v_p(n)) + w(n) \overline{x_{ref}(n)} \end{aligned} \quad (2.15)$$

where $y(n, p) = y(n + (p - 1)M) \forall n \in \llbracket 0, M - 1 \rrbracket$. If we define $L = \lfloor \frac{\Delta\tau}{T_s} \rfloor$ as the floor value of the discrete time offset, the two signal components of $z(n, p)$ can be written as:

- a contribution of the $(p - 1)^{th}$ transmitted chirp during the time interval $\llbracket 0, L - 1 \rrbracket$,

$$\begin{aligned} v_{p-1}(n) &= s_{p-1}\left(n + M - \frac{\Delta\tau}{T_s}\right) e^{j2\pi\left(\Delta f + \frac{c_d(nT_s)}{2}\right)nT_s} \overline{x_{ref}(n)} \\ &= e^{j\theta_1} e^{j2\pi n \left(\frac{S_{p-1} - \frac{\Delta\tau}{T_s} + (\Delta f + \frac{c_d(nT_s)}{2})T}{M}\right)} \end{aligned} \quad (2.16)$$

- a contribution of the p^{th} transmitted chirp during the time interval $\llbracket L, M - 1 \rrbracket$,

$$\begin{aligned} v_p(n) &= s_p\left(n - \frac{\Delta\tau}{T_s}\right) e^{j2\pi\left(\Delta f + \frac{c_d(nT_s)}{2}\right)nT_s} \overline{x_{ref}(n)} \\ &= e^{j\theta_2} e^{j2\pi n \left(\frac{S_p - \frac{\Delta\tau}{T_s} + (\Delta f + \frac{c_d(nT_s)}{2})T}{M}\right)} \end{aligned} \quad (2.17)$$

where θ_1 and θ_2 represent two constant arguments, which will not be considered in the upcoming expressions. As shown in (2.15) and Fig. 2.3, when the timing alignment of the received signal is not performed, inter-symbol interference (ISI) occurs. In the following subsections, we analyze the impact of the CFO, the Doppler shift and the STO on the symbol estimation.

2.2.2 Impact of the CFO on symbol estimation

When the received signal is only affected by a CFO (i.e. $\{\Delta\tau, c_d\} = 0$), (2.15) becomes:

$$z(n, p) = \sqrt{P} e^{j2\pi n \left(\frac{S_p + \Delta f T}{M}\right)} + w(n) \quad (2.18)$$

Following the non-coherent symbol detection principle, as detailed in [66, 67], the p^{th} transmitted symbol is estimated by searching the frequency that maximizes the module of the FFT from M samples of $z(n, p)$:

$$\begin{aligned} Y[k, p] &= \frac{1}{\sqrt{M}} \sum_{n=0}^{M-1} z(n, p) e^{-j2\pi \frac{nk}{M}} \\ &= \sqrt{\frac{P}{M}} \Gamma_M(k, S_p + \Delta f T) + W[k] \end{aligned} \quad (2.19)$$

where $\Gamma_x(k, m) = \frac{1 - e^{j2\pi \frac{m-k}{M} x}}{1 - e^{j2\pi \frac{m-k}{M}}}$ is the discrete *sinc* function centered around frequency parameter m for a M -point FFT. However, if m is integer, $\Gamma_M(k, m)$ is referred to a *Dirac* distribution at frequency m . Given that Δf is a real random variable, $\Delta f T$ can be decomposed into two components: $\Delta f T = C + \nu$, with

- $C = \lfloor \Delta f T \rfloor$ is an integer offset that shifts the spectrum line in the frequency domain

from S_p to $((S_p + C) \bmod M)$, where $\lfloor \cdot \rfloor$ designates the rounding function,

- $\nu \in [-0.5, 0.5]$ is the fractional part of the CFO that shifts the spectrum line between two frequency bins, effectively making a *sinc* kernel appears in the frequency domain.

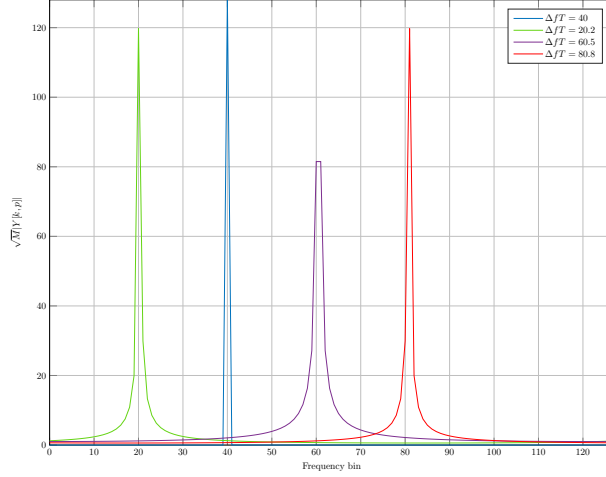


Figure 2.4: Result of $\sqrt{M}|Y[k, p]|$ when $S_p = 0$ ($SF = 7$) without AWGN for different CFO values.

We notice in Fig. 2.4 that the cardinal sine maximum is severely attenuated as long as $|\nu|$ is close to 0.5 which degrade the signal to noise ratio (SNR) of the received signal in the symbol estimation. In addition, the latter fractional offset makes the estimation of symbols very sensitive to off-by-one demodulation errors (i.e. a symbol error by ± 1). Hence, to avoid performance degradation, it is mandatory to estimate and compensate ν .

2.2.3 Impact of the DR on the symbol estimation

When only the DR is present (i.e. $\{\Delta\tau, \Delta f\} = 0$), we observe an uncompensated frequency offset that varies linearly with time at a slope c_d . For sake of simplicity and to qualitatively understand the effect of this DR, let us approximate this linear variation as constant over a symbol time and changing from symbol to symbol (i.e. $f_d(nT_s) = f_d(pMT_s)$, $\forall n \in \llbracket pM, (p+1)M - 1 \rrbracket$). Under this assumption, the frequency corresponding to the maximum amplitude of the FFT, when performed on consecutive symbols, will increase or decrease linearly (depending on the sign of c_d). Hence, (2.15) can be written as:

$$\begin{aligned} z(n, p) &= \sqrt{P} e^{j2\pi n \left(\frac{S_p + \frac{f_d(pMT_s)}{M} T}{M} \right)} + w(n) \\ &= \sqrt{P} e^{j2\pi n \left(\frac{S_p + \frac{c_d p}{M} T^2}{M} \right)} + w(n). \end{aligned} \quad (2.20)$$

Then the M -point FFT of $z(n, p)$ gives:

$$Y[k, p] = \sqrt{\frac{P}{M}} \Gamma_M(k, S_p + \frac{c_d p}{2} T^2) + W[k] \quad (2.21)$$

As depicted in (2.21), the *argmax* of the FFT is shifted from symbol to other. We notice also that the signals with highest symbol time are more sensitive to the DR.

2.2.4 Impact of the STO on the symbol estimation

In the following, we assume that only the STO occurs ($\{\Delta f, c_d\} = 0$). Since LoRa-like symbols span over M samples, a receiver that is not synchronized in time, processes windows of samples belonging to two consecutive symbols. As in the CFO, the STO is decomposed to an integer part L and a fractional offset $\lambda \in [0, 1)$, subsequently, $\frac{\Delta \tau}{T_s}$ is equal to $L + \lambda$. The first L samples in the window belong to the first symbol and the remaining $M - L$ samples originate from the second symbol. Indeed, the fractional STO can be seen as a single frequency component of frequency $\frac{\lambda}{M}$ circularly shifted by $J = M - \lfloor L + \lambda \rfloor$ samples, since a phase difference of $2\pi\lambda$ is induced at $n = J$. In this case, the de-chirped signal in the p^{th} T -long sequence $z(n, p)$ can be written as:

$$z(k, p) = \sqrt{P} (v_{p-1}(n) + v_p(n)) + w(n) \quad (2.22)$$

where

$$v_{p-1}(n) = e^{j2\pi n \frac{S_{p-1}-L}{M}} \left\langle e^{-j2\pi n \frac{\lambda}{M}} \right\rangle_{J-M} \mathbb{1}_{\llbracket 0, L-1 \rrbracket}(n), \quad (2.23)$$

$$v_p(n) = e^{j2\pi n \frac{S_p-L}{M}} \left\langle e^{-j2\pi n \frac{\lambda}{M}} \right\rangle_J \mathbb{1}_{\llbracket L, M-1 \rrbracket}(n), \quad (2.24)$$

are respectively the contributions of the $(p-1)^{\text{th}}$ and the p^{th} chirps, with $\langle x(n) \rangle_J$ corresponds to a circular shift of J samples on the signal $x(n)$. Hence, as shown with (2.25), when the time alignment of the received signal is not perfectly performed, ISI occurs. Furthermore, the desired maximum value of the periodogram is shifted and attenuated, which leads to a biased estimated symbol and a loss of SNR. Indeed, Computing the M -point FFT of (2.22) yields the following signal:

$$Y[k, p] = \sqrt{\frac{P}{M}} (V_{p-1}[k] + V_p[k]) + W[k] \quad (2.25)$$

Where

$$V_{p-1}[k] = e^{-j2\pi \frac{kJ}{M}} \Gamma_L(k, S_{p-1} - (L + \lambda)) \quad (2.26)$$

$$V_p[k] = e^{-j2\pi\frac{kJ}{M}} \Gamma_{M-L}(k, S_p - (L + \lambda)) \quad (2.27)$$

are respectively the FFTs of the parts of $(p - 1)^{th}$ and p^{th} chirps.

To sum up, equations (2.18), (2.23) and (2.24) reveal that the fractional CFO ν and the fractional STO λ cannot be considered equivalent. Notably, the CFO adds to the de-chirped signal a residual frequency term continuous across the up chirps boundaries, whereas the fractional STO induces a frequency term whose phase is reset to $2\pi\lambda$ after crossing an upchirp boundary.

After giving an overview on the impact of time and frequency offsets on the LoRa symbols demodulation, we detail in the next paragraph the synchronization algorithms proposed in the literature.

2.3 State of the art on synchronization algorithms with LoRa signals

In this subsection, we recall the main principles of the synchronization methods commonly used in LoRa [66, 67, 75, 58, 76, 69, 68, 74]. To note that the models of the received signal are as expressed in (2.14) with $c_d = 0$ since the latter works did not deal with the Doppler-time variation. Moreover, we will not discuss the packet detection in the upcoming algorithms. For this purpose, several methods will be presented in the next sections and in the next chapter when dealing with interference.

To understand the synchronization process of LoRa signal, which leads to the latter constraint of maximum CFO estimable, it is mandatory to give a brief overview on the structure of the specific LoRa preamble used in this purpose.

2.3.1 Structure of the synchronization signal

The signal transmitted by LoRa node starts with a preamble composed of N_p raw chirps (up or down chirps) which are exploited to detect the presence of a LoRa packet and to perform the time and frequency synchronization. $N_{sw} = 2$ special modulated symbols known as synchronization word “sync word” are used to verify the accurate synchronization of the received frames¹. The synchronization sequence ends by $N_{SFD} = 2.25$ unmodulated chirps known as the start of frame delimiter (SFD), which help for the time and frequency synchronizations [66]. To conquer this challenge, the chirps of the SFD must be the complex conjugate of ones in the preamble. A spectrogram representing a LoRa frame, obtained by recording real LoRa data

¹It is used also as a network identifier.

transmitted by a chip SX1276, is represented in Fig. 2.5.

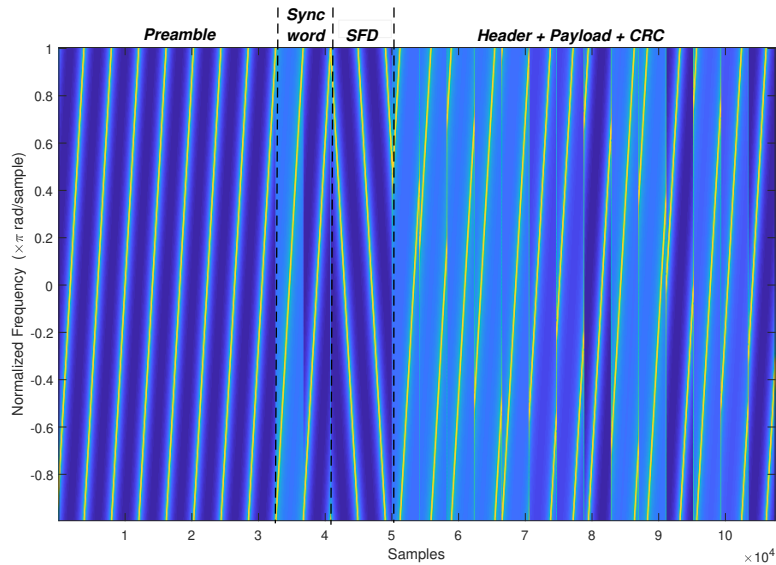


Figure 2.5: Spectrogram of the LoRa frame obtained by recording real LoRa data, using raw up chirps in the preamble

2.3.2 Time and frequency synchronization algorithms

In this subsection, we provide an overview on several methods of the literature, allowing to estimate the integer and fractional parts of the CFO and STO. Then, we discuss the overall synchronization algorithms as presented in latter works. Subsequently, every synchronization algorithm in LoRa mainly implements the following steps:

- Packet detection using the preamble
- Estimating the fractional CFO, then compensate its contribution,
- Estimating the fractional STO, then compensate its contribution,
- jointly estimation of the integer parts of the CFO and the STO, followed by their compensation.

As already mentioned, the preamble detection algorithm will not be detailed in this section. Hence, we start directly by the estimation of the fractional CFO ν . It worth noting before starting the explications of the aforementioned steps that in the preamble only one cardinal sine is obtained after the FFT processing, even in a non-synchronized mode, since all its symbols are equal to zero. Moreover, based on the previous section, the frequency estimated in all the

up chirps of the preamble is equal to:

$$\hat{S}_{up} = (-L - \lambda + C + \nu) \pmod{M}$$

2.3.2.1 Fractional CFO estimation

After the packet detection, the first step of the most of the existent synchronization algorithms in the literature is the estimation and the compensation of the fractional CFO [66, 67, 69, 74]. The former induces a linear phase term that is continuous across symbols, whereas the phase due to the latter is cyclic with period M . This cyclic property allows a receiver to estimate ν independently of λ . Furthermore, the compensation of the fractional offsets is mandatory to avoid off-by-one demodulation errors and the degradation of the SNR after the dechirping process. Thereafter, ν and λ should be compensated before the estimation of the integer offsets C and L . As an example, ν can be estimated via the following two methods:

- **Schmidl-Cox estimator [68, 69]**

One method to estimate ν was described in [68, 69] using variant of the well-known Schmidl-Cox estimator [77]. This estimator averages the phase differences between samples with the same index from two consecutive chirps carrying the same symbol. Given that the transmitted signal starts with N_c unmodulated up chirps of the preamble, an estimate $\hat{\nu}$ of ν is obtained as follows:

$$\hat{\nu} = \frac{1}{N_c - 1} \sum_{p=0}^{N_c-2} \frac{1}{2\pi} \arg \left(\sum_{n=0}^{M-1} y(n, p) \overline{y(n, p+1)} \right) \quad (2.28)$$

with N_c is the number of up chirps used to compute $\hat{\nu}$.

- **Method in [66, 67]**

As an alternative of Schmidl-Cox estimator, the extraction of the fractional CFO ν can be achieved simply during the reception of two consecutive identical symbols, e.g. two up-chirps or two down-chirps. Therefore, if the phase, respectively ϕ_1 and ϕ_2 , of the signal present in this FFT bin is extracted for these two consecutive identical symbols, we can write:

$$\phi_2 - \phi_1 = \frac{\nu}{B}(k + M) - \frac{\nu}{B}(k) \quad (2.29)$$

from which we find $\hat{\nu} = \frac{B(\phi_2 - \phi_1)}{M}$.

The accuracy of the latter estimator could be enhance by averaging the value of $\hat{\nu}$ over several up chirps of the preamble.

2.3.2.2 Fractional STO estimation

To achieve accurate receiver alignment, it is necessary to compensate the fractional STO λ . Indeed, once the fractional CFO is estimated, the latter is compensated in the unmodulated up chirps of the preamble to allow the receiver performing the estimation of λ . To note here that residual error in the estimation of ν will impact the estimation process of λ . It worth noting also that the impact of the fractional STO λ produces a frequency offset after the FFT processing as depicted in (2.26) and (2.27).

Many estimators in the literature have been designed to estimate a fractional frequency ϵ of a sinc signal $\Gamma(k, \epsilon)$ under an AWGN channel [78, 79, 80].

- **Method in [69]**

As we have already mentioned, due to the term $e^{j2\pi\frac{kJ}{M}}$, the expression of the signal $Y[k, p]$, $p \in [1, N_p]$, after correction of ν is not a strict cardinal *sinc* function. Hence, estimating λ from usual estimators therefore requires *a priori* knowledge of $J = M - [L + \lambda]$, which is unknown until the reception of a down chirp. Hence, as demonstrated in [68, 69], an estimate $\hat{\lambda}_p$ of λ , in the p^{th} unmodulated chirp of the preamble, can be expressed as:

$$\hat{\lambda}_p = \frac{e^{-j2\pi\frac{j}{M}}Y_\nu[(i+1) \bmod M, p] - e^{-j2\pi\frac{j}{M}}Y_\nu[(i-1) \bmod M, p]}{2Y_\nu[i, p] - e^{-j2\pi\frac{j}{M}}Y_\nu[(i+1) \bmod M, p] - e^{-j2\pi\frac{j}{M}}Y_\nu[(i-1) \bmod M, p]} \quad (2.30)$$

with

$$Y_\nu[k, p] = \frac{1}{\sqrt{M}} \sum_{n=0}^{M-1} \left(y(n, p) \overline{x_{ref}(n)} e^{-j2\pi\frac{nv}{M}} \right) e^{-j2\pi\frac{nk}{M}} \quad (2.31)$$

being the FFT in the p^{th} T -long sequence of the preamble after the compensation of $\hat{\nu}$ and $i = \underset{k \in [0, M-1]}{\operatorname{argmax}} (|Y[k, p]|)$.

To be noted also that the compensation of the fractional offsets should be implemented before the estimation of the integer parts L and C to avoid off-by-one errors. Therefore, authors in [69] propose to estimate the fractional STO in two steps. The first one is to perform a coarse estimation using (2.30) and by averaging the values of $\{Y_\nu[i-1, p], Y_\nu[i, p], Y_\nu[i+1, p]\}$ over the first $\frac{N_p}{2}$ up chirps of the preamble to improve the accuracy of the estimation. In this first step, they considered $M - \hat{S}_{up}$ as an approximation of \hat{J} instead of $M - \hat{L}$. If a perfect compensation of ν is assumed we obtain: $\hat{S}_{up} = (-L - \lambda + C) \bmod M$. This coarse estimation allows not to wait for the SFD symbols in order to jointly estimate \hat{L} and \hat{C} as we will explain in the next paragraph. After that the former coarse estimate of λ is compensated in order to compute \hat{L} and \hat{C} .

Finally, a fine estimation of the fractional STO is performed by approximating \hat{J} with $M - \hat{L}$ and by using the last $\frac{N_p}{2}$ unmodulated chirps of the preamble for this purpose.

- **Method in [67, 66]** This method allows to compute the fractional STO λ without the estimation of \hat{J} and thus without having to wait for the down chirps of the SFD. This method leverages the following intermediate function:

$$TE_{raw}(\lambda) = \frac{|\Gamma_M(1, \lambda)| - |\Gamma_M(-1, \lambda)|}{|\Gamma_M(0, \lambda)|} \quad (2.32)$$

Hence, after the compensation of the fractional CFO ν , the estimate $\hat{\lambda}$ is computed by inverting $TE_{raw}(\lambda)$ as follows:

$$\hat{\lambda} = TE_{raw}^{-1} \left(\frac{|Y_\nu[(i+1) \bmod M, p]| - |Y_\nu[(i-1) \bmod M, p]|}{|Y_\nu[i, p]|} \right) \quad (2.33)$$

with $i = \underset{k \in \llbracket 0, M-1 \rrbracket}{\operatorname{argmax}} (|Y_\nu[k, p]|)$.

As in the latter method, averaging the magnitude of $Y_\nu[k, p]$ over several up chirps would enhance the accuracy of the estimator. However this averaging process is not mentioned in [67, 66]. This estimator presents a very high variance due to the derivative of $TE_{raw}^{-1}(x)$ being close to 0 for small values of λ [67].

After computing the estimate $\hat{\lambda}$, a fine timing alignment is done just before the α sub-sampling in the decimation chain of the receivers digital front-end (i.e. process samples produced at the frequency rate $f'_s = \alpha f_{s_{min}}$). Indeed, the fractional STO equals to $\lfloor \alpha \times \hat{\lambda} \rfloor$ can be easily compensated by shifting the decimation operators input by a corresponding number of undecimated samples. The signal after the correction of the fractional STO and the sub-sampling at the Nyquist rate can be written as follows:

$$y_\lambda(n) = \left(y((n + \lfloor \alpha \times \hat{\lambda} \rfloor) T'_s) \right)_{nT_s} \quad (2.34)$$

2.3.2.3 Integer CFO and integer STO estimation process

Given the specific structure of the synchronization signal as presented in previous paragraph, an estimation of the integer parts of the STO and the CFO (L and C respectively) can be jointly performed. As explained in [66, 67, 68, 69, 76, 74], a system of two equations using the estimated argmax of each FFT module in the preamble and the SFD are used to that end. If we denote the latter estimated frequencies \hat{S}_{up} and \hat{S}_{down} respectively and by considering a perfect

compensation of ν and λ , we obtain:

$$\begin{aligned}\hat{S}_{up} &= (-L + C) \pmod{M} \\ \hat{S}_{down} &= (L + C) \pmod{M}\end{aligned}\tag{2.35}$$

Combining the two equations of (2.35), \hat{C} the estimate of C can be easily determined as :

$$\hat{C} = \frac{1}{2}\Lambda_M \left[(\hat{S}_{up} + \hat{S}_{down}) \pmod{M} \right]\tag{2.36}$$

where

$$\Lambda_M(k) = \begin{cases} k & \text{for } 0 \leq k < \frac{M}{2}, \\ k - M & \text{for } \frac{M}{2} \leq k < M. \end{cases}$$

Once \hat{C} is known, \hat{L} can be computed using:

$$\hat{L} = (S_{up} - \hat{C}) \pmod{M}\tag{2.37}$$

If we note $r(n)$ the coarse time-frequency synchronized signal after estimating the integer parts of the CFO and STO, \hat{C} and \hat{L} , we have:

$$r(n) = y_\lambda(n + \hat{L})e^{-j2\pi n \frac{(\hat{C} + \nu)}{M}}\tag{2.38}$$

Given the expression of \hat{C} as in (2.36), the former can only be defined modulo $\frac{M}{2}$. Knowing that C is equal to $\lfloor \Delta f T \rfloor$, Δf should be modulo $\frac{B}{2}$ to perform accurate time and frequency synchronizations. As a result, the receiver will be able to recover a CFO only in the range $[-\frac{B}{4}, \frac{B}{4}]$.

After the compensation of all the offsets C , L , ν and λ , each T -long sequence of the payload is sub-sampled at the frequency rate $f_{s_{min}}$. Thus, the symbols can be easily estimated as presented in (2.12).

2.3.3 Limits of the synchronization algorithms

As we have already explained, the algorithms used to synchronize LoRa-like signals lead to a maximum CFO estimable of $\frac{B}{4}$, if we perform the estimation of latter offset at the Nyquist rate. The former constraint is caused by the jointly estimation of the integer CFO and the integer STO obtained by a system of two equations as depicted in (2.35). For instance, it must be recognized that the aforementioned synchronization methods developed in [66, 67, 68, 69, 74] are very clever and offers an excellent compromise performance and implementation complex-

ity. However, the low computational complexity of the synchronization proposed by the latter works leads to the former constraint of maximum CFO estimable. Indeed, this maximum value is confirmed by the Semtech technical note for the LoRa SX1272 chipset [81]. This study shows that on average ($\forall SF$) in the 868 MHz band and $B = 125$ kHz, the LoRa chipset is robust to synchronization errors of ± 35 ppm ($\simeq \pm \frac{B}{4}$). This means that the frequency synchronization algorithm implemented in the chipset works in this range. An example from [81] is given in Fig. 2.6.

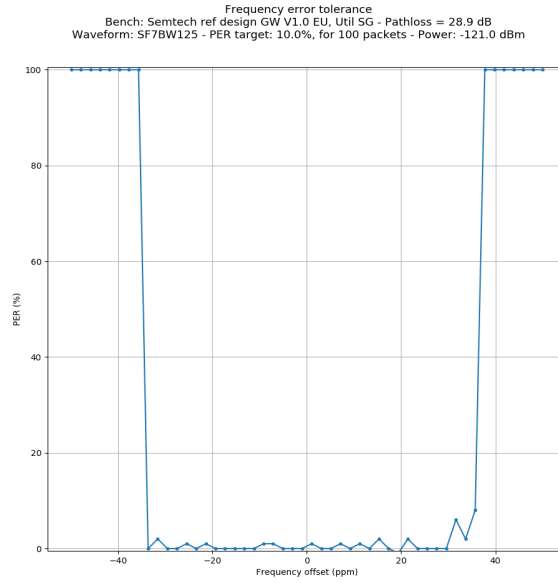


Figure 2.6: Rx Frequency error Tolerance for $SF=7$, a bandwidth of 125kHz, 25°C

Although this limit of maximum CFO estimable does not really be a problem regard to: 1/the bandwidth, 2/the carrier frequency and 3/the local oscillator precision, it prevents in the current state to reduce the bandwidth of the transmitted signals. However, the reduction of the bandwidth makes it possible to increase the sensitivity of the receiver. Some applications, such as LEO satellite communications, lend themselves well to this need for range expansion. The contribution developed in the following section is not limited to this application case but is particularly well adapted to it. Thereby, we propose in the next section a new LoRa-like waveform resilient to the CFO and much more robust than CSS against any time-varying offset, typically the DR. The decoding performance of the former waveform will be evaluated in perfect synchronization case over an AWGN channel and in the presence of synchronization errors. Moreover, we will prove that the association between the former waveform and an original synchronization algorithm will lead to bypass the constraint of the maximum CFO that could be estimated. This waveform is also much more robust to Doppler time-variation than the CSS modulation, which makes our proposed receivers in the next sections good candidates for

communication with LEO satellites.

2.4 Differential Chirp Spread Spectrum

In the previous section, we showed that jointly estimating the CFO and the STO leads to maximum CFO estimable of $\frac{B}{4}$. To alleviate this constraint, we propose a modification of the LoRa PHY layer which we refer to as differential CSS (DCSS). In addition, introducing the well-known differential process to the CSS modulation allows to demodulate the received signals without performing a complete frequency synchronization. Furthermore, we will prove by simulations that the proposed modulation is much more robust to Doppler time variation than CSS. To note that from this section to the end of the manuscript, we will provide all the contributions of works performed during this PhD thesis.

2.4.1 Modulation

Based on the previous analysis, we propose an enhancement of the LoRa symbol generation process and we then show how it makes the detection of the received symbols robust to synchronization errors. Our idea, inspired by the principle of differential digital modulation techniques, consists in transmitting not directly the value of the symbols but rather their cumulative sum so that, at the receiver, they can be retrieved by differentiation. In the following, we call this method of digital modulation: Differential Chirp Spread Spectrum (DCSS). Based on this, the DCSS transmitter consists in sequentially generating chirps based on the symbols D_p obtained as follows:

$$D_p = (S_p + D_{p-1}) \mod M \text{ for } p \geq 1 \quad (2.39)$$

where S_p has been defined as the LoRa symbol transmitted at time pT . Without loss of generality, we suggest to set $D_0 = 0$ to initiate the integration processing.

2.4.2 Demodulation

At the receiver side, the estimation of $\{\hat{S}_p\}_{p \geq 1}$ is obtained as:

$$\hat{S}_p = (\hat{D}_p - \hat{D}_{p-1}) \mod M \text{ for } p \geq 1 \quad (2.40)$$

where the estimation of the DCSS symbols $\{\hat{D}_p\}$ are based on the periodogram method presented in the previous chapter. Given the model of the received signal as defined in (2.14) in the

presence of the STO, the CFO and the DR, the p^{th} transmitted DCSS symbol is estimated as:

$$\begin{aligned}\hat{D}_p &= D_p - \frac{\Delta\tau}{T_s} + (\Delta f + c_d \cdot nT_s)T \\ &= D_p - (L + \lambda) + (C + \nu + \frac{c_d}{2} \cdot nT)T\end{aligned}\tag{2.41}$$

Thus, as expressed in (2.16) and (2.17), the differential process performed by (2.40), limits the impact of $-\frac{\Delta\tau}{T_s} + (\Delta f + c_d \cdot nT_s)T_s$ on the symbol estimations. However, it is necessary to estimate and compensate the fractional CFO ν and the fractional STO λ to prevent performance degradation due to off-by-one demodulation errors. It is also necessary to estimate the integer STO to avoid the impact of ISI. In addition, we will see in upcoming simulations that deploying DCSS waveform allow to tolerate some time synchronization errors.

Furthermore, to insure high robustness of DCSS to the variation of Doppler shift over time, the latter technique is combined with more precise estimation of the frequencies that maximize the module of the FFTs as described in the next paragraph. It worth noting that if the received signal is only affected by the CFO, the demodulation of the payload can be performed after only the compensation of the fractional CFO ν .

2.4.3 Fine estimation of the symbols

In the presence of time varying Doppler shift, it is judicious to implement more precise estimation of the *argmax* of each FFT module. To conquer this challenge, many techniques have been developed in the literature. For instance:

- Quadratic interpolation,
- Secant method,
- Newtons method,
- Bisection method,
- etc.

For more details on the latter methods, the reader can refer to [82].

In our work, we decided to use a low-complexity technique based on the Bisection method. Thus, if we consider the interval $[a = \omega_{\hat{D}_{p-1}}, b = \omega_{\hat{D}_{p+1}}]$, with $\omega_{\hat{D}_p} = \frac{2\pi(\hat{D}_p-1)}{M}$ being the pulse that matches the symbol \hat{D}_p , we have to maximize the following function:

$$R(\omega) = \left| \sum_{n=0}^{M-1} z(n, p) e^{-j(n-1)\omega} \right|, \omega \in [a, b]\tag{2.42}$$

With $z(n, p)$ is defined as in (2.18) given that the estimated symbol is \hat{D}_p . We propose to numerically compute an approximation of \hat{D}_p with an error less than a given maximum permissible error ζ .

A trivial solution is to consider N equidistant points $l_1 = a < l_2 < \dots < l_N = b$ with $N > \frac{b-a}{\zeta}$, to calculate $R(l_1), R(l_2), \dots, R(l_N)$ and to find the index of the maximum of this sequence. This method requires the calculation of $R(\omega)$ over N points. Therefore, it has a complexity in the order of $O(M) = O(\frac{b-a}{\zeta})$.

However, taking into account the concave nature of $R(\omega)$, the number of points at which the calculation of $R(\omega)$ is performed can be significantly reduced by performing a binary search. The proposed algorithm is as follows:

1. Consider a number of points that is a power of two. More precisely, $p = \log_2(\frac{b-a}{\zeta}) + 1$ and $N = 2^p$ are taken. The starting analysis interval is $[a, b] = [l_1, l_{2^p}]$.
2. Estimate $R(\omega)$ at the extremities $l_1 = a$ and $l_{2^p} = b$, and also at the two points in the "middle" of the analysis interval i.e $l_{2^{p-1}}$ and $l_{2^{p-1}+1}$. If the maximum of $R(\omega)$ calculated in these four points is reached for one of the two extremities of half" left $[l_1, l_{2^{p-1}}]$, this interval becomes the new analysis interval otherwise the new analysis interval will be the half" right $[l_{2^{p-1}+1}, l_{2^p}]$.
3. Loop on step 2 by processing the new analysis interval and continue until step 4 criteria is reached.
4. After p iterations, the extremities of the analysis interval are two points at a distance of $\frac{b-a}{2^p}$. The highest value of $R(\omega)$ computed from these points is decided to be the sought solution.

The association between the DCSS technique and the latter interpolation method would allow the proposed receiver to have high robustness against time-varying CFO at the price of a moderate increase in the complexity.

2.4.4 DCSS Performance evaluation and comparison with CSS

In this section, we aim to evaluate the performance of the DCSS modulation against synchronization errors especially the Doppler time-variation along the packet duration. We provide, as well, a comparison between DCSS and CSS to assess the robustness of these two technologies in several desynchronization scenarios.

In the following, we consider in all the simulations an oversampling factor $\alpha = 8$ and a reference bandwidth $B_{ref} = 125$ kHz, which is the most commonly used bandwidth in LoRa-

based networks. We represent the results of Monte-Carlo based simulations, which are obtained from a DCSS and CSS signals simulator that we developed in MATLAB.

2.4.4.1 Perfect synchronization case

In this paragraph, we evaluate the decoding performance of DCSS in a perfect synchronization case and compared with CSS in the same conditions. Hence, the received signal, sampled at the Nyquist rate, can be written as:

$$y_s(n) = \sqrt{P}s(n) + w(n) \quad (2.43)$$

Where $s(n)$ is defined as in (2.8) with the transmitted symbols are $\{D_p\}_{p \geq 1}$ for DCSS and $\{S_p\}_{p \geq 1}$ for CSS.

Given the principle of DCSS as described in section 2.4, one can remark that this modulation naturally introduces a degradation of performance compared to CSS. Indeed, two consecutive DCSS symbols must be properly detected for the original symbol carrying the information to be accurately retrieved (see (2.40)). However, Fig. 2.7, which represents the BER of CSS and DCSS in perfect synchronization as function of the SNR, proves that this impairment remains low. For instance, for a BER equals to 10^{-4} , the loss is only of 0.2 dB for all the SFs .

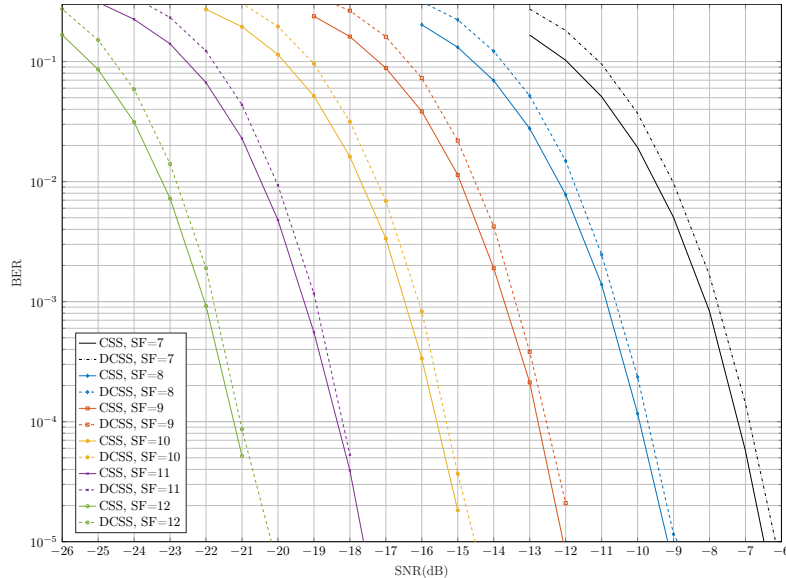


Figure 2.7: Comparison of bit error probabilities of LoRa and DCSS technologies before channel decoding.

2.4.4.2 Robustness against the CFO and STO

The second simulation test aims in evaluating the robustness of DCSS to time and static frequency offsets. Hence the received signal can be written as in (2.14), with the DR c_d is equal to zero. Subsequently, We represent in Fig. 2.8 the BER of DCSS as a function of the SNR with different CFO and STO values. Here, we consider a CFO Δf uniformly distributed in $[-B, B]$ and a STO $\Delta\tau$ uniformly distributed in $[-\Delta\tau_{max}, \Delta\tau_{max}]$. It should be noted here that the fractional offsets ν and λ are supposed equal to zero to avoid off-by-one demodulation errors. Thus, in this case the fine estimation of the symbols is not needed.

Without the time synchronization, it can be seen that a loss of SNR of only 2.7 dB is obtained at a BER = 10^{-4} when $\Delta\tau_{max} = 25\%T$, which proves the natural robustness of DCSS to large STO values. In addition, this simulation proves that DCSS is insensitive to CFO since the curve of perfect synchronization fits with the one of the perfect time alignment with the presence of huge CFO.

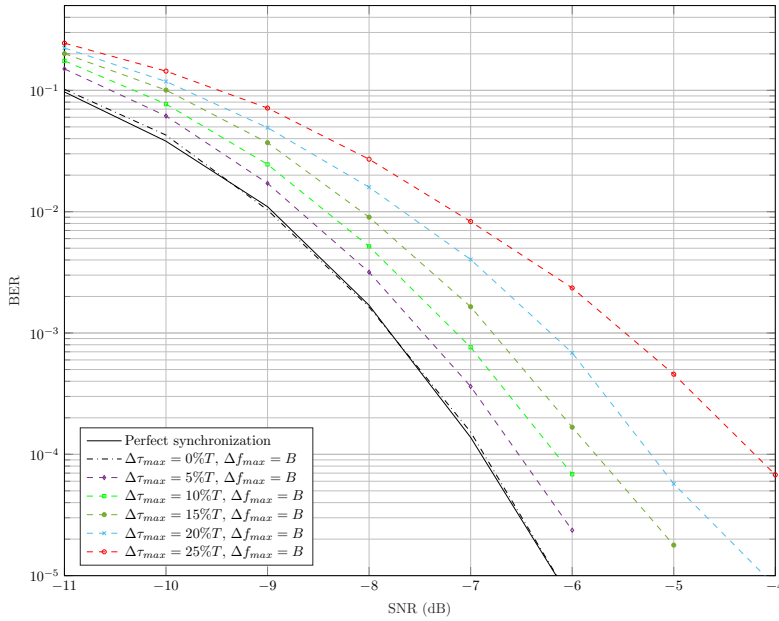


Figure 2.8: Impact of synchronization errors on the BER of DCSS with $SF = 7$.

2.4.4.3 Robustness against Doppler time-variation

In this paragraph, we aim to evaluate the robustness of DCSS against the DR. Thus, we consider the signal after the dechirping operation as defined in (2.20). Given the differentiation process of DCSS and the use of the interpolation to estimate more accurately the $argmax$ of each FFT, our proposed technique is supposed to be robust to much faster Doppler variation than LoRa signals. This result is confirmed in Fig. 2.9 by presenting the packet error rate (PER) evolution of DCSS and CSS signals as function of the DR c_d in a perfect synchronization case (i.e. $\Delta\tau, \Delta f = 0$).

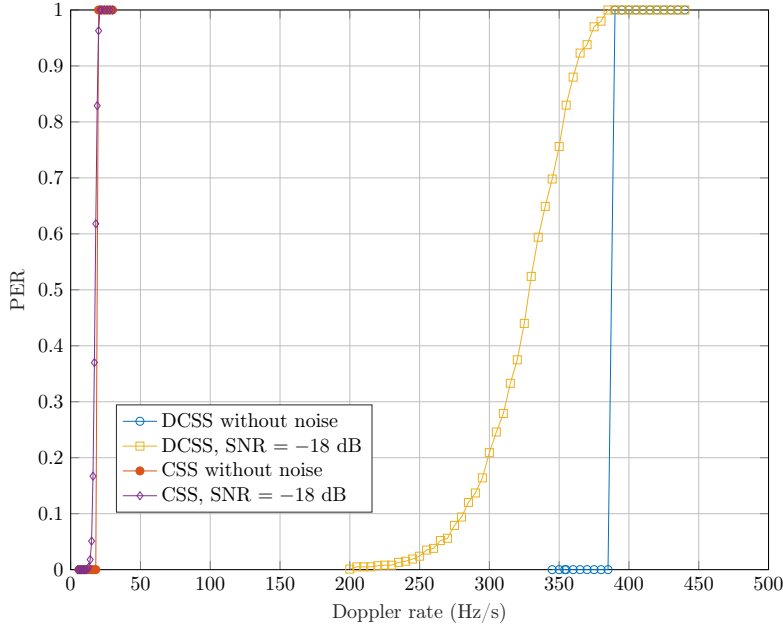


Figure 2.9: Robustness of DCSS against Doppler rate with $SF = 12$, $B = B_{ref}$ and $N_{pay} = 51$ bytes.

It can be seen in this figure that, without considering the channel noise, the DR limit that can be naturally supported by DCSS, with $SF = 12$ and a payload size $N_{pay} = 51$ bytes², is $c_d^{th} = 385$ Hz/s. Whereas for CSS the DR limit can not exceed 18 Hz/s. In the presence of the AWGN signal and for a signal to noise ratio (SNR) of -18 dB³ the robustness of both techniques is degraded but DCSS still maintain good performance with DR lower than 250 Hz/s, when LEO communications is considered. This value corresponds to the DR order of magnitude, indeed, according to [83], the maximum value of the DR for a typical altitude of 650 km is 245 Hz/s (at sub-GHz carrier frequency).

Finally, we represent in Fig. 2.10 the PER evolution of DCSS and CSS for $SF = 12$, $B = B_{ref}$ and a payload size $N_{pay} = 51$ bytes, for different DR values, in an AWGN channel model. The results confirm the fact that DCSS is much more robust to DR than CSS. For instance, it can be easily seen that, for CSS signals, the PER is greater than 0.5 for all SNR values, if the DR is equal or greater than 12 Hz/s. Whereas, for DCSS signals, a PER equal to 10^{-3} (resp. 10^{-2}) is achieved at SNR= -18 dB for DR= 200 Hz/s (resp. DR= 240 Hz/s).

As depicted in the latter results, DCSS modulation is much more robust to DR than CSS thanks to the differential processing and the fine estimation of the symbols. In addition, the latter differential process makes the DCSS waveform resilient to the CFO. Hence, it is possible to bypass the constraint of the maximum CFO estimable at f_{smin} by performing the time syn-

²According to LoRaWan protocol, the maximum payload size for the slowest data rates, $SF \in \{10, 11, 12\}$ on 125 kHz is 51 bytes.

³The SNR sensitivity threshold of LoRa with $SF = 12$ is -20 dB.

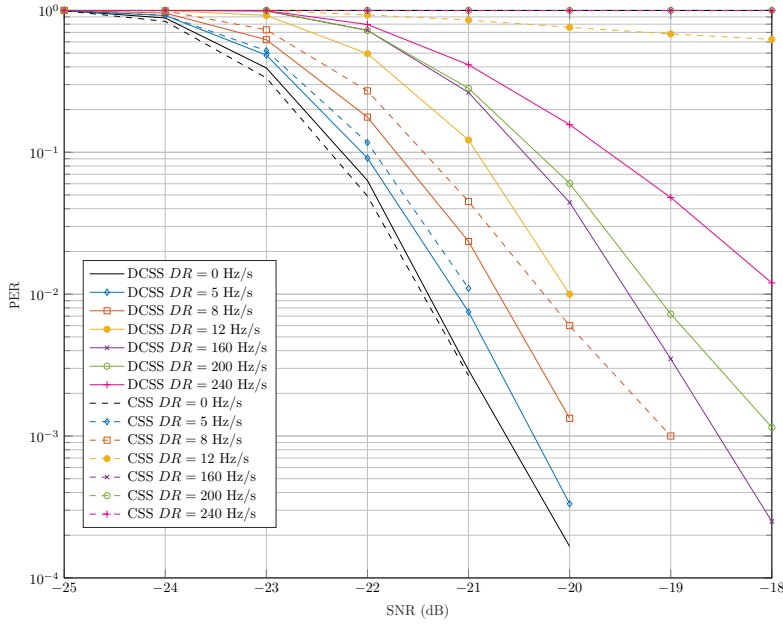


Figure 2.10: Comparison of robustness of CSS and DCSS technologies to DR over AWGN channel with $SF = 12$, $B = B_{ref}$ and $N_{pay} = 51$ bytes.

chronization regardless to the CFO. This finding encourages us to propose two synchronizations algorithms associated to the DCSS modulation, as will be presented in the next two sections.

2.5 Proposed DCSS Transceiver using chirped preamble

In this section, we propose a receiver based on the DCSS modulation and a novel synchronization algorithm. This algorithm allows to perform the timing synchronization regardless to the CFO, which makes it possible to bypass the constraint of the maximum CFO estimable. Moreover, as already proved, the lowest data rates in LoRa, which have link budgets allowing to communicate with LEO satellites, are very sensitive to DR. However, thanks to the differential process associated with the fine estimation of the symbols, the proposed receiver will have better robustness to DR and will allow the LoRa-like transmission with latter data rates to establish reliable communication with LEO satellites.

2.5.1 Proposed synchronization signal

The DCSS transmitter is basically similar to the LoRa one since the same structure of linear chirps is used. However, additional differential processing is implemented before the chirps are generated. This can be easily implemented, which guarantees the cost-effectiveness of our proposed transmitter. Another distinction of this latter transmitter is the structure of the preamble which is used for the detection and synchronization of the received signals.

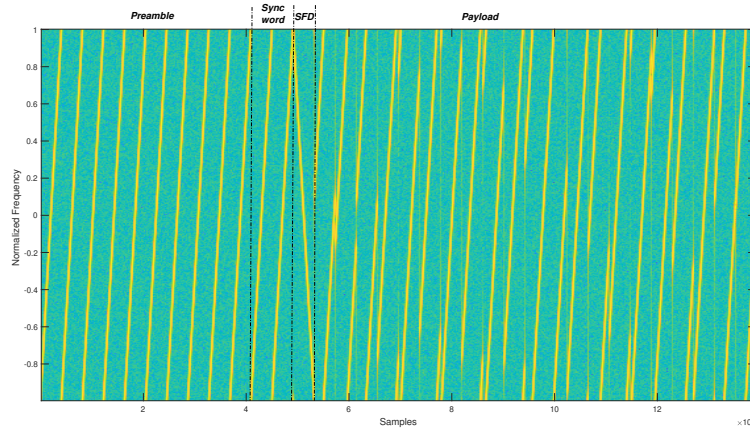


Figure 2.11: Spectrogram of the transmitted signal.

Indeed, in our DCSS transmitter, the preamble and the SFD symbols are no longer needed to estimate L and C , using the system of two equations as in (2.35), since the latter modulation is robust to frequency desynchronization and tolerates some timing misalignment that do not induce important ISI. Therefore, in this work we propose an original method to estimate time offset regardless the frequency offset. To this end, we use the N_p up chirps of the preamble for the signal detection and the estimation of the fractional offsets. We maintain also the *sync word* to verify the accuracy of the time synchronization and one down chirp symbol as a SFD to adjust the receivers timing alignment. This structure of preamble is very similar to the ones deployed in LoRa PHY layer except for the number of symbols of the SFD, which is reduced to one symbol.

If we note $x_{pre}(t)$ the complex envelope of the proposed synchronization signal and $s(t)$ the continuous-time version of (2.3) where the transmitted symbols are $\{D_p\}_{p \geq 0}$, the signal transmitted by a DCSS node can be written as follows:

$$x(t) = x_{pre}(t)\mathbb{1}_{[0, T_p]}(t) + s(t - T_p)\mathbb{1}_{[T_p, T_p + N_s \times T)}(t) \quad (2.44)$$

where T_p is the duration of the latter synchronization sequence which is equal to $(N_p + N_{sw} + 1)T$. A spectrogram example of the transmitted signal is shown on Fig. 2.11.

2.5.2 Proposed synchronization algorithm

To implement our synchronization algorithm, we consider the same model of the received signal as in (2.14). To be more general compare to (2.14), the global time desynchronization parameter is supposed to be $t_s = KT + \Delta\tau$, with $K \in \mathbb{N}$ and $\Delta\tau$ is the same as the one used in (2.14).

Thus, the continuous version of the received signal is written:

$$y(t) = \sqrt{P}x(t - t_s)e^{j(2\pi(\Delta f + \frac{c_d \cdot t}{2})t + \varphi_0)} + w(t) \quad (2.45)$$

As we have already mentioned, due to the CFO and the DR, the ADC output signal should be sampled with $f'_s = \alpha f_{s_{min}}$, which will allow also more accurate receiver's time alignment with the effective start of the payload and is necessary to correctly capture the power spectral density of the signal to process. Nevertheless, to ensure a low complexity of our proposed receiver and for a fair comparison with LoRa receivers, the different processing steps are developed with a sampling rate such that $T_s = \frac{1}{f_{s_{min}}}$. Yet, it worth noting that to compensate the fractional offset λ , it is mandatory to use the over-sampled signal in order to re-align the receiver with $\lfloor \alpha \times \lambda \rfloor$ samples. Hence, the received signal sampled at T_s can be written as:

$$y(n) = \sqrt{P}x(n - n_s)e^{j(2\pi(\Delta f + \frac{c_d \cdot n T_s}{2})n T_s + \varphi_0)} + w(n) \quad (2.46)$$

where

$$n_s = \lfloor \frac{t_s}{T_s} \rfloor = KM + \lfloor \frac{\Delta \tau}{T_s} \rfloor \quad (2.47)$$

DCSS as well as all the other modulation techniques does not escape the need of an accurate time synchronization to avoid ISI which strongly degrades the receiver sensitivity. However, as detailed in 2.4, the differential process allows tolerating some time misalignment. In addition, after the time alignment, this differential process makes DCSS insensitive to the integer CFO during the payload demodulation and enhance the robustness against fractional CFO and DR if accurate time synchronization is performed. However, the presence of the DR degrades the synchronization and the decoding performance especially for the lowest data rates. Therefore, an estimation and compensation of the DR are mandatory in some cases.

Given these properties of DCSS, we propose to perform the synchronization of (2.61) by implementing the following 6 steps, detailed hereafter:

1. Preamble detection,
2. Coarse time synchronization,
3. Doppler rate estimation,
4. Fractional CFO estimation,
5. Fractional STO estimation,
6. DR, fractional CFO and fractional STO compensations.

2.5.2.1 Preamble detection

The first step in our synchronization algorithm is the detection of a signal of interest through the search of the known preamble. To this end, the receiver must be in a listening mode, which is done by multiplying each block of M samples by the complex conjugate of the reference signal as written in (2.15). Then a FFT is calculated on each blocks of non-overlapping M samples as in (2.19) and (2.25). To increase the certainty of the preamble detection, it is advantageous to average the FFT magnitudes of successive blocks before applying the *argmax* function. Indeed, since in the preamble the symbols are identical, this processing would average out the bin containing the noise, easing finding the correct one. To do this, authors in [67, 66] propose to design an IIR filter, such as $y[n] = x[n] + \beta y[n - 1]$ instead of averaging consecutive FFTs, with $\beta < 1$ is the portion of the previous block to be remembered. In this work, we chose to average the FFT magnitude over each two consecutive blocks. In addition, as stated in [67], the performance are enhanced if a threshold value according to the noise level is set to determine the presence of the signal peaks in the FFTs. Subsequently, a preamble is assumed to be detected when in $(N_p - 1)$ blocks of M samples the maximum FFT absolute value is on the same FFT bin. However, due to the fractional STO and CFO and the presence of a significant DR, the positions of the FFTs *argmax* would be shifted by several FFT bins from the beginning to the end of the preamble up-chirps. Hence, proper control procedures must be envisaged to take into account all these effects when searching for the preamble. In other words, we do not have to look for $(N_p - 1)$ consecutive peaks at the same FFT bin. In the same context, authors in [67, 83] propose to relax this constraint by searching for only $\frac{N_p}{2}$ consecutive peaks at the same frequency with a tolerance several FFT bins.

After detecting the presence of a valid preamble, our receiver should identify in which T -long sequence the received packet begins. To do this, a sequence of up chirps is applied to the T -long sections where the down chirp of the SFD is expected. The module of the FFT having the highest maximum indicates the location of the T -long section of the SFD. Given the latter position, the value of \hat{K} can be deduced.

2.5.2.2 Coarse time synchronization

Before starting the demodulation process, it is mandatory to be time synchronized at the beginning of the frame to avoid ISI. Nevertheless, thanks to the differential process, the DCSS modulation is more robust than CSS to time synchronization errors. Therefore, a time alignment that ensures a predominant cardinal sine in each FFT is sufficient to achieve accurate decoding performance. Based on this feature, we propose in this step to coarsely estimate n_s , the frame beginning. Indeed, after estimating \hat{K} and considering the distribution of $\frac{\Delta\tau}{T_s}$ in the set $[-\frac{M}{2}, \frac{M}{2})$, the signal's beginning instant n_s will be in the range of $\llbracket a \times M, b \times M \rrbracket$ with

$$a = \hat{K} - \frac{1}{2} \text{ and } b = \hat{K} + \frac{1}{2}.$$

Here, it should be noted that the maximum possible FFT magnitude is obtained in a perfect time alignment. Otherwise, the energy of the main peak will span over several bins and two cardinal sines may appear. Thus, the principle of our coarse time synchronization method is to search for the starting index that maximizes the magnitude of all FFTs in the preamble detected in step 1. Thereby, the function that we propose to maximize can be written as follows:

$$H(\omega) = \sum_{p=\omega}^{\omega+N_p+N_{sw}-1} \max_k (|Y[k, p]|), \quad \omega \in [a, b] \quad (2.48)$$

To guarantee a symmetric property between $H(a)$ and $H(b)$ (i.e. in a perfect time synchronization, no peaks would appear in the FFT before the preamble and in the one after the *sync word*), the down chirp of the SFD is inserted before the beginning of the payload. Moreover, a silence period can be considered instead of the SFD. However, the use of latter SFD is mandatory since it is deployed also in the estimation of K as presented in the previous paragraph. Indeed, this SFD can be seen as a guard interval since up and down chirps are orthogonal. Finally, \hat{n}_s the estimate of n_s , is obtained by searching the index that maximizes the function $H(\omega)$ as explained in the pseudo-code of Algorithm 1.

To reduce the computational complexity of this step we suggest to implement the maximum research by dichotomy. Furthermore, to estimate the start index of the received frame, we have to set the maximum permissible error of the Algorithm 1 to $\psi = 1$ sample, which gives a number of iterations $N_{it} = \log_2(M) = SF$.

Algorithm 1: Proposed estimation of n_s .

```

Input:  $\psi, H, a, b$ 
begin
     $I \leftarrow (b - a)$ 
     $N_{it} = \log_2\left(\frac{(b-a)M}{\psi}\right)$ 
    for  $i \leftarrow 1$  to  $N_{it}$  do
        if  $H(a) > H(b)$  then
             $b \leftarrow b - \frac{I}{2}$ .
             $\hat{n}_s \leftarrow a \times M$ 
        else
             $a \leftarrow a + \frac{I}{2}$ .
             $\hat{n}_s \leftarrow b \times M$ .
         $I \leftarrow \frac{I}{2}$ 

```

If we note $r(n)$ the coarse time synchronized signal, we have:

$$r(n) = y(n + \hat{n}_s), \quad n \in I_1 \quad (2.49)$$

with $I_1 = \{0, \dots, (N_p + N_{sw} + 1 + N_s - 1)M - 1\}$.

2.5.2.3 Doppler rate estimation

Once the coarse time synchronization is accomplished, the receiver has to estimate the DR to remove its impact on symbols estimation and to accurately perform the reminding steps of our synchronization algorithm. To note that, given the robustness of DCSS against the DR as depicted in previous section, the latter process is performed only for lowest data rate. Also, if the time synchronization algorithm is precise, the differential process makes it possible to accurately demodulate the symbols without compensating the DR, even for the lowest data rates.

In order to measure the DR, we propose an algorithm based on the estimation of the peak position in each T -long sequence of the preamble up chirps. The peak frequency values are processed in order to find the linear regression which represents the frequency slope due to the DR. The proposed algorithm, using the same principle as in [83], is summarized by the following three points:

1. Estimate the *argmax* of the FFT module in each symbol interval of the preamble. If we note \hat{i}_p the *argmax* of the FFT module in the p^{th} T -long sequence, we have:

$$\hat{i}_p = \underset{k \in \llbracket 0, M-1 \rrbracket}{\operatorname{argmax}} (|R[k, p]|) \quad (2.50)$$

with $R[k, p] = \frac{1}{\sqrt{M}} \sum_{n=0}^{M-1} \left(r(n, p) \overline{x_{ref}(n)} \right) e^{-j2\pi \frac{nk}{M}}$ and $r(n, p) = r(n + pM)$, $\forall n \in \llbracket 0, M - 1 \rrbracket$. It should be noted here that an interpolation method, as presented in 2.4.3, is used to increase the accuracy of the estimate \hat{i}_p , while in [83], a classical *argmax* function is performed.

2. The FFTs *argmax* are used in pairs to compute different DR estimates noted $\hat{c}_d^{p,l}$. These estimations are obtained using the couple $\{\hat{i}_p, \hat{i}_{p+l}\}$, with $p \in \{0, N_p - 2\}$ and $l \in \{p + 1, N_p - 1\}$. Thus, by considering (2.21) we have:

$$\hat{c}_d^{p,l} = \frac{2}{T^2} \frac{\hat{i}_{p+l} - \hat{i}_p}{l} \quad (2.51)$$

3. An estimation of the DR is obtained by averaging $\hat{c}_d^{p,l}$ as follows:

$$\hat{c}_d = \frac{1}{N_p - 1} \sum_{p=0}^{N_p-2} \frac{1}{N_p - p} \sum_{l=p+1}^{N_p-1} \hat{c}_d^{p,l} \quad (2.52)$$

We note that the estimation of the DR is done at the sampling rate $T_s = \frac{1}{f_{s_{min}}}$, while in [83] the sampling rate is equal to $\frac{1}{2f_{s_{min}}}$. Furthermore, this estimation is needed only if the frequency separation between two adjacent bins $\Delta_b = \frac{1}{T} = \frac{B}{M}$ is greater than a specific value. In this case, the compensation of the DR is mandatory before starting the estimation of the fractional offsets. In the payload, the compensation of the DR is done after the compensation of the fractional STO and perform the down-sampling at the frequency rate $f_{s_{min}}$. In the simulation results section, the robustness of our proposed receiver is tested with different separation Δ_b , i.e. different values of B and SF .

2.5.2.4 Fractional CFO estimation

In order to estimate the fractional CFO, it is mandatory first to compensate the DR. Hence, the former is compensated in the preamble as follows:

$$r_{c_d}(n, p) = r(n + pM)e^{-j\pi\hat{c}_d n^2 T_s^2}, \forall p \in \llbracket 1, N_p \rrbracket \text{ and } \forall n \in \llbracket 0, M - 1 \rrbracket. \quad (2.53)$$

Thereafter, the estimation of the fractional CFO $\hat{\nu}$ is performed using the preamble up chirps, after the compensation of the DR, via the Schmidl-Cox estimator as depicted in (2.28). We note that the compensation of the DR is mandatory to prevent the changing of the fractional CFO from one symbol to an other.

2.5.2.5 Fractional STO estimation

Once the fractional CFO and the DR are estimated, the latter are compensated in the unmodulated up chirps of the preamble to allow the receiver performing the estimation of the fractional STO λ . Unlike the algorithm from [69, 68], our proposed algorithm can estimate accurately the fractional STO with no need to compute the value of \hat{J} . Hence, a complete correction of λ and ν could be performed before the estimation of the integer offsets. To this end, we compute the following FFT, denoted $R_{c_d, \nu}[k, p]$, in the p^{th} T -long sequence of the preamble after the compensation of $\hat{\nu}$ and \hat{c}_d :

$$R_{c_d, \nu}[k, p] = \frac{1}{\sqrt{M}} \sum_{n=0}^{M-1} \left(r_{c_d}(n, p) \overline{x_{ref}(n)} e^{-j2\pi \frac{n\hat{\nu}}{M}} \right) e^{-j2\pi \frac{nk}{M}}, p \in \llbracket 1, N_p \rrbracket. \quad (2.54)$$

An estimate of the fractional STO, in the p^{th} T -long sequence of the preamble, can be obtained using an interpolation method between the FFT bins where the $\underset{k}{\operatorname{argmax}}(|R_{c_d, \nu}[k, p]|)$ is located. If we note $\hat{\lambda}_p$ this estimate and \hat{i}_p the argmax of the latter FFT using the interpolation

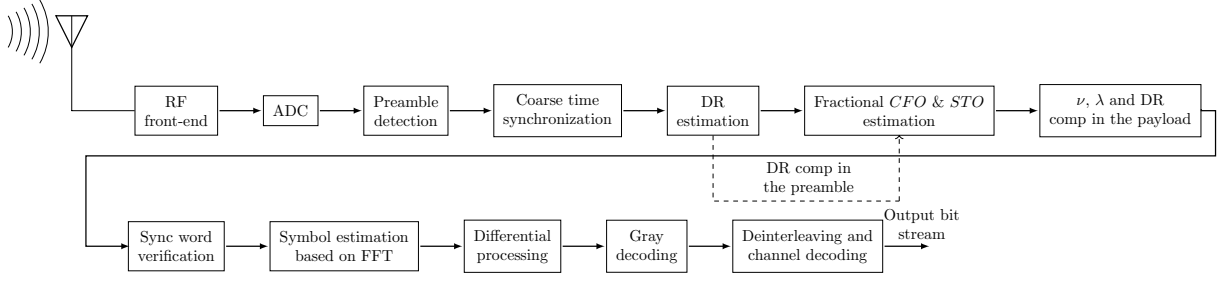


Figure 2.12: Proposed receiver architecture.

method as already explained in Section 2.4, we obtain:

$$\hat{\lambda}_p = \hat{i}_p - [\hat{i}_p] \quad (2.55)$$

Similarly to ν , the estimation of λ can be improved by using an averaging over the several preamble up chirps. The choice of this method is relevant since we propose a coarse time synchronization, that does not allow to compute \hat{J} . Thus, it is impossible to estimate λ using (2.30).

According to the patent [67] and the models described in 2.2, the interpolation works unsatisfactorily to estimate the symbols of the payload, because the modulated chirps comprise, due to the cyclical shift and fractional STO, two exponential complex signals with different phases. However, in the unmodulated up chirps of the preamble, the latter method works efficiently as will be proved in the simulation results section.

2.5.2.6 DR, fractional CFO and fractional STO compensation

The DR has been compensated in the preamble to allow accurate estimation of ν and λ . In the payload, the receiver has to compensate the fractional STO, perform the down-sampling at $f_{s_{min}}$, and then compensate the DR and ν .

To this end, based on the estimate $\hat{\lambda}$, the timing alignment is done in the decimation chain of the receivers digital front-end. Before the samples are produced at the minimum sampling frequency $f_{s_{min}}$, an oversampling $f'_s = \alpha \times f_{s_{min}}$ is considered. Indeed, the compensation of the fractional STO $[\alpha \times \hat{\lambda}]$ can be easily done by shifting the decimation operators input by a corresponding number of undecimated samples. After that, the payload is sub-sampled at the frequency rate $f_{s_{min}}$. Thus, the symbols can be easily estimated as depicted in (2.12), where the FFTs are computed as in (2.54) after the compensation of $\hat{\nu}$ and the DR.

Finally, before starting the payload decoding, the receiver has to verify the accuracy of our synchronization algorithm by finding the two special modulated symbols of the *sync word*, as depicted in Fig. 2.12 which summarizes the architecture of our proposed receiver.

2.5.3 Results and Discussions

In this section, we aim to evaluate the performance of our proposed receiver to perform accurate synchronization and decoding of the received DCSS signals in a LEO satellite communication scenario. To conquer this challenge, we propose to perform Monte Carlo based simulations, with significant number of repetition per SNR. The simulation results we present are obtained from a DCSS signal simulator that we developed in MATLAB. Thus, we simulate the interleaving and de-interleaving blocks, but also the channel coding/decoding parts. Based on the robustness of the DCSS waveform against the CFO, the STO and especially the Doppler time-variation as proved in section 2.4, we show the ability of this waveform associated with our original synchronization algorithm to demodulate LEO satellite signals. Finally, we validate the efficiency of our technology using real DCSS deployment scenario.

In the following, we consider in all the simulations that the number of preamble up chirps $N_p = 8$, an oversampling factor $\alpha = 8$ and a reference bandwidth $B_{ref} = 125$ kHz, which is the most commonly used bandwidth in LoRa-based networks. In this section, we use data provided by Eutelsat [84].

As depicted in Fig. 1.3 showing the variation of the DR and Doppler shift over visibility window of Eutelsat nano-satellite with a typical altitude of 550 km, it can be seen that in the worst case the DR can reach 280 Hz/s. We note here that along the packet duration the DR can be modeled as a linear shift variable in time. Whereas the Doppler shift can achieve 19 kHz. This significant Doppler shift, related to the satellite motion, combined with local oscillators instability leads to huge CFO values. Therefore, our proposal, which allows decoding LoRa-like signals whatever the frequency offset, would be a very promising solution for ultra narrow band (UNB) communication with LEO satellite using chirped signals.

Table 2.1: Simulation parameters

Carrier frequency f_c (MHz)	868
Maximum CFO Δf_{max} (kHz)	50
DR (Hz/s)	280
Transmitted power P_{Tx} (dBm)	14

As depicted in Table 2.1, our receiver has to deal with significant CFO value (i.e. $\Delta f_{max} > \frac{B_{ref}}{4}$) and fastest Doppler variation in LEO satellite communication.

2.5.3.1 Synchronization algorithm numerical results

In the following simulations, we consider the worst case scenario of LEO satellite communication as proposed in Table 3.2.

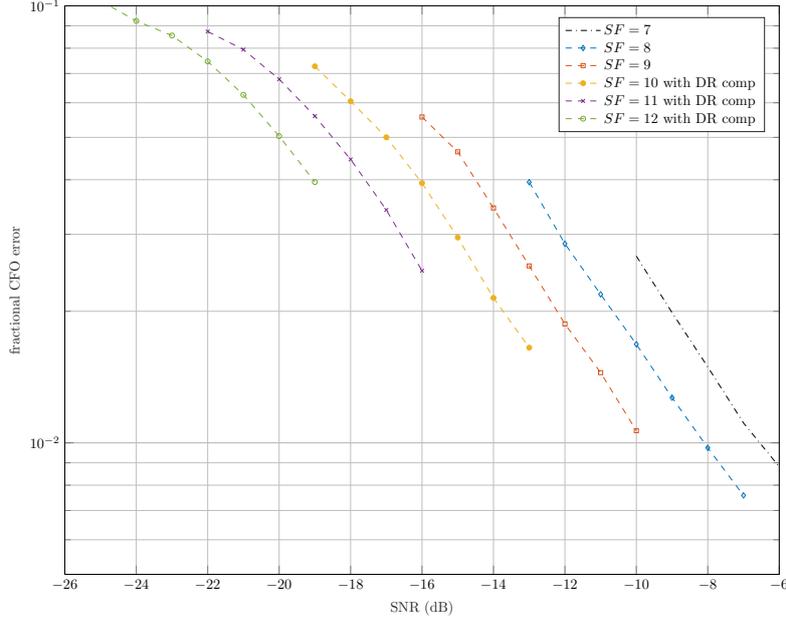

 Figure 2.13: Fractional CFO estimation error ϵ_ν .

Fig. 2.13 shows the estimation error of the fractional CFO $\epsilon_\nu = |\nu - \hat{\nu}|$ for all the possible SF s. It can be seen that the estimation of ν is more precise for the lower SF (i.e. $SF \in \{7, 8, 9\}$) since a DR of 280 Hz/s does not affect the synchronization and the decoding performance of the latter SF s. In addition, the highest SF s has the lowest bin separation which makes them more sensitive to the fractional offsets and the DR. Thus, for $SF \in \{10, 11, 12\}$, the DR should be corrected in order to estimate ν , otherwise the latter offset will vary rapidly along the preamble unmodulated chirps.

In Fig. 2.14, we represent the start of frame error $\epsilon_{n_s} = \left| \frac{n_s + \lambda - (\hat{n}_s + \hat{\lambda})}{M} \right|$ as function of the SNR for each SF . We can notice that our time synchronization algorithm has a good precision since, for instance, $\epsilon_{n_s} = 0.017$ (resp. $\epsilon_{n_s} = 0.021$) at the SNR sensitivity threshold [54] of $SF = 7$ (resp. $SF = 12$). In [85] and in the previous section, we showed that DCSS can maintain good decoding performance for timing errors ϵ_{n_s} of 0.25. Hence, given the time synchronization accuracy of our algorithm and the robustness of DCSS, we expect to have good decoding performance of our receiver.

2.5.3.2 Decoding performance of the proposed receiver

After evaluating the performance of our receiver to estimate the parameters needed to perform an accurate synchronization, we represent in Fig. 2.15, a comparison of the decoding performance of our receiver and a classic LoRa one as function of the CFO. In this figure, we represent the PER with a number of transmitted packets equals to 10^4 and a SNR equals to -5 dB. This simulation confirms the constraint of a maximum allowed CFO of $\frac{B}{4}$ for LoRa receivers, which

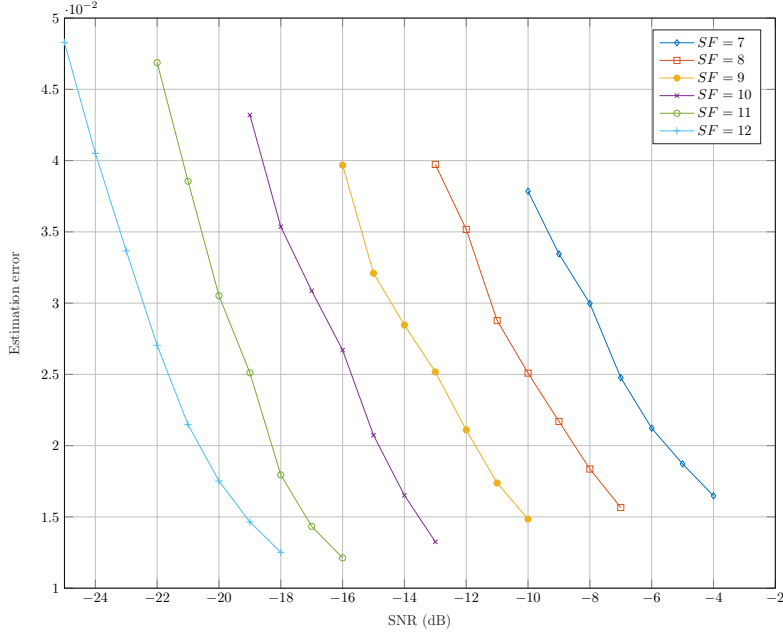


Figure 2.14: Beginning time estimation ϵ_{n_s} .

is not the case when adopting our approach due to the proposed synchronization strategy.

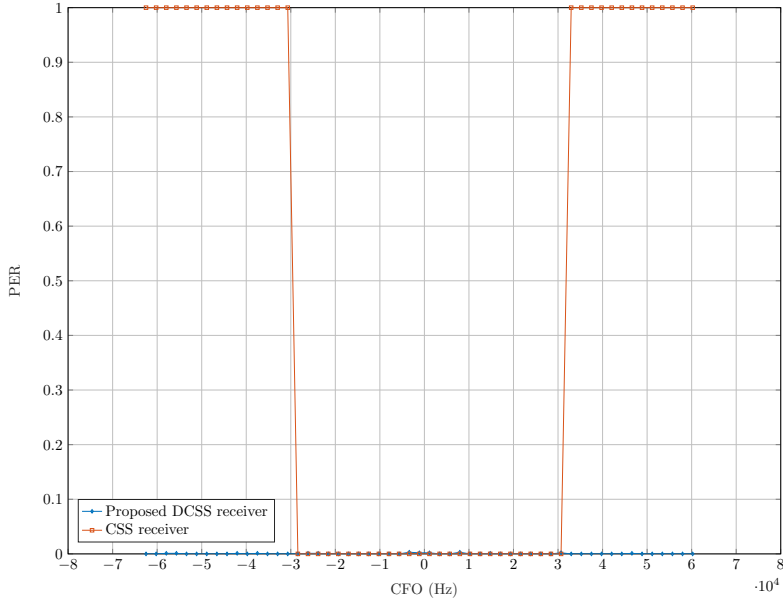


Figure 2.15: PER of CSS and DCSS receivers as function of the CFO with $SF = 7$, $SNR = -5$ dB and $B = B_{ref}$.

We compared in Fig. 2.16 the robustness of DCSS and CSS waveforms against the DR under AWGN channel. In Fig. 2.16, we propose the same comparison between our DCSS receiver and CSS one, as described in [68], in the presence of the STO and CFO but without compensating the DR. In this simulation, we used the configuration ($SF = 9$, $B = \frac{B_{ref}}{2^3}$) which

has the same robustness to the DR as ($SF = 12$, $B = B_{ref}$). We notice in this figure that the CSS receiver is very sensitive to the Doppler variation since, for a DR = 10 Hz/s, an almost constant PER of 0.5 is obtained for SNRs greater than -13 dB. On the other hand DCSS receiver maintains acceptable decoding performance for DR values lower than 70 Hz/s. However, we notice that the robustness of both receivers to DR in the presence of the CFO and the STO are lower than the perfect synchronization case as present in 2.16, since an uncompensated DR would affect the estimation of the latter desynchronization parameters.

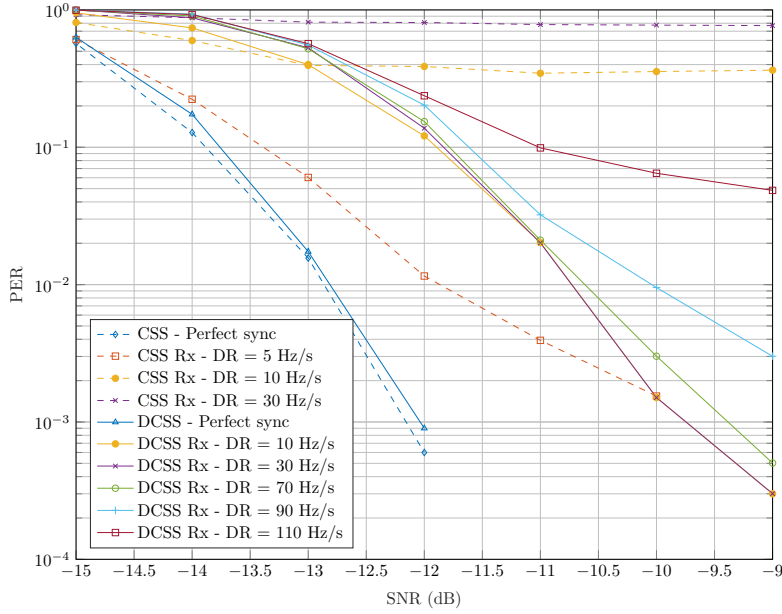
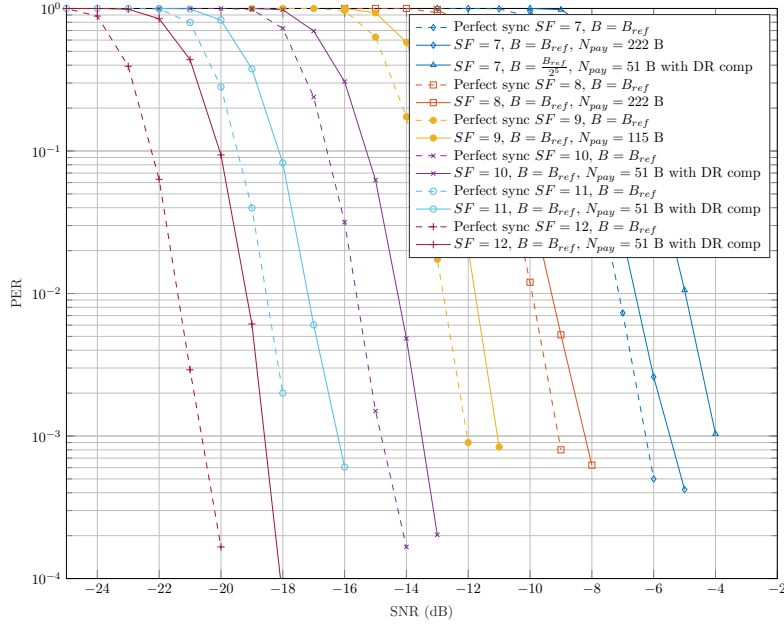


Figure 2.16: PER of CSS and DCSS receivers for different DR values, with $SF = 9$, $B = \frac{B_{ref}}{2^3}$, $N_{pay} = 51$ bytes and $CR = 1$.

Fig. 2.17 states the result of PER of our proposed receiver as function of the SNR for all the SF 's. We note here that we consider the worst case of DR and the maximum of payload size with each SF as defined by LoRaWan standard in [86]. Thanks to the accuracy of our synchronization algorithm and the robustness of DCSS technique to CFO and some STO values, we notice in Fig. 2.17 that the decoding performance of our receiver are slightly degraded compared to the perfect synchronization case. It can be seen that PER is slightly increased for the lowest bin separation Δ_b (i.e. slowest data rates, $SF \in \{10, 11, 12\}$). This result is explained by a higher sensitivity of the latter SF 's to the time-varying Doppler shift and the fractional CFO. We can notice also that the performance degradation compared to the perfect synchronization case of the configuration $SF = 12$ and $B = B_{ref}$ is almost the same than $SF = 7$ and $B = \frac{B_{ref}}{2^5}$ since they have the same bin separation. It should be noted also that these two configurations have the same link budget.


 Figure 2.17: PER evolution of the proposed DCSS receiver with $CR = 3$

Finally, we represent in Fig. 2.18 the SNR evolution of an uplink line of sight communication between an Eutelsat satellite and a terminal in its field of view (FoV) as function of time. We show also the elevation angle from the terminal to the satellite during the visibility window [23]. Let $d_u(t)$ the distance between the satellite and the user device, that depends on the elevation angle of the satellite during its window of visibility. The SNR acquisitions, as showed in Fig 2.18, are obtained using the following equation:

$$\begin{aligned} \text{SNR} \Big|_{\text{dB}} &= P_{Tx} \Big|_{\text{dBm}} + G_{TX} \Big|_{\text{dBi}} + L_{FS} \Big|_{\text{dB}} + L_{At} \Big|_{\text{dB}} + L_P \Big|_{\text{dB}} \\ &+ G_{Rx} \Big|_{\text{dBi}} - 10 \log_{10}(k_B T_N B) - 30 \end{aligned} \quad (2.56)$$

In these measurements, an omnidirectional transmit antenna having a gain $G_{Tx} = 0$ dBi, a directional receiver antenna with a gain $G_{Rx} = 8$ dBi, atmospheric loss $L_{At} = 1$ dB and a polarization mismatch $L_P = -3$ dB were considered

To note that the latter SNR acquisitions are presented to determine which B and SF configuration have a sufficient range for such communication.

By referring to the curves of the PER as function of the SNR in Fig. 2.17, we propose to define the SNR sensitivity threshold SNR_{th} , in this case as the minimum SNR that guarantees a PER lower than 10^{-2} . Using the latter SNR threshold value we can easily compute the sensitivity of our receiver as depicted in (1.10).

Table 2.2: Receiver sensitivity S dBm for different SF and B values

(SF, B)	$(12, B_{ref})$	$(11, B_{ref})$	$(10, B_{ref})$	$(9, B_{ref})$	$(8, B_{ref})$	$(7, B_{ref})$	$(7, \frac{B_{ref}}{2^5})$
SNR_{th} (dB)	-19.5	-17.5	-14.5	-11.8	-9.2	-6.5	-5
S (dBm)	-136.53	-134.53	-131.53	-128.83	-126.23	-123.53	-137.08

At the farthest distance d_{max} between the satellite and the terminal device (i.e. $d_u(t) = d_{max}$ at the elevation angle of 20°), the measured SNR is equal to -19 dB. The latter measurement gives a received power of -136 dBm. We represent in Table 2.2, based on Fig. 2.17 and (1.10), the sensitivity of our proposed receiver for each SF and B configuration by considering $NF = 6$ dB. The results of the latter table prove that only $SF = 12$ with $B = B_{ref}$ and $SF = 7$ with $B = \frac{B_{ref}}{2^5}$ can fulfill the sensitivity requirements for all the SNR measurements by the Eutelsat satellite. Hence any transmitted signal has the same bin separation as $\Delta_b = \frac{B_{ref}}{2^{12}}$ would be suited for this communication. It should be noted also that an adaptive data rate communication according to the position of the satellite could be considered.

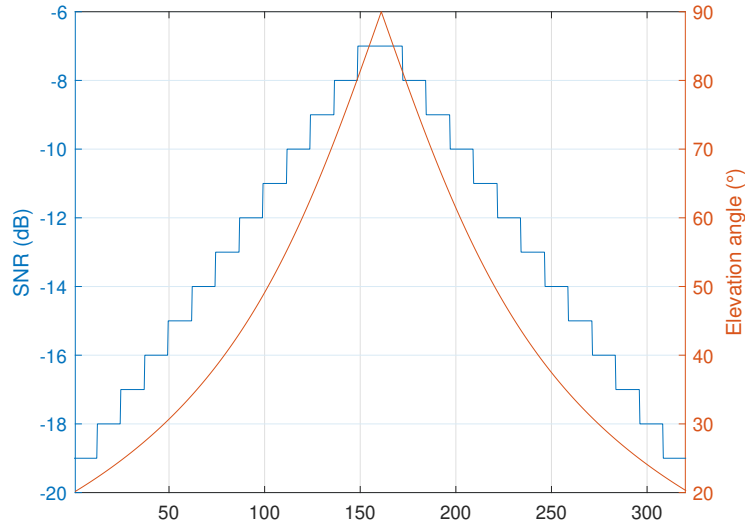


Figure 2.18: Evolution of the SNR (dB) and elevation angle as function of time for Eutelsat satellite.

In the next section, we will present our second DCSS-based transceiver suited also for LEO satellite communications.

2.6 Dual Waveform DCSS Transceiver

As in the previous section, we aim to take full advantage of a differential processing in the CSS signals by not trying to estimate and track the frequency synchronization parameters. To

conquer this challenge, we propose a new transceiver, based on the DCSS technique, able to perform accurate time synchronization regardless of the CFO using a non-chirp-based waveform in the preamble. The adopted waveform in this training sequence should be insensitive to the instantaneous phase variation, robust against in-band interference and remain at constant envelope, which allows an optimal power amplification function and does not increase the energy consumption of the nodes. As for the previous proposed receiver, this processing would break the glass of the maximum CFO estimable of $\frac{B}{4}$ and makes it possible to consider, if the communication rate allows it, reducing the bandwidth B while keeping the LOs currently used in low-cost IoT technologies. Hence, we can increase the capacity of LoRa-based networks by adopting our approach. In addition, our receiver is much more robust to the Doppler time-variation than the existent LoRa ones. All these features make our proposition good candidate for LEO satellite communications, as detailed hereafter.

2.6.1 Proposed Transmitted Signal

As in the transceiver presented in the previous section, our proposition aims at fully exploiting the immunity of DCSS to the CFO, especially when the latter is time varying, which is not the case when adopting chirp-based preamble as in the literature. For this purpose, we propose to use a waveform in the preamble insensitive to the instantaneous phase variation and allowing to estimate the time desynchronization regardless to the CFO and the Doppler time-variation, which is not the case in the current LoRa receivers. Moreover, the proposed waveform as a training sequence in the preamble should not introduce any particular constraints from a circuit and system point of view. More precisely, this waveform should remain at constant envelope, which allows an optimal use of the power amplification function. The objective of using the latter type of training sequences is to be able to detect the time arrival of the packet to be decoded with sufficient accuracy to ensure proper demodulation of the payload chirps. As with any training sequence, our preamble must have good auto-correlation properties. Furthermore, in order to guarantee the ability of the receiver to identify the SF used by the transmitter, it must provide at least as many orthogonal training sequences as existing SF s. Finally, the latter sequences must be detected without deteriorating the sensitivity of the receiver. In other words, the detection probabilities of the training sequences must be at least equivalent to the chirp-based ones. Thus, if we note $s_p^j(t)$ the training sequence associated with the spreading factor $SF = j$, ideally the sequences should be such that:

$$R_{i,j}(\tau) = \frac{1}{\sqrt{E_p^i E_p^j}} \int_{\mathbb{R}} s_p^i(t) \overline{s_p^j(t - \tau)} dt = \delta_{i,j} \quad (2.57)$$

where $\delta_{i,j}$ is the Kronecker symbol, E_p^i and E_p^j are the energies of $s_p^i(t)$ and $s_p^j(t)$ respectively.

In the literature, it exists several sequences with good auto and cross-correlation properties. For instance, this is the case of the binary sequences of Gold [87] or Hadamard [88]. Without loss of generality, we consider to use Gold sequences in the following.

We consider Gold sequences of length N_{bp} and that the bits of this sequence are generated at a rate $D_{bp} = \frac{1}{T_{bp}}$ bits/s. Thus, if we note b_k the bit of the sequence generated at kT_{bp} , then the signal associated with the Gold sequence is expressed as:

$$s_p(t) = \sum_{k=0}^{N_{bp}-1} b_k g(t - kT_{bp}) \quad (2.58)$$

with $g(t)$ being the pulse shaping filter and N_{bp} being the number of bits in the sequence. $g(t)$ and D_{bp} must be chosen so that the energy of $s_p(t)$ is well localized in time and frequency and that $s_p(t)$ is naturally insensitive to the CFO. By choosing $g(t) = 1, \forall t \in [0, T_{bp}]$, then $\forall f_d(t)$:

$$|s_p(t)e^{j\pi f_d(t)t + j\phi_d}| = s_p(t) \quad (2.59)$$

In order to limit the out-of-band energy, we have considered the bit rate $D_{bp} = \frac{B}{G}$, with $G \gg 1$.

Given the choice of the latter preamble, the signal transmitted by the DCSS transmitter can be written as:

$$x(t) = s_p(t)\mathbb{1}_{[0, T_p]}(t) + s(t - T_p)\mathbb{1}_{[T_p, T_p + N_s \times T]}(t) \quad (2.60)$$

with $T_p = N_{bp} \times T_{bp}$.

Based on this dual waveform that composes the transmitted signal, we present in the following the associated receiver.

2.6.2 Proposed Receiver

We consider in this paragraph that the continuous-time version the signal received at the satellite can be written as in (2.45). As previously, to correctly obtain the radio frequency signal and due to the CFO, the analog to digital converter output signal should be sampled with $f_s = \frac{1}{T_s}$ greater than the Nyquist rate $f_{s_{min}} = B$, with an oversampling $\alpha = f_s / f_{s_{min}}$. Hence, after the different processing carried out on the radio frequency front-end, the complex envelope of the signal, reconstructed after analog-to-digital conversion at the sampling rate $T'_s = \frac{1}{\alpha \times f_{s_{min}}}$ is written as:

$$y(n) = \sqrt{P}x(n - n_s)e^{j(2\pi(\Delta f + \frac{c_d \cdot n T'_s}{2})n T'_s + \varphi_0)} + w(n) \quad (2.61)$$

where $n_s = \left\lceil \frac{t_s}{T'_s} \right\rceil$ is the beginning index of the frame if we use the sampling rate T'_s . It should be noted that the oversampling will allow to enhance the precision of time alignment of the

receiver and no further fractional STO estimation is needed.

In order to find the beginning index of the packet received for each $SF = j$, we compute the following normalized cross-correlation function:

$$\rho(n_i) = \frac{\sum_{n=n_i}^{n_i+N_s^p} |y(n)| \overline{s_p^j(n-n_i)}}{\sqrt{\sum_{n=0}^{N_s^p} |s_p^j(n)|^2} \cdot \sqrt{\sum_{n=n_i}^{n_i+N_s^p} |y(n)|^2}} \quad (2.62)$$

with $N_s^p = \lfloor \frac{T_p}{T_s} \rfloor$ being the number of samples in the preamble. Hence, if we note \hat{n}_s the estimate of n_s , we have:

$$\hat{n}_s = \arg \max_{n_i} |\rho(n_i)| \quad (2.63)$$

Given (2.62), $\forall n_s |\rho(n_s)| \leq 1$, thus in order to detect the presence of the preamble in the recorded signal and to launch the frame decoding processing, it is necessary to check if the result of cross-correlation exceeds a threshold value which it is necessary to define *a priori*. It should be noted that this threshold value is set to find a good compromise between missed detection and the false alarm probabilities. Yet, in this work we suppose that the signals are systematically received. Hence we do not investigate here the detection performance as function of the latter threshold.

If we note $r(n)$ the time-synchronized signal, we have:

$$r(n) = y(n + \hat{n}_s), \quad n \in I_2 \quad (2.64)$$

with $I_2 = \{0, \dots, N_p^s + \alpha N_s M - 1\}$.

After performing the time synchronization of the received signal, the latter is sub-sampled at the rate $T'_s = \frac{1}{f_{s_{min}}}$. Then the estimation of the symbols in the payload is performed as detailed in the previous section.

In the next section, we present simulation results to demonstrate the efficiency of our dual waveform DCSS receiver when a LEO satellite communication scenario is considered.

2.6.3 Results and Discussions

In this subsection, we aim to evaluate the performance of the “hybrid” DCSS transceiver to perform accurate time synchronization and decode the received packets in the presence of Doppler effects typical to a LEO satellite communication scenario. In the following, we consider in all the simulations an oversampling factor $\alpha = 8$ and a bandwidth of reference $B_{ref} = 125$ kHz.

To that end, due to the Doppler shift and the frequency mismatches of low-cost LOs, we consider a CFO Δf uniformly distributed in $[-B, B]$ and the DR is uniformly distributed in

$[-DR_{max}, DR_{max}]$. Based on [83], we consider in the following that DR_{max} is equal to 250 Hz/s. Moreover, as we have already explained, satellite communication with Earth entails very important interference level giving the huge number of connected devices. Subsequently, to verify that our synchronization algorithm is not affected by intra-technology interference, we test in the following the mutual impact between gold sequences and the chirps of the payload. Thus, given the structure of the transmitted packets, 4 types of destructive interference can occur between two packets:

- I_{p-p} : Interference between two preambles having the same Gold sequence.
- I_{p-c} : A preamble interfering with payload chirps.
- I_{c-p} : Payload chirps interfering with a preamble.
- I_{c-c} : Interference between two payloads.

In Fig. 2.19 and Fig. 2.20, we show respectively the time synchronization error $\epsilon_{n_s} = \frac{|n_s - \hat{n}_s|}{\alpha M}$ and the BER as function of the SNR with different interference scenarios. It should be noted that only the interference on the preamble is tested in Fig. 2.19 (i.e. I_{c-p} and I_{p-p}), since in these scenarios the performance time synchronization will be affected. The results depicted in these figures are given with $SF = 7$ and $B = \frac{B_{ref}}{2^5}$, which have the same data rate as the case of $SF = 12$ and $B = B_{ref}$. As previously explained, these two configurations have the same link budget and the same separation between adjacent bins $\Delta_b = \frac{B}{M}$, which induces the same robustness to Doppler variation. Moreover, we define the signal to interference ratio (SIR) as $\frac{P}{P_i}$, where P_i is the received power of the interfering signal. In this simulation, we consider a training sequence having the same duration as the conventional LoRa preamble. Indeed, if we note N_p the number of up chirps in the latter preamble then we have:

$$N_{bp} = N_p \times T \times D_{bp} = \frac{N_p M}{G} \quad (2.65)$$

A typical value of N_p used to perform the synchronization in LoRa is 10. This value will be considered in the following.

We can easily notice in Fig. 2.19 the good performance of our time synchronization algorithm in the case without interference, especially when we decrease G and hence increase N_{bp} which guarantee better auto-correlation proprieties of the training sequence. For instance, at the SNR sensitivity threshold (i.e. the SNR associated to a BER of 10^{-5} in LoRa communication) which equals to -6 dB with $SF = 7$ [75]), ϵ_{n_s} is equal to 2×10^{-4} (resp. 7×10^{-4}) in the case without interference with $G = 5$ (resp. $G = 10$). We notice also that, with the same conditions except for the maximum CFO which is equal here to $\frac{B}{4}$, LoRa receiver cannot perform accurate time synchronization because of the Doppler variation. Furthermore, our preamble shows high

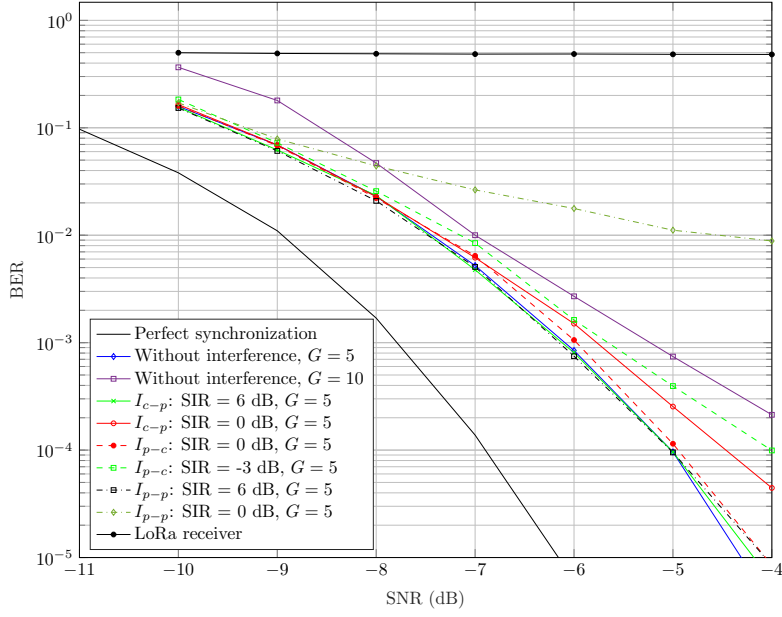


Figure 2.20: BER evolution with $SF = 7$ and $B = \frac{B_{ref}}{2^5}$.

robustness against interfering signals (i.e. interference scenarios I_{p-p} and I_{c-p}). Indeed, it can be seen that, in the two interference scenarios with SIR = 6 dB, there is almost no loss in the estimation precision compared to the case without interference.

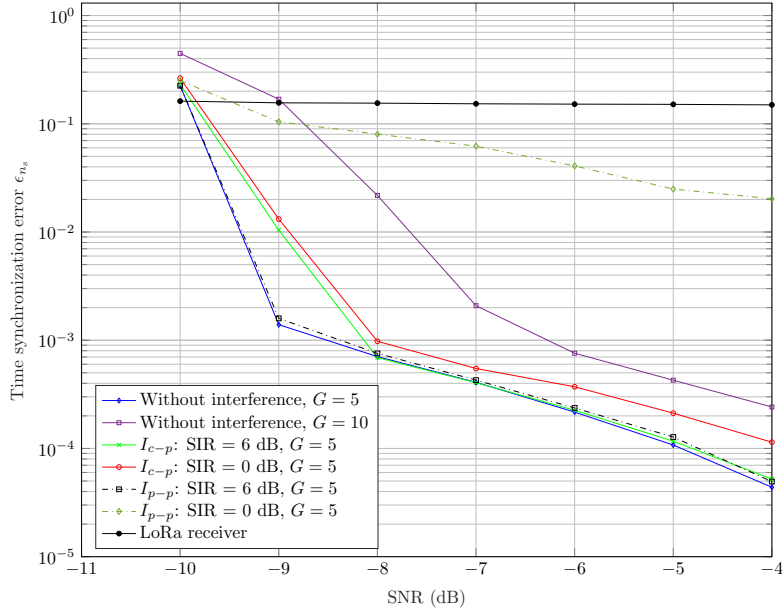


Figure 2.19: Time estimation error ϵ_{n_s} with $SF = 7$ and $B = \frac{B_{ref}}{2^5}$.

Given the latter accurate time synchronization and the robustness of DCSS technique to the Doppler variation, we expect to have good decoding performance of our receiver. We can see in Fig. 2.20 that our receiver causes a loss of only 2 dB of SNR sensitivity threshold

compared to the case of perfectly synchronized DCSS communication. This loss is explained by the fractional CFO which degrades the magnitude of peaks in the FFTs. Since we do not compensate the DR in this work, the impact of the latter fractional offset cannot be avoided. In the presence of interference, the decoding performance are slightly affected. For instance in the case interference on the preamble (i.e. I_{p-p} and I_{c-p}), we showed that our receiver performs accurate time synchronization, especially when the SIR greater than 6 dB for I_{p-p} . Hence as depicted in Fig. 2.20 the curves of BER, in the latter cases, are slightly degraded compared to the case without interference. Whereas, if the packet payload is interfered with the proposed preamble (i.e. I_{p-c}), we showed in [89], the high robustness of CSS against narrow band signals and this result is confirmed in Fig. 2.20. Finally, for the interference case I_{c-c} , we proved in [75], that the signal of interest is well decoded if the SIR is greater than 6 dB.

2.7 Conclusion

In this chapter, we discussed the synchronization issues of LoRa-like signals. We modeled at first the impact of the time and frequency desynchronizations on symbols estimation. We explained by mathematical models and simulation that the estimation of the fractional offsets, especially the fractional STO, is a challenging task. We demonstrate also that the decoding performance are clearly degraded if the latter offsets are not estimated with a sufficient precision. Moreover, we proved that the method used to estimate the integer offsets leads to a maximum CFO estimable of $\frac{B}{4}$. An other synchronization issue, that could considerably degrade the decoding performance of LoRa-like signals, is the Doppler time-variation along the packet duration. Given the significant Doppler shift and DR induced by the LEO satellite motion, the deployment of LoRa technology for such communication is a very challenging task. To conquer this challenge, we proposed a modification of the LoRa PHY layer which we refer to as DCSS associated with original synchronization algorithms. In the first algorithm, we almost maintain the same structure of the conventional LoRa preamble to perform the time synchronization regardless to the CFO. In the former algorithm, it is mandatory to compensate the DR with the lowest data rate to avoid the degradation of the performance. Whereas, in the second algorithm, the same task is fulfilled by using a waveform insensitive to the instantaneous phase variation in the preamble. Thereby, based on these modifications our proposed receivers can handle UNB LoRa-like signals since it has no limitation on the maximum CFO that could be estimated, as it is actually the case in the current LoRa receivers. In addition, in the presence of the Doppler shift varying along the packet duration, DCSS shows better performance than CSS, which makes our proposed receivers good candidates for LEO satellite communications.

After dealing with the synchronization challenges when communicating with LEO satellites, we focus in the next chapter, on the interference issues caused by the FoV of the latter satellites,

which allow to connect huge number of end-devices. Thus, we propose novel approaches to deal with distinctive LoRa-like collisions in uplink and downlink contexts.

CHAPTER 3

Interference management of LoRa-like communications with LEO satellites

In the previous chapter, we proposed a study on the impact of synchronization errors on LoRa-like symbol estimation, when LEO satellite communications are considered. Then, we provided two synchronization algorithms associated with the DCSS modulation to cope with the impact of Doppler effects when considering such communication scenario. In this chapter, we will deal with an other challenge of satellite IoT, which is the high interference level caused by the FoV of a LEO satellite, which allows to connect huge number of end-devices. More precisely, if LPWAN technologies in ISM bands, such LoRa-based networks, are deployed to establish such communication, packets collisions will be caused by uncoordinated LoRa transmissions and the ones from other ISM technologies. As already explained, LoRa-based networks have a severe problem to deal with same-technology interference, especially the destructive collisions when two or more signals are simultaneously received over the same channel with the same SF . Moreover, currently the technologies that may coexist with LoRa in LEO satellite communication are mostly based on the UNB PHY layer, such as Sigfox and LR-FHSS. Thus, we start this chapter by studying, in Section 3.1, the impact of UNB interfering signals on LoRa-like communication to quantify the robustness of the latter waveform in such scenario. Then, in Section 3.2, we evaluate its robustness to same-technology interference by modeling the impact of the inter- SF and same- SF collisions on the decoding performance of a LoRa-like signal of interest. Based on these results, we represent in Section 3.3, a novel receiver able to decode several superposed LoRa-like signals using the SIC algorithm. Whereas, in Section 3.4, a similar approach is developed in a downlink communication case by adding a power diversity that can replace the SIC algorithm in several configurations. Finally, we provide, in Section 3.5, an original packet detection algorithm suited to the massive connectivity with LEO satellite as well

as low-connectivity scenarios, when covering mountains, oceans, etc.

3.1 Impact of UNB interfering signals on LoRa

As already mentioned, if we aim to deploy LoRa-like communications with LEO satellites, it is very likely to survive inter-technology interference from other technologies using ISM bands for the same purpose. The majority of the latter technologies, such Sigfox and LR-FHSS use UNB transmissions to communicate with LEO satellite. Hence, in this section we model the impact of UNB interfering signals on LoRa-like communications. Then, based on the elaborated models, we present several results allowing to quantify the impact of such interference on the decoding performance of the signal of interest.

3.1.1 Interference Model

One of the main problems with the coexistence of networks based on LoRa-like and UNB-IoT PHY layers in the ISM bands is the packet collisions. The objective of this section is to theoretically present the impact of UNB communications on a LoRa-like signals.

To model our system, we present in Fig. 3.1 an illustrative scheme scaling UNB and CSS interference model. To note that T^{nb} and B_{nb} are respectively the symbol time and the bandwidth of the UNB interfering signal. It can be seen in this figure that the interference duration of the UNB symbol on the CSS one is relatively small due to ultra narrow bandwidth B_{nb} of the latter interfering symbol. In the following, we consider that the receiver is perfectly time/frequency synchronized on the CSS signal. In addition, the impact of the DR is neglected for the UNB interfering signal since we suppose that it is the same as for the CSS signal and we accurately compensated in the synchronization processing of the latter.

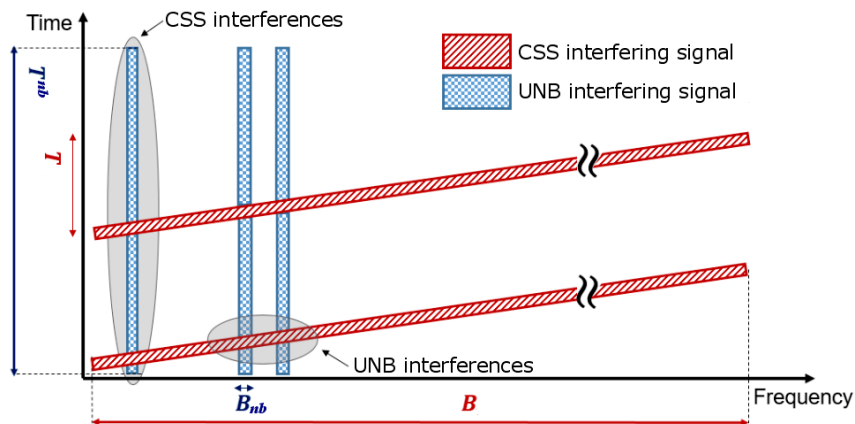


Figure 3.1: interference model between UNB and CSS symbols.

To analyse the impact of UNB communication on the decoding of a CSS signal of interest, we consider a LoRa-like signal $s(t)$ in the presence of several UNB interferences $s_{nb,i}(t)$, $i \in \{1, \dots, N_{int}\}$, with N_{int} being the number of UNB interfering signals. Thus, the received signal at a gateway demodulating LoRa-like signals, sampled at the Nyquist rate $T_s = \frac{T}{M}$, is given by:

$$y^l(nT_s) = \sqrt{P}s(nT_s) + \sum_{i=1}^{N_{int}} \sqrt{P_{nb,i}}nT_s + w(nT_s) \quad (3.1)$$

where

- P : received power of the CSS signal,
- $P_{nb,i}$: received power of the i^{th} UNB interfering signal,
- $s_{nb,i}(nT_s)$: i^{th} UNB interfering signal.

In addition, by defining for the i^{th} UNB interfering signal:

- $f_{c,i}$: the baseband carrier frequency,
- $\Delta\tau_i$: the time desynchronization,
- $A_{i,k'}$: the symbol transmitted at the time $k'T^{nb}$,

we obtain:

$$s_{nb,i}(nT_s) = \sum_{k'=1}^{N_s^{nb,i}-1} A_{i,k'}g(nT_s - k'T^{nb} - \Delta\tau_i)e^{j2\pi f_{c,i}nT_s} \quad (3.2)$$

with $N_s^{nb,i}$ is the number of transmitted symbols by the i^{th} interfering signal.

As previously explained, knowing the complex envelope of the raw chirp, the digital demodulation of the p^{th} CSS transmitted symbol is obtained during the following time interval: $(p-1)T \leq t < pT$. If $r_p^l(nT_s)$, $n \in \llbracket 0, M-1 \rrbracket$ corresponds to the signal processed by the CSS demodulator, we have:

$$\begin{aligned} r_p^l(nT_s) &= y^l(nT_s + pT)\overline{x_{ref}(n)} \\ &= s_p(nT_s) + \sum_{i=1}^{N_{int}} i_{p,i}^{nb}(nT_s) + w_p(nT_s) \end{aligned} \quad (3.3)$$

In this case, as previously proved, the useful signal and the noise term are respectively equal to:

$$s_p(nT_s) = \sqrt{P}e^{j2\pi \frac{S_p n}{M}} \quad (3.4)$$

and

$$w_p(nT_s) = w(nT_s + pT)\overline{x_{ref}(n)} \quad (3.5)$$

Whereas the i^{th} UNB interfering signals, $i_{p,i}^{nb}(nT_s)$, is given by:

$$\begin{aligned} i_{p,i}^{nb}(nT_s) &= \sqrt{P_{nb,i}} s_{nb,i}(nT_s + pT \Delta\tau_i) \overline{x_{ref}(n)} \\ &= \sqrt{P_{nb,i}} \sum_{k' \in \mathbb{Z}} A_{i,k'} g(nT_s + pT - k'T^{nb} - \Delta\tau_i) e^{j2\pi f_{c,i}(nT_s + pT)} \overline{x_{ref}(n)} \end{aligned} \quad (3.6)$$

Here we notice that the receiver is perfectly synchronized on the received CSS signal and we suppose that the interfering signals do not affect this synchronization process.

The interference between a CSS symbol and a UNB signal occurred only when they overlap in the time and the frequency domains. This interference is characterized by the duration in which CSS symbol crosses the UNB bandwidth B_{nb} . Furthermore, the samples of $s_{nb,i}(nT_s + pT)$ that interfere with the p^{th} CSS symbol are:

$$\begin{aligned} \Delta n_{int} &= \{[n_1, n_2] \subset \llbracket 0, M - 1 \rrbracket, \forall n \in [n_1, n_2], \\ f_p(nT_s) &\in [f_{c,i} - \frac{B_{nb}}{2}, f_{c,i} + \frac{B_{nb}}{2}]\} \end{aligned}$$

Where $f_p(nT_s)$ is defined as in (2.2), with $f_p(nT_s) = f^{S_p}(nT_s)$. Without loss of generality, the latter chirp is considered as an increasing function $\forall n \in [n_1, n_2]$. Thus, the number of interfering samples is given by:

$$n_{int} = \frac{B_{nb}M}{B^2T_s} = \frac{B_{nb}M}{B} \quad (3.7)$$

This proves that the number of interfering samples between CSS and UNB symbols increases by increasing the SF and the bandwidth of the UNB signal and decreases by increasing the bandwidth of the CSS signal. Then, the i^{th} UNB interfering signal sampled at T_s , denoted by $i_{p,i}^{nb}(nT_s)$, with $n \in \llbracket 0, M - 1 \rrbracket$, is defined as:

$$i_{p,i}^{nb}(nT_s) = \begin{cases} 0 & \text{for } n \in \llbracket 0, M - 1 \rrbracket \setminus [n_1, n_2] \\ (3.6) & \text{otherwise} \end{cases} \quad (3.8)$$

As previously explained, the optimal estimation of symbol S_p can be performed by searching for the maximum of $r_p(nT_s)$ periodogram. If we note $R[k, p]$, $k \in \llbracket 0, M - 1 \rrbracket$, the FFT of

$r_p^l(nT_s)$ we have:

$$\begin{aligned} R[k, p] &= \frac{1}{\sqrt{M}} \sum_{n=0}^{M-1} r_m^l(nT_s) e^{-j2\pi \frac{nk}{M}} \\ &= \sqrt{PM} \delta(k - S_p) + I_{nb}[k, p] + W[k, p] \end{aligned} \quad (3.9)$$

where $I^{nb}[k, p]$ and $W[k, p]$ are the FFT of the UNB interference and the noise respectively. The estimation of the p^{th} CSS symbol is then given by:

$$\hat{S}_p = \underset{k \in \llbracket 0, M-1 \rrbracket}{\operatorname{argmax}} (|R[k, p]|) \quad (3.10)$$

The decision on the symbol S_p is perturbed by the noise and the interference terms. The interference term $I^{nb}[k, p]$ is the sum of the DFTs of the interfering signals defined in (3.8) which have the symbol interference duration as depicted in (3.7). We will use these expressions to numerically evaluate, the UNB signal impact on the LoRa symbol demodulation.

3.1.2 Results and Discussions

First of all, we choose to analyze the impact of UNB signals on LoRa-like communications, by observing the performance degradation on the BER. Without loss of generality, we consider that the digital modulation used by the UNB system is a differential binary phase shift keying (DBPSK), typical for Sigfox uplink transmissions, and that the signals are systematically in collision over their entire duration. The degradation related to every interference scenario is compared to the theoretical BER for CSS or DBPSK modulations without interference as depicted in Chapter 1. To note here that we did not consider LR-FHSS interferers since they have the same impact on the LoRa-like symbols estimation as Sigfox-like interfering signals, with only an increase of the occurrence of interference on the latter symbols.

Results in Fig. 3.2 correspond to the use of the bandwidths adopted by LoRa and Sigfox ($B = 125$ kHz and $B_{nb} = 100$ Hz). They show that raising the power of interference results in decoding failure of the received signal. The results of Fig. 3.2 allow to quantify the robustness of a LoRa signal against an UNB interference (Sigfox type). Indeed, for a signal to interference ratio (SIR) $\gamma_l = 10 \log_{10}(\frac{P}{P_{nb}})$ of -20 dB we observe a loss of sensitivity of only 1 dB for a BER = 10^{-4} , when the SF = 10 is considered.

Beyond these observations, Fig. 3.2 allow us to validate our interference models, since the results obtained with our Matlab simulators overlap with the results of our models. We illustrate this for the SIR $\gamma_l = -20$ dB.

In order to go further in the analysis of the results, we represent in Fig. 3.3 the impact of UNB interference on the sensitivity of the LoRa-like receiver. We note Γ_l the $\frac{E_b}{N_0}$ sensitivity

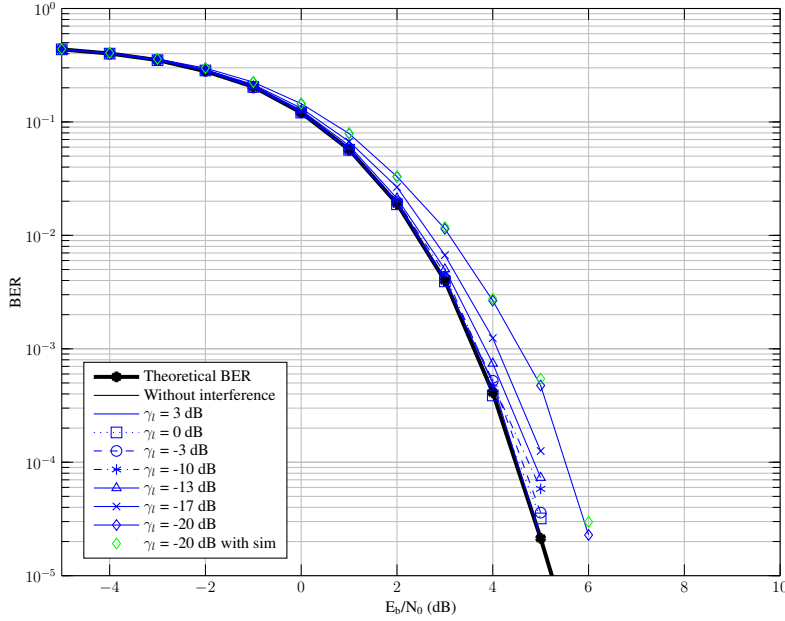


Figure 3.2: Impact of a UNB signal on LoRa-like communication - $SF = 10$, $B = 125$ kHz, $B_{nb} = 100$ Hz and $\gamma_l = 10 \log_{10}(\frac{P}{P_{nb}})$.

threshold, which considered here as the floor value of $\frac{E_b}{N_0}$ to provide a BER of 10^{-4} . Finally, considering that a signal remains UNB up to a bandwidth of 1kHz, we show the impact of increasing the bandwidths of UNB and CSS signals on the receiver sensitivity. For the further results, we consider that $BW = (B_{nb}, B)$ is the bandwidth configuration adopted for each interference scenario.

Fig. 3.3 shows that the decoding quality of the CSS signal is clearly more degraded by increasing B_{nb} . This result is consistent with (3.7) which indicates that the duration of the interference between the CSS and UNB symbols is proportional to B_{nb} . In fact, for an SIR value equal to -10 dB, Γ_l increases by 1.5 dB (resp. 0.6 dB) compared to the reference sensitivity Γ_l^{ref} in the presence of an UNB interfering signal with B_{nb} equal to 1kHz (resp. 100 Hz). In addition, if we consider 10 and 40 UNB interfering signals, with carrier frequencies $f_{p,i}$ uniformly distributed in $[0, B]$ and a bandwidth $B_{nb} = 100$ Hz, the sensitivity threshold increases slightly compared to the case of a single interfering signal with the same bandwidth. Finally, the green curves show that the decoding performance of the CSS signal is clearly enhanced when its bandwidth is increased from 125 kHz to 250 kHz. This result is consistent with (3.7) which indicates that the duration of the interference between the CSS and UNB symbols is inversely proportional to B .

From the former results, we can deduce that the impact of UNB signals of LoRa-like communication is more accentuated by increasing the bandwidth of the interferer (i.e. B_{nb}). Whereas, the impact is less intense if we reduce the bandwidth B of the signal of interest. These results are consistent with (3.7), which prove that the number of samples impacted by

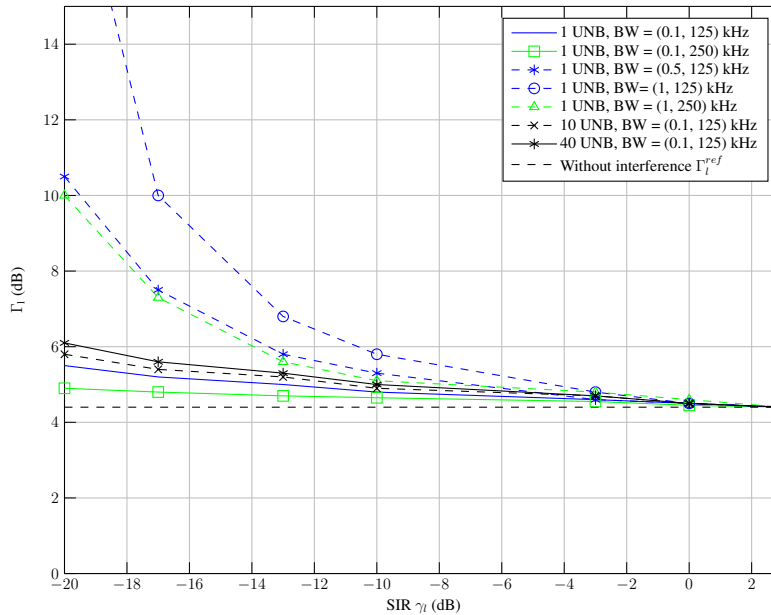


Figure 3.3: Impact of UNB interference on LoRa-like $\frac{E_b}{N_0}$ sensitivity threshold Γ_l as function of $\gamma_l = 10 \log_{10}\left(\frac{P_{wb}}{\sum_{i=1}^{N_{int}} P_{nb,i}}\right) - SF = 10$.

the UNB interfering signal are proportional to B_{nb} and the symbol time of the LoRa-like signal $T = \frac{M}{B}$.

After discussing the resilience of LoRa-like communications to UNB interfering signals, we will focus in the next two sections on their robustness against intra-technology interference (i.e. interference between LoRa-like signals).

3.2 Inter- SF and same- SF interference in LoRa

Apart from the cross-technology interference in the ISM band, a LoRa signal of interest can also experience interference generated by other LoRa nodes. Same-technology interference can be divided in two main categories: the first is interference from other LoRa nodes which use different SF s, which is called inter- SF interference. Different SF s are usually considered to be almost orthogonal. The second, and most severe type of same-technology interference comes from LoRa nodes transmitting with the same SF , and is called same- SF interference. Same-technology interference is directly related to the results of this chapter. The impact of same-technology interference of both types has also received significant attention in the literature [11, 54, 55, 90, 91, 92, 93, 56, 94, 95, 96, 97, 98].

3.2.1 State of the art

The LoRa PHY has been extensively studied on many aspects and several reverse engineering works attempt to reveal more information about this LPWAN technology. One of the most stud-

ied aspect is the issue of same-technology interference, which is the main obstacle to improving the throughput of LoRa-based networks. In the following we provide some details about works, that has addressed this problem.

Authors in [90] examine the scalability of a LoRa network that is limited by same- SF interference. They implemented a network simulator and a simple interference model, where a packet impacted by interference survives if both of the following independent assumptions hold: First, the packet has a value of received signal strength (RSS) that is above the sensitivity threshold for the chosen SF . Second, the received packet has a signal to interference ratio (SIR) greater than 6 dB. The fact that a LoRa packet can survive the impact of a lower-power interfering signal is mentioned in the literature as the capture effect, and has been examined in several papers [54, 55, 56, 57, 11]. Indeed, considering the capture effect in the system model leads to higher values of network throughput compared to the pure ALOHA scenario where any colliding packet is considered lost and needed to be re-transmitted at the expense of the spectral efficiency.

Simulators to evaluate the impact of same and inter SF interference on LoRaWAN performance are implemented in [11, 12, 13, 57, 99, 100]. The authors showed that different SF s are not perfectly orthogonal and such collision can lead to a packet loss if the SIR is lower than a threshold value for each SF configuration. Moreover, for same- SF collisions and by using the capture effect, authors in [11, 12, 13] assumed that the signal of interest is well decoded if its power is 6 dB greater than the total power of the interfering signals.

Authors in [54, 55] have analyzed the impact of a same- SF interfering signal on the decoding performance of the signal of interest by presenting the theoretical models of the interference. This analysis is done at the expense of the interfering signal whose information is lost. This paper does not propose any method to process the interference issue and thus decoding the colliding signals.

The works in [92, 93] measure the impact of same-SF interference using a controllable setup with real-time communications. Using this set-up, they determined the number of end nodes that could be served by one gateway.

Finally, work of [56] measures interfering LoRa packets for multiple SIRs to experimentally evaluate the capture effect in a controllable environment. The results show that a packet under same- SF interfering signal can survive even with a $SIR < 6$ dB, which was also proved in [101]. The measurement results are then used in a simulation model to evaluate the capacity of LoRa networks, showing that it is higher than the capacity of a pure ALOHA network.

3.2.2 Impact of inter-SF interference

SFs in LoRa were widely considered to be orthogonal among themselves [102, 103, 104], however, some recent studies have shown that this is not the case, by experimentally evaluating the effects of inter-SF interference on LoRa-like communications [11, 12, 57, 99, 100].

To model the impact of such interference, we consider that the desired signal is modulated with a reference $SF_{ref} = u \in \{7, \dots, 12\}$, whereas, the interfering signals are modulated with a different spreading factor $SF_{int} = v \in \{7, \dots, 12\} \setminus \{u\}$. Thus the received signal can be expressed as:

$$y(t) = \sqrt{P}s(t) + \sum_{k=1}^{N_{int}} \sqrt{P_k}s_k(t - \tau_k)e^{j(2\pi(\Delta f_k - \Delta f)t)} \quad (3.11)$$

where

- N_{int} is the number of interfering signals,
- Δf (resp. Δf_k) is the CFO of the signal interest (resp. k^{th} interfering signal),
- $s(t)$ (resp. $s_k(t)$) is the signal of interest (resp. k^{th} interfering signal), modulated with SF_{ref} (resp. SF_{int}),
- \sqrt{P} (resp. $\sqrt{P_k}$) is the received power of the signal interest (resp. k^{th} interfering signal),
- τ_k is the time desynchronization between the k^{th} interfering signal and the signal of interest.

To quantify the impact of inter-SF interference on LoRa-like communication, let us introduce the following Signal-to Interference-plus-Noise-Ratio (SINR) threshold matrix, as depicted in Table 3.1. The results of the former table are provided in [11, 12, 13].

Table 3.1: SINR threshold in dB [11].

$SF_{ref} \backslash SF_{int}$	7	8	9	10	11	12
7	-	-16	-18	-19	-19	-20
8	-24	-	-20	-22	-22	-22
9	-27	-27	-	-23	-25	-25
10	-30	-30	-30	-	-26	-28
11	-33	-33	-33	-33	-	-29
12	-36	-36	-36	-36	-36	-

Each element of the latter table corresponds to the co-channel rejection coefficient, which characterizes the SINR margin in dB, that a packet of interest sent with $SF_{ref} = u$ must have in

order to overcome the impact of the interfering signals sent with $SF_{int} = v \in \{7, \dots, 12\} \setminus \{u\}$. Subsequently, if we denote each coefficient by $SINR_{u,v}$, we obtain:

$$SINR_{u,v} = \frac{P}{\sigma_w^2 + \sum_{k \in I_v} P_k} \quad (3.12)$$

with I_v being the set of the indexes of interfering signals that are sent with $SF_{int} = v$.

It can be also noticed that the rejection coefficients are very low for inter- SF interference, especially for the highest SF s. Hence, the former SF s are usually assigned to distant nodes for the noise sensitivity also permits to overcome the impact of closer devices which are likely to be received with a higher power level.

After modeling and quantifying the impact of inter- SF interference using some results from the literature, we will discuss in the next paragraph the most serious problems facing LoRa-based networks, which is same- SF interference.

3.2.3 Impact of same- SF interference

The main limiting factor for the scalability of massive LoRa networks is the same-technology interference, especially the same- SF destructive collisions. As presented in [105], receiving simultaneously two or more signals with the same SF leads to a loss of orthogonality and may cause the loss of all packets. However, the majority of the works have implemented system-level simulators using an abstraction of the PHY layer. In most of the cases interference and noise are treated independently, and the threshold for the capture effect is heuristically chosen at $SIR = 6$ dB. Furthermore, the latter works do not propose a solution to deal with this destructive collision. In this paragraph, we model the impact of same- SF interference and we provide some solutions proposed in the literature to deal with this issue. Then, in sections 3.3 and 3.4, we present our approaches allowing to overcome the impact of the former problem in uplink and downlink scenarios.

3.2.3.1 Problem modeling

In this paragraph, we analyze the case of a gateway trying to decode the signal of interest simultaneously received over the same channel with an interfering signal having the same SF . As mentioned in Chapter 2, this scenario becomes particularly relevant in future LoRa deployments with a high density of end nodes, especially with LEO satellite communications, due to the uncoordinated ALOHA-based random channel access of LoRaWAN. As we showed in the previous paragraph that inter- SF interference can cause the loss of the signal of interest at a very low SIR for all the SF s. Hence, same- SF interference has a dominant impact on the throughput of LoRa based-networks. To illustrate the principle, we consider in the following

two signals in interference.

If we note $s(t)$ (resp. $s_I(t)$) the signal of interest (resp. the interfering signal) defined as in (2.3), we obtain the following received signal synchronized on $s(t)$:

$$y(t) = \sqrt{P}s(t) + \sqrt{P_I}s_I(t - \tau_I)e^{j(2\pi(\Delta f_I - \Delta f)t)} + w(t) \quad (3.13)$$

where

- Δf (resp. Δf_I) is the CFO of the signal interest (resp. interfering signal),
- \sqrt{P} (resp. $\sqrt{P_I}$) is the received power of the signal interest (resp. interfering signal),
- τ_I is the time desynchronization between the two received signals.

It should be noted here that the gateway is assumed to be perfectly synchronized on the signal of interest (i.e. CFO and STO are compensated).

At the gateway, we focus on the demodulation of the p^{th} transmitted symbol of the signal of interest. The dechirped signal, sampled at $T_s = \frac{1}{B}$ and used to demodulate the later symbol, can be written as:

$$\begin{aligned} z(n, p) = & \sqrt{P}e^{j2\pi n \frac{S_p}{M}} + \sqrt{P_I}e^{j2\pi n \frac{\bar{S}_p^I}{M}} \mathbb{1}_{[0, L_\tau - 1]}(n) \\ & + \sqrt{P_I}e^{j2\pi n \frac{\bar{S}_p^I}{M}} \mathbb{1}_{[L_\tau, M - 1]}(n) + \tilde{w}(n) \end{aligned} \quad (3.14)$$

Where S_p is the p^{th} transmitted symbol by the node of interest and with

$$\bar{S}_p^I = (S_p^I - L_\tau + \delta f) \quad \text{mod } M \quad (3.15)$$

and

$$\bar{S}_{p-1}^I = (S_{p-1}^I - L_\tau + \delta f) \quad \text{mod } M \quad (3.16)$$

with $L_\tau = \lfloor \frac{\tau_I}{T_s} \rfloor$ and $\delta f = \Delta f_I - \Delta f$.

As explained in the previous chapter, the symbol S_p is retrieved by searching the *argmax* of the FFT of the de-chirped signal (3.14).

In Fig. 3.4, we represent the result of the FFT processing of (3.14). It can be easily seen that the interfering signal contributes by two cardinal sines, which impact the detection of peak of the synchronized signal (i.e. signal of interest).

In the literature, several works [54, 106, 107, 108] have conducted detailed studies on the impact of the same- SF interference on the symbol estimation of the signal of interest, by providing the theoretical expressions of such interference. For instance, we refer to Fig. 3.5 from

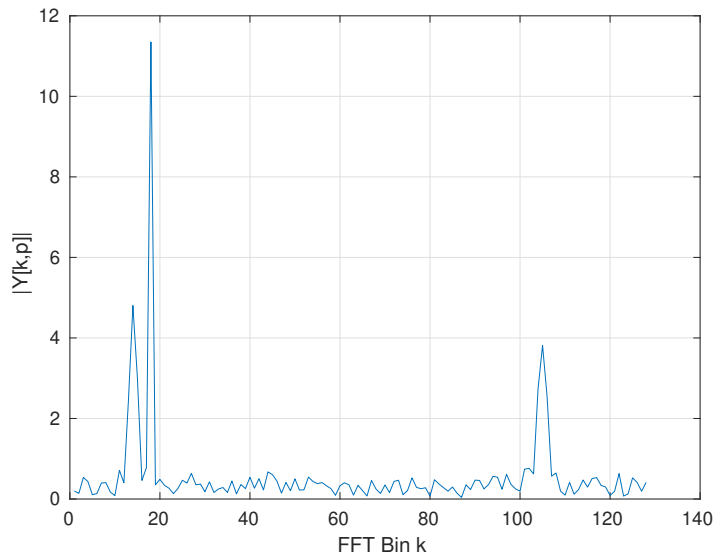


Figure 3.4: Result of the FFT in the presence of same- SF interference with $SIR = 3$ dB, $SF = 7$ and $L_\tau = 55$.

[108], which provide the evolution of the SNR_{th} , when considering a target frame error rate (FER) of 10^{-1} , as function of the SIR.

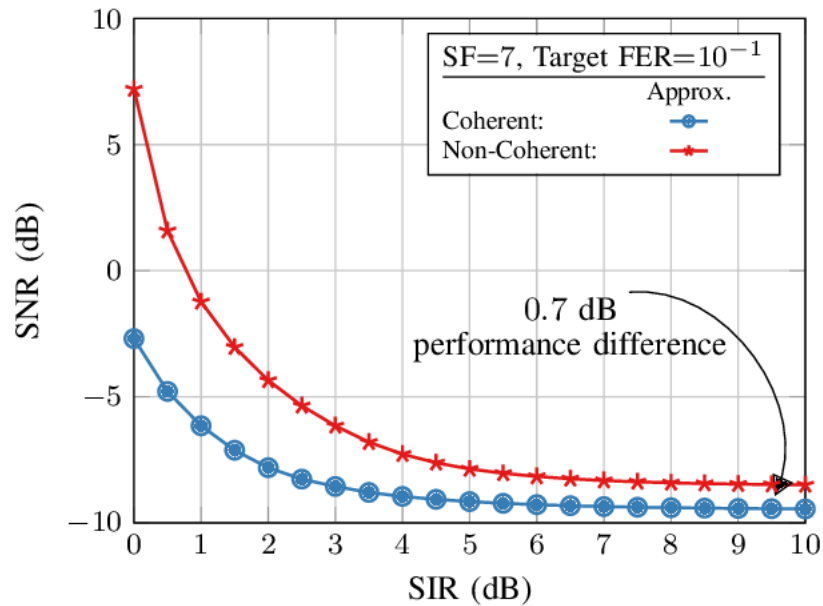


Figure 3.5: SNR threshold for a target FER of 10^{-1} as a function of the SIR for a packet length of $N_{pay} = 20$ LoRa symbols for $SF = 7$ for coherent and non-coherent receiver [108].

We notice, for a non-coherent receiver, that the target SNR is slightly affected for a SIR greater than 6 dB, which is considered in many works as the minimum SIR giving the required QoS. Moreover, we can easily notice that the use of a coherent demodulation allows to enhance

the decoding performance under same- SF interference. In fact, for the higher SIR the gain is only 0.7 dB. Whereas, for low SIR (i.e. close to zero) the benefit can reach 10 dB. Hence, coherent demodulation can be considered as a solution to reduce the impact of the former issue. In the next paragraph, we provide some strategies to deal with this problem.

3.2.3.2 Strategies to deal with same- SF interference

Dealing with packet collisions in communication systems with random access to the channel, such as LoRa-based networks, is a very challenging task. To conquer this challenge, preventive or palliative solutions could be deployed.

- **Preventive approaches**

Among preventive approaches, we can mention using the frequency diversity of random-access channel (RACH) in LoRaWAN [50]. In such configuration, if the nodes do not receive an acknowledgment, due to an out of range communication or the presence of interfering signals, they wait for random period before transmitting again at the expense of the spectral efficiency. In the same context, authors in [109] propose to reduce the occurrence of destructive collisions in LoRaWAN by using redundant gateways.

- **Palliative approaches**

In the literature, few works have proposed solutions to deal with same- SF interference rather than avoiding it. Indeed, some works prove that it is possible to reduce the impact of the interfering signal. For instance, authors in [108] demonstrate that the use of coherent LoRa symbol detection would improve the decoding performance of the signal of interest compared to the non-coherent method. Furthermore, authors in [110] and [111] proposed a modification of the CSS modulation referred to respectively as Symmetric CSS (SCSS) and Asymmetry CSS (ACSS). These two modulations allowed to enhance the decoding performance of the signal of interest in same- SF interference scenario. However, The latter approach are done at the expense of the interfering signal whose information is lost. Thus, to avoid this issue, some works propose to decode the superposed signals using the successive interference cancellation (SIC) approach. For instance, authors in [101] studied the capture effect and proposed to use SIC algorithm to decode the superposed signals. Nevertheless, this analysis does not provide any explanation about how the interference cancellation and the synchronization are performed. They presented the throughput of the proposed system using an abstraction of the physical layer since they assumed that the SIC is well performed if the SIR is greater than a threshold value.

Moreover, a novel approach to decode non-orthogonal LoRa signals using the specific structure of the chirps is presented in [102]. However, their proposed algorithms could decode only

two superposed signals and require the receiver to be perfectly synchronized or slightly desynchronized which is unrealistic in a random access scenario as adopted by LoRa-based networks. In addition, using the spectrogram of the chirps to decode the superposed signals is not very efficient since it requires a good SNR to identify them. And basically the problems occur when we are closed to the receiver sensitivity.

In the same context, authors in [58] deployed a SIC algorithm to enhance the throughput of LoRa-based network in LEO satellite communication scenario. Yet, this study also did not formalize the SIC algorithm and the strategy used to decode superposed signals. To that end, authors in [112] have gave the mathematical models before introduced the results of SIC by evaluating the decoding performance of the superposed signals. However, the strongest signal in each iteration of their SIC algorithm is based on the correlation with the preamble, which has a high computational complexity. Moreover, they used this correlation to determine the beginning start of the received packets, which is impossible in the presence of CFO. The same authors provided in [113] a multi-user detection (MUD) scheme to decode superposed LoRa-like signals, without performing the SIC, in a downlink communication case. To that end, they supposed that the superposed signals are transmitted in a synchronized way by the gateway. In addition, they considered a power allocation schemes to minimize error probabilities and increase fairness between users having good or bad channels

In the next two sections, we propose our approach to decode superposed LoRa-like signals in uplink and downlink scenarios. To note that we are the first proposing a detailed study on how deploying the SIC to decode superposed LoRa-like signals, by providing our approaches and models for the detection, time/frequency synchronization, decoding and cancellation of the strongest signal in each iteration of our algorithm.

3.3 Proposed uplink approach to process the multiple Reception of non-orthogonal LoRa-like signals

In this section, we deal with an uplink communication case where several LoRa-like signals are simultaneously received over the same channel and with the same SF at the gateway. Due to the random access protocols adopted by LoRa-based networks and the deployment of low-cost crystal oscillators which have an inherent mismatch with their nominal frequency, all the received signals are randomly desynchronized in time and suffer from carrier frequency offsets. The goal of this chapter is to design an efficient receiver capable to decode superposed LoRa-like signals in such configuration. Our approach is based on the SIC algorithm which is relevant because the interference can be removed efficiently based on the symbol estimation principle. This processing would reduce the energy consumption of the nodes and enhance their spec-

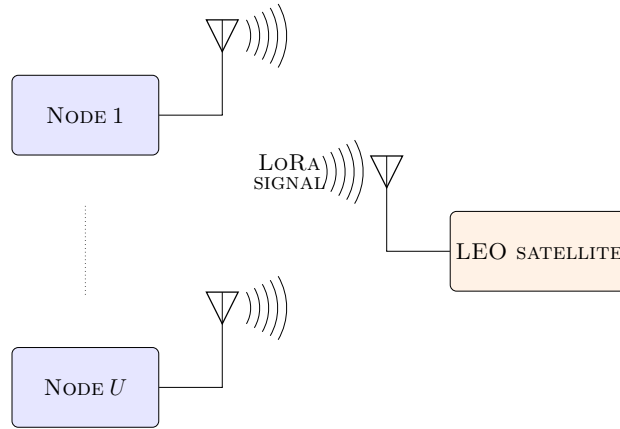


Figure 3.6: Test-bed for U LoRa transmissions simultaneously received by a LEO satellite.

tral efficiency since it decreases the number of re-transmitted packets. Finally, to evaluate the performance of our receiver, we perform simulation using LoRa-like signals synthesized with Matlab before considering real LoRa deployments.

3.3.1 System model

We consider an uplink communication system where several LoRa-like signals are supposed to be simultaneously received on the same channel and with the same SF . Indeed, as depicted in Fig. 3.6, those signals come from IoT LoRa nodes transmitting data to a LEO satellite, which is considered as a gateway that can demodulate the intended signals or forward them to a ground station for this purpose. As presented in [105], receiving simultaneously two or more signals with the same SF leads to a loss of orthogonality and may cause the loss of all packets.

3.3.1.1 Model of transmitted signals

As we have already mentioned in the previous chapter, the signal transmitted by each LoRa node is started by the aforementioned preamble, the sync word and the SFD.

Based on the LoRa frame structure as depicted in Fig. 2.5, a realistic complex envelope of the signal transmitted by the i^{th} node can be written as:

$$x_i(t) = x_{pre}(t)\mathbb{1}_{[0, T_p]}(t) + s_i(t - T_p)\mathbb{1}_{[T_p, T_p + N_s^i \times T]}(t) \quad (3.17)$$

where

- $x_{pre}(t)$ is the complex envelop of the above-mentioned preamble with a duration equals to T_p ,

- $s_i(t)$ is the complex envelop of the N_s^i payload modulated chirps transmitted by the i^{th} node

3.3.1.2 Model of received signals

In this paragraph, we detail the mathematical models and the demodulation principle of the received signals at a LoRa gateway. Due to the complete lack of synchronization between the gateway and the nodes, the continuous-time version of the received signal, when several LoRa-like frames with the same SF are superposed, can be written as:

$$y(t) = \sum_{i=1}^U \sqrt{P_i} x_i(t - \Delta t_i) e^{j(2\pi(\Delta f_i + c_d^i t)t + \theta_i)} + w(t) \quad (3.18)$$

where P_i , θ_i , Δt_i , Δf_i and c_d^i are respectively the power, the initial phase, the time desynchronization, the CFO and the DR of the i^{th} received signal.

To detect, synchronize and decode LoRa-like signals, the gateway has to be in a listening status. To this end, the received signals are sampled and multiplied by a train of down-chirp signals. Indeed, as depicted in Fig. 3.7, the multiplication by the de-chirping sequence is performed, not necessarily in a synchronized mode at first since the beginning instant of each packet is not known in advance by the receiver. The former de-chirping sequence, sampled at T_s , can be expressed as:

$$d(n) = \sum_{p \in \mathbb{Z}} \overline{x_{ref}(n + (p-1)M)} \mathbb{1}_{\llbracket (p-1)M, pM-1 \rrbracket}(n) \quad (3.19)$$

In the previous chapter, we discussed several practical methods to perform accurate time and frequency synchronizations of the received signal.

As the processing of LoRa-like signals at the gateway is done after the Analog to Digital Converter (ADC), the discrete-time version of the received signal sampled at T_s is given by:

$$y(n) = \sum_{i=1}^U \sqrt{P_i} x_i(n - \Delta n_i) e^{j(2\pi(\Delta f_i + c_d^i n T_s)n T_s + \theta_i)} + w(n) \quad (3.20)$$

The discrete time shift Δn_i between the beginning of the de-chirping sequence and each superposed LoRa signal is expressed as: $\Delta n_i = \frac{\Delta t_i}{T_s} = K_i M + \tau_i$ with $K_i \in \mathbb{N}$ and τ_i denoting the relative time offset between the i^{th} signal with the de-chirping sequence and following the uniform distribution $\mathcal{U}[0, M)$. As we have discussed in the previous chapter, τ_i can not be constrained to an integer value, since supposing that the de-chirping sequence is sample-aligned with the received signals is not realistic. Therefore, this time-offset is given by: $\tau_i = L_i + \lambda_i$, with

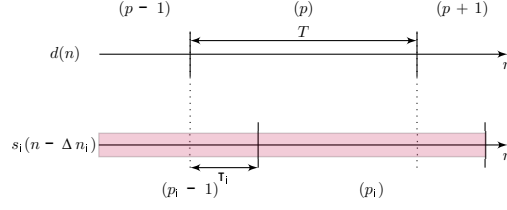


Figure 3.7: LoRa-Like symbol detection principle.

$L_i = \lfloor \tau_i \rfloor$ and $\lambda_i \in [0, 1)$. Moreover, the CFO of the i^{th} signal can be written as $\Delta f_i = C_i + \nu_i$, with $C_i = \lfloor \Delta f_i T \rfloor$ and $\nu_i \in [-0.5, 0.5)$

Based on the principle of the LoRa-Like symbol detection detailed in [105, 55, 114] and on Fig. 3.7, the signal obtained after the FFT, which corresponds to the processing of p^{th} T -long section of the de-chirping sequence is equal to:

$$Y(k, p) = \frac{1}{\sqrt{M}} \sum_{n=0}^{M-1} \underbrace{(y(n, p)d(n, p))}_{z(n, p)} e^{-j2\pi \frac{nk}{M}} \quad (3.21)$$

where $y(n, p) = y(n)$ and $d(n, p) = d(n) \forall n \in \llbracket (p-1)M, pM-1 \rrbracket$. Thus based on [105, 52], Fig. 3.7 and after some calculations we obtain:

$$\begin{aligned} z(n, p) &= \sum_{i=1}^{U_p} z_{\tau_i}(n, p) + w(n) = \sum_{i=1}^{U_p} \left(\sqrt{P_i} e^{j(2\pi n \frac{\bar{S}_{p_i}^i - 1}{M} + \phi^{p_i - 1})} \mathbb{1}_{\llbracket 0, L_i \rrbracket}(n) \right. \\ &\quad \left. + \sqrt{P_i} e^{j(2\pi n \frac{\bar{S}_{p_i}^i}{M} + \phi^{p_i})} \mathbb{1}_{\llbracket L_{i+1}, M-1 \rrbracket}(n) \right) + w(n) \end{aligned} \quad (3.22)$$

where

- $U_p \in \{1, \dots, U\}$ is the number of received signals in the p^{th} T -long section of the de-chirping sequence,
- $\phi^{p_i}, p_i \in \{1, \dots, N_t + N_s^i\}$, is the initial phase of the i^{th} received signal in its p_i^{th} T -long section, with $N_t = \frac{T_p}{T}$,
- $\bar{S}_{p_i}^i, p_i \in \{1, \dots, N_t + N_s^i\}$, is the frequency of the detected peak of latter signal in a non synchronized mode. The relation between $\bar{S}_{p_i}^i$ and the symbol initially transmitted is expressed as:

$$\bar{S}_{p_i}^i = S_{p_i}^i - \tau_i + \Delta f_i T + \frac{c_d^i p}{2} T^2 \pmod{M} \quad (3.23)$$

To note we considered the same modeling of the DR as in (2.21), where we assumed that it is constant in each T -long sequence.

Based on the structure of i^{th} de-chirped signal $\forall i \in \{1, \dots, U\}$, we can observe that the FFT of a non synchronized signal gives two cardinal sines. Here, we notice that the maximum

number of peaks that could be detected is $2 \times U_p$ depending on the positions of the latter peaks (probability of 2 superposed peaks) and the noise level of each signal. Therefore, in a non-synchronized mode, an accurate decoding of these signals is impossible.

In the next section, we propose a novel approach to detect, synchronize and decode the maximum number of non-orthogonal signals simultaneously received.

3.3.2 Proposed algorithms to process the reception of multiple non-orthogonal LoRa-like signals

In this section, we propose to design an enhanced receiver able to synchronize and decode simultaneously received non-orthogonal LoRa-like signals. Our approach consists in processing LoRa signals in a given time window. Indeed, the receiver sets a constant block duration T_B and tries to iteratively decode the maximum number of signals received along this duration. The principle consists in:

- detecting the received signals and identifying the strongest one,
- performing the time/frequency synchronization of the strongest signal,
- decoding its information,
- reproducing its complex envelope and removing it from the received signal (SIC algorithm).

The latter operations are repeated until there is no detected LoRa-like signal left. We point out that each two consecutive blocks are overlapped by at least a maximum packet duration¹ to ensure the processing of all the received signals information. To note also that we did not consider the impact of the DR in proposed algorithm (i.e. $c_d^i = 0, \forall i \in \{1, \dots, U\}$). However, we proved in the previous chapter that we are able to measure and compensate the latter frequency drift. As a consequence, we did not consider the use of DCSS.

3.3.2.1 Detection of the strongest signal

The detection of the presence of LoRa-like signals is performed by a gateway in a listening mode. This is done by continuously de-chirping the sampled received signals. After that, a FFT is processed in each T -long section as presented in (3.21).

Nevertheless, given that all the symbols of LoRa preamble are equal to zero. Thus, only one peak is detected even in a non-synchronized mode (time and frequency desynchronizations)

¹As an example, in LoRaWAN, the maximum packet duration is known for each SF .

since the contribution of two consecutive zero symbols would be superposed in same FFT bin as depicted in Fig. 3.8 for the strongest signal. Thereby, given that $\forall p_s \in \{1, \dots, N_p\}, S_{p_s}^s = 0$ and by using (3.23), a nearly accurate estimation of the total shift of the main peak $\hat{\tau}'_s = -\tau_s + \Delta f_s T$ can be easily performed.

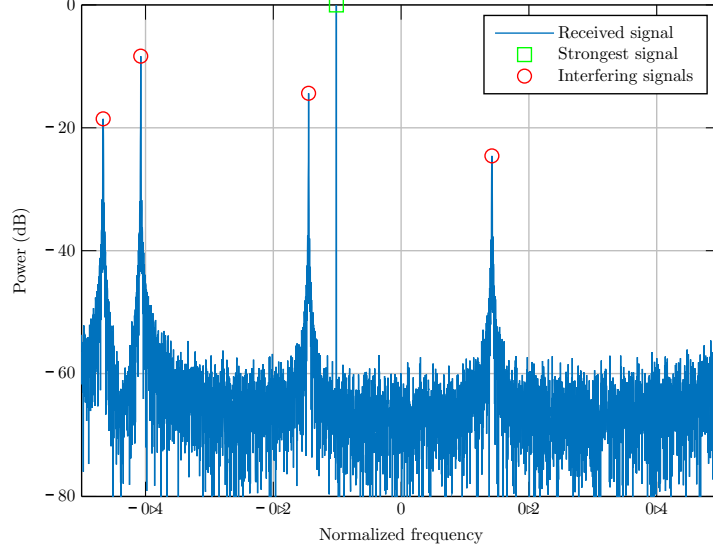


Figure 3.8: Result of the FFT processing when the preamble of the strongest signal is superimposed with two interfering signals ($U_p = 3$).

Given the structure of LoRa packet preamble, averaging the module squared of the FFTs over each N_p T -long sections would increase the certainty of preamble detection. If we note $T(k, p)$, $k \in \llbracket 0, M - 1 \rrbracket$, $p \in \{1, \dots, N_B\}$ and $N_B = \lfloor \frac{T_B}{T} \rfloor$, the averaging function, we have:

$$T(k, p) = \sum_{j=p}^{p+N_p-1} \left| \frac{Y(k, j)}{\sigma_w} \right|^2 \quad (3.24)$$

It should be noted that the estimation of the AWGN variance σ_w^2 is done on silent periods when no signal is received.

To coarsely estimate the index \hat{K}_s of the T -long section that corresponds to the beginning of the strongest signal preamble, we compute the function $M(p)$, as presented in Fig. 3.9 when three signals are simultaneously received. This function represents the maximum value of $T(k, p)$, $\forall p \in \{1, \dots, N_B\}$.

$$M(p) = \max_k (T(k, p)). \quad (3.25)$$

Then, if we note \hat{K}_s an estimation of K_s we have:

$$\hat{K}_s = \underset{p}{\operatorname{argmax}} (M(p)). \quad (3.26)$$

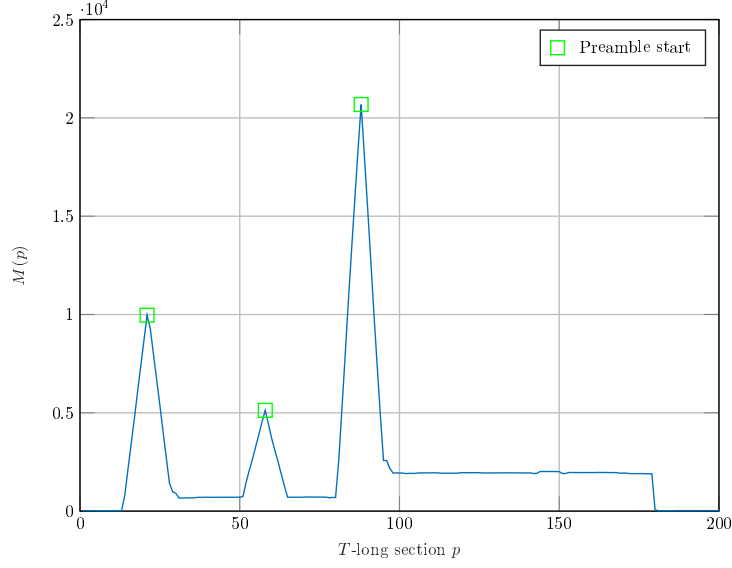


Figure 3.9: Preamble detection process ($U = 3$).

We notice that, in each iteration of our algorithm, the identification of the maximum of $M(p)$ requires the definition of a threshold value to detect the existence of LoRa-like signals in the data block. This value is set using a classical hypothesis test on $T(k, p)$ according to the noise level.

Giving that the FFT of the noise in p^{th} T -long section $W(k, p)$, $k \in \llbracket 0, M - 1 \rrbracket$, follows the Normal distribution $\mathcal{N}_{\mathbb{C}}(0, \sigma_w^2)$, thus, it is easy to demonstrate that $\sum_{j=p}^{p+N_p-1} \left| \frac{W(k, j)}{\sigma_w} \right|^2$ follows the chi-squared distribution $\chi^2(\cdot; N_p)$ with N_p is the degree of freedom.

If we note P_{fa} the probability of the false alarm based on the following binary hypothesis tests

- $\mathcal{H}_0: \{U_j = 0, \forall j \in \{p, \dots, p + N_p\}\}$,
- $\mathcal{H}_1: \{\exists j \in \{p, \dots, p + N_p\}, U_j \neq 0\}$,

we have:

$$\begin{aligned}
 P_{fa} &= P[\mathcal{H}_1/\mathcal{H}_0] \\
 &= P[T(k, p) > Th/T(k, p) \sim \chi^2(\cdot; N_p)] \\
 &= 1 - P[T(k, p) < Th/T(k, p) \sim \chi^2(\cdot; N_p)] \\
 &= 1 - F_{\chi^2}(Th; N_p)
 \end{aligned} \tag{3.27}$$

where $F_{\chi^2}(\cdot; N_p)$ is the cumulative density function of the chi-squared distribution with N_p degree of freedom.

Thus, the threshold Th could be expressed as:

$$Th = F_{\chi^2}^{-1}(1 - P_{fa}; N_p) \tag{3.28}$$

Therefore, if $T(k, p) < Th, \forall p \in \{1, \dots, N_B\}$, no LoRa-like signal is detected in the considered block.

3.3.2.2 Time and frequency synchronization of the strongest signal

The previous synchronization procedure has enabled the detection of the strongest received signal and the estimation of K_s and τ'_s . However, due to the random distribution of the total shift τ'_s (caused by τ_s and Δf_s), we will have a significant uncertainty on the estimation of K_s . Furthermore, as explained in the previous chapter, the τ_s and Δf_s are jointly performed. As a consequence, we propose a fine frame synchronization procedure in order to reduce the latter uncertainty on K_s and to accurately estimate τ_s and Δf_s .

Here, we suggest an optimized method based on the SFD framing. It is simply needed to compensate the total shift $\hat{\tau}'_s$ and apply an up-chirp sequence to the T -long sections where the down-chirp symbols of the SFD are expected. The two highest successive FFTs maxima in the same FFT bin indicate the beginning of the down-chirps. Hence, an accurate estimation of K_s can be performed. After that the receiver estimates the fractional CFO using the preamble up chirps via the Schmidl-Cox estimator as depicted in (2.28). Once the latter offset is compensated for the strongest signal, the receiver measures the fractional part of τ_s using the interpolation method as described in 2.5.2.5. Finally, after compensating the fractional STO, the integer parts of τ_s and Δf_s are jointly estimated via the system of two equations as depicted in (2.35) and compensated as shown in (2.38).

3.3.2.3 Decoding the strongest signal

Once the receiver is synchronized to the beginning of the frame of the signal having the highest received power, a synchronized de-chirping process is applied to it. Consequently, a FFT is performed for each T -long section of the latter frame. We assume here that the time and frequency synchronizations are perfectly performed on the strongest signal.

If we note $z_s(n, p_s)$ the de-chirped received signal synchronized on the former signal, we have:

$$z_s(n, p_s) = \sqrt{P_s} e^{j\left(2\pi n \frac{S_{p_s}^s}{M} + \phi^{p_s}\right)} + \sum_{i=1}^{U_{p_s}-1} z_{\tau_i^s}(n, p_s) + w(n) \quad (3.29)$$

with $n \in \llbracket \Delta n_s + p_s M, \Delta n_s + (p_s + 1)M - 1 \rrbracket$ and τ_i^s being the time offset between the synchronized signal and the i^{th} interfering signal. Using (3.21) and some calculation, the FFT of $z_s(n, p_s)$ can be expressed as:

$$Y^s(k, p_s) = \sqrt{P_s M} \delta(k - S_{p_s}^s) + \sum_{i=1}^{U_{p_s}-1} Y_i(k, p_s) + W(k) \quad (3.30)$$

where $Y_i[k, p_s]$ is the FFT of i^{th} signal interfering the decision of the p_s^{th} symbol. Hence, the estimation of the p_s^{th} transmitted symbol is obtained as:

$$\hat{S}_{p_s}^s = \underset{k}{argmax}(|Y^s[k, p_s]|) \quad (3.31)$$

3.3.2.4 Strongest signal cancellation

Once the receiver is synchronized on the strongest signal, it estimates the frequency as presented in (3.31), the magnitude and the phase of the main peak in each T -long section of the later signal. Then the symbols are decoded and the signal associated to each estimated symbol could be reproduced and subtracted from the received signal.

If we note $\hat{z}_s(n, p_s)$ the reconstruction of the synchronized signal, in the p_s^{th} T -long section, synthesized by the estimation of its frequency $\hat{S}_{p_s}^s$, magnitude $\sqrt{\hat{P}_s^{p_s}}$ and initial phase $\hat{\phi}^{p_s}$, we have:

$$z(n, p_s) = z(n, p_s) - \hat{z}_s(n, p_s) \quad (3.32)$$

where $\hat{z}_s(n, p_s)$ is expressed as:

$$\hat{z}_s(n, p_s) = \sqrt{\hat{P}_s^{p_s}} e^{j\left(2\pi n \frac{\hat{S}_s^s}{M} + \hat{\phi}^{p_s}\right)} \quad (3.33)$$

To enhance the performance of our SIC-based algorithm, it is important to deal with some critical cases that can occur in such interference scenario. To this end, we deal in the next paragraph with the issue of superposed peaks in the FFTs.

3.3.2.5 Processing of superimposed peaks

Dealing with simultaneously received LoRa-like signals with the same SF causes some critical cases that should be studied to avoid the degradation of the decoding performance. As presented in (3.29), after the FFT processing, the synchronized signal contributes by one Dirac at the symbol to estimate, but the other existent signals contribute by two cardinal sines each. As a result, there is a non-null probability that one of these peaks is located at the same FFT bin with the Dirac of the synchronized signal. In this case, after estimating the frequency, magnitude and phase of the main peak, the latter is removed and then the contribution of the other existent signals in the same FFT bin is also reduced.

To address this issue, we propose to compare the magnitude of the current FFT main peak with a mean value, denoted $\sqrt{\bar{P}_s}$ and computed from the main peaks in all the T -long sections of the signal of interest. If this current magnitude is considerably greater than the mean value,

two or more superposed peaks are assumed to be detected. In this case, an hypothesis test is done by referring to the distribution of the demodulation metric $|Y_s(k, p_s)|$. Thus, if we suppose that there are no interfering signals in the p_s^{th} T -long section and by using the basic properties of the complex normal distribution, we have:

$$|Y_s(k, p_s)| \sim \begin{cases} \mathcal{R}_i(\sqrt{P_s M}, \sigma_w) & \text{for } k = S_{p_s}^s \\ \mathcal{R}_i(0, \sigma_w) & \text{else} \end{cases} \quad (3.34)$$

Where $\mathcal{R}_i(u, v)$ is the Rician distribution with u and v are the location and the scale parameters.

In this case, we define the hypothesis of our test as:

- \mathcal{H}_0 : one peak exists at the FFT bin of the symbol to be decoded.
- \mathcal{H}_1 : two or more peaks are superposed at the FFT bin of the symbol to be decoded.

Using the same definition of the probability of false alarm P'_{fa} as we detailed in 3.3.2.1, we can easily deduce the value of the threshold allowing the detection of two or more peaks at the FFT bin of the symbol to be decoded:

$$Th' = F_{\mathcal{R}_i}^{-1}(1 - P'_{fa}; \sqrt{P_s M}, \sigma_w) \quad (3.35)$$

Once the receiver detects the presence of two or more peaks at the FFT bin of the current symbol of the synchronized signal, the magnitude and the phase of the reconstructed signal in (3.33) will be $\sqrt{\bar{P}_s}$ and $\bar{\phi}$, where $\bar{\phi}$ is the mean phase computed from the initial phases in all the T -long sections. It should be noted here that LoRa modulation is a memoryless continuous phase modulation [105]. Thus, the initial phases are equal in all the T -long sections. Thereby, this operation allows to maintain the contribution of the signals other than the strongest one in the same FFT bin.

Finally, as depicted in Fig. 3.10, which summarizes the adopted approach to design our receiver, the algorithms presented in sections 3.3.2.2, 3.3.2.3, 3.3.2.4 and 3.3.2.5 are repeated until no LoRa-like signal is detected in the considered block. Reader can find more details about our algorithm in the pseudo-code in the Algorithm 2.

Algorithm 2: Decoding superposed LoRa-like signals

Input: $y(n)$, SF , B , N_B

$M \leftarrow 2^{SF}$.

$z(n, p) \leftarrow (3.44)$, $n \in \llbracket pM, (p+1)M - 1 \rrbracket$ and $p \in \{1, \dots, N_B\}$ (dechirping operation).

$Y(k, p) \leftarrow (3.21)$, $k \in \llbracket 0, M - 1 \rrbracket$ (FFT).

$T(k, p) \leftarrow (3.24)$ (averaging function).

$M(p) \leftarrow \max_k(T(k, p))$.

$Th \leftarrow (3.28)$ (noise threshold).

while $\exists p \in \{1, \dots, N_B\}$, $M(p) > Th$ **do**

$\hat{K}_s \leftarrow \underset{p}{\operatorname{argmax}}(M(p))$.

$\hat{\tau}_s, \hat{\Delta}f_s \leftarrow$ fine synchronization.

$\Delta n_s \leftarrow \hat{K}_s M + \hat{\tau}_s$.

for $p_s \leftarrow 1$ to N_{symbols} **do**

$z_s(n, p_s) \leftarrow (3.29)$, $n \in \llbracket \Delta n_s + p_s M, \Delta n_s + (p_s + 1)M - 1 \rrbracket$.

$Y^s(k, p_s) \leftarrow FFT(z_s(n, p_s))$.

$\hat{m}_s(p_s) \leftarrow \underset{k}{\operatorname{argmax}}(|Y^s(k, p_s)|)$ (estimated symbol).

$\sqrt{\hat{P}_s^{p_s}} \leftarrow \max_k(|Y^s(k, p_s)|)$ (estimated magnitude).

$\hat{\phi}^{p_s} \leftarrow \operatorname{arg}(|Y^s(\hat{m}_s(p_s), p_s)|)$ (estimated phase).

$Th' \leftarrow (3.35)$ (threshold to detect superposed signals).

if $\sqrt{\hat{P}_s^{p_s}} > Th'$ **then**

$\hat{A}_r \leftarrow \underset{p_s}{\operatorname{mean}}(\sqrt{\hat{P}_s^{p_s}})$.

$\hat{\phi}_r \leftarrow \underset{p_s}{\operatorname{mean}}(\hat{\phi}^{p_s})$

else

$\hat{A}_r \leftarrow \sqrt{\hat{P}_s^{p_s}}$.

$\hat{\phi}_r \leftarrow \hat{\phi}^{p_s}$.

end

$\hat{z}_s(n, p_s) \leftarrow \hat{A}_r e^{j\left(2\pi n \frac{\hat{\phi}_r}{M} + \hat{\phi}_r\right)}$ (reconstruction of the strongest signal).

$z(n, p_s) \leftarrow z(n, p_s) - \hat{z}_s(n, p_s)$ (SIC).

end

$T(k, p) \leftarrow (3.24)$.

$M(p) \leftarrow \max_k(T(k, p))$.

end

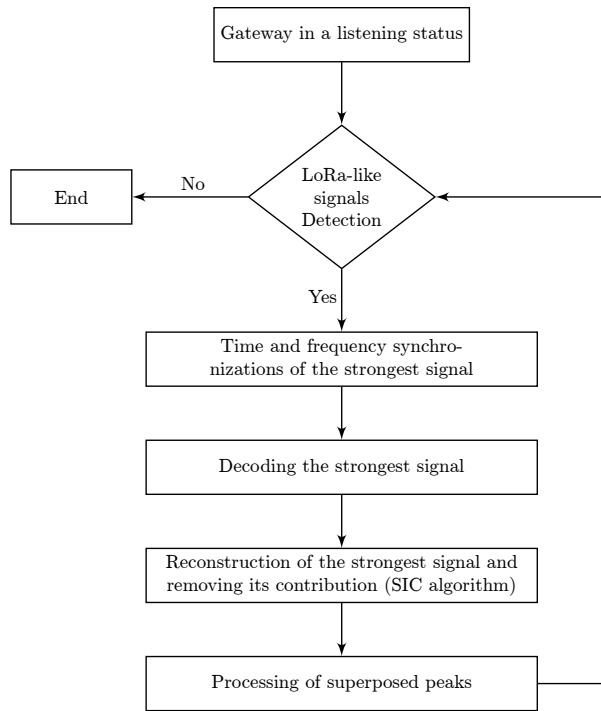


Figure 3.10: Adopted algorithm.

3.3.3 Results and Discussions

In this section, we aim to evaluate the performance of our receiver to synchronize and decode simultaneously received LoRa-like signals with the same SF . To this end, we propose to:

- perform Monte Carlo based simulations using synthesized LoRa-like signals,
- use own-made LoRa nodes and gateways to validate our results with real LoRa deployments.

3.3.3.1 Simulation results on synthesized signals

• Considered scenario

The considered scenario consists in simultaneously receiving U LoRa-like signals at random arrival instants using the parameters in Table 3.2. The packets are generated using our Matlab simulator and have the structure as presented in Fig. 2.5. For the sake of simplicity, we assumed that the simulated receiver is aware of the packet and the preamble lengths.

In the following, we define the power ratio between each two received signals:

$$(PR_{i,j})_{dB} = 10 \log_{10} \left(\frac{P_i}{P_j} \right), \quad i, j \in \{1, \dots, U\} \quad (3.36)$$

Table 3.2: Simulation parameters

Bandwidth (kHz)	125
Spreading Factor	$\{12; 9; 7\}$
Frame length	$80 \times T$
Block length T_B	$200 \times T$
Preamble length N_p	8
Number of superposed signals U	$\{2; 3; 4\}$
Number of Monte Carlo iterations	10000

When sorting the received powers by decreasing order, we consider that the power ratio (dB) between each two consecutive signals as being constant and equals to PR .

Furthermore, the frequency shifts $\Delta f_i, \forall i \in \{1, \dots, U\}$ are supposed uniformly distributed in $[-\Delta f_{max}, \Delta f_{max}]$. The highest frequency offset Δf_{max} is equal to $25\% \times f_{s_{min}}^2$.

- **Start of frame detection**

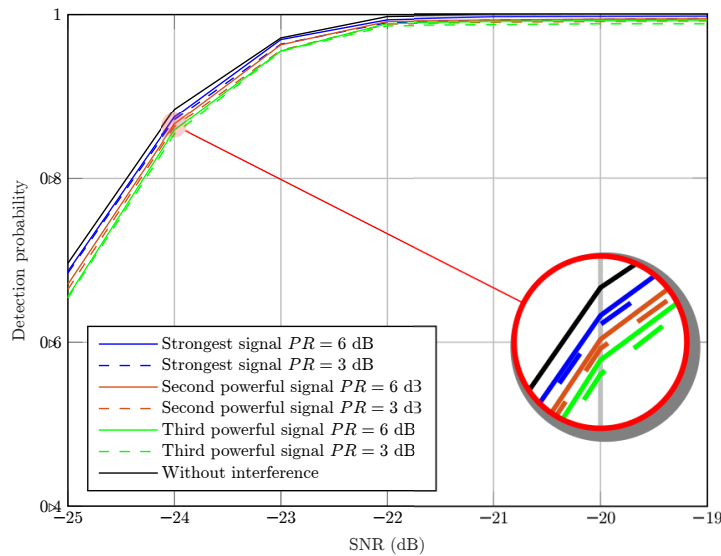


Figure 3.11: Start of frame detection with $SF = 12$ and $U = 3$

The first step that our receiver has to perform is the detection of the received LoRa-like packets and the identification of the effective start of the frames. Using the coarse and fine synchronization methods as described in 3.3.2.2, we obtained in Fig. 3.11 the following curves of the accurate detection probabilities of the start of the frame as function of the Signal to Noise

² Δf_{max} has been chosen based on the local oscillators precision used for LPWAN applications and given the order of the Doppler shift in LEO satellite communications.

Ratio (SNR). For each signal, the SNR is defined as:

$$SNR = \frac{P_i}{\sigma_w^2} \quad (3.37)$$

Fig. 3.11 shows that, for $PR = 6$ dB and $PR = 3$ dB, the start of frame detection of all the received signals are slightly affected compared to the case of a single LoRa packet received without interference. These results prove the immunity of our detection and synchronization (time and frequency) methods against same- SF interference. In addition, a nearly optimal detection is reached for the SNRs greater than -22 dB. Thus, this detection method is consistent with deployment requirements of the LoRa technology which define the SNR threshold, which is equal to -20 dB for $SF = 12$ as presented in Table 1.4.

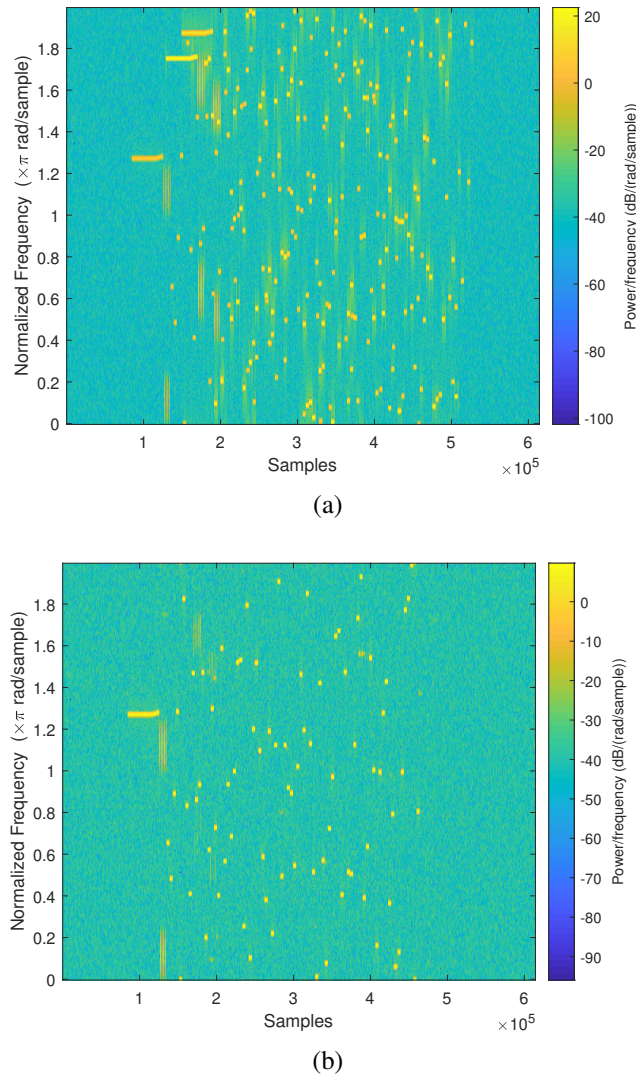


Figure 3.12: Evolution of the de-chirped block with $PR = 3$ dB, $SF = 12$ and $U = 3$ - (a) initial state - (b) after two iterations.

• SIC performance

To test the efficiency of our receiver to perfectly synchronize to the strongest signal and remove its contribution, we present in Fig. 3.12 the evolution of the de-chirped data block. Both spectrograms are obtained before performing the synchronization on the strongest signal in each iteration of our algorithm. Here we note that, in a synchronized mode, each de-chirped LoRa symbol gives constant frequency over the symbol time.

The spectrogram in Fig. 10a represents the initial de-chirped data block where the $U = 3$ preambles could be easily identified. We can observe the existence of 3 long temporal sequences having a constant frequency. Indeed, since the symbols of LoRa preamble have the same value, a constant frequency is obtained over N_p symbol times.

After iterating our algorithm twice, it can be seen in Fig. 3.12b, that the contribution of the two signals having the highest received powers are perfectly removed. Hence, our receiver performs accurate time and frequency synchronizations.

• Decoding performance

To evaluate the decoding performance of our proposed receiver, we display, in Fig. 3.13 and Fig. 3.14, the BER evolution of three superposed signals, with PR of 6 dB and 3 dB respectively, as a function of the SNR relative to each received signal as depicted in (3.37).

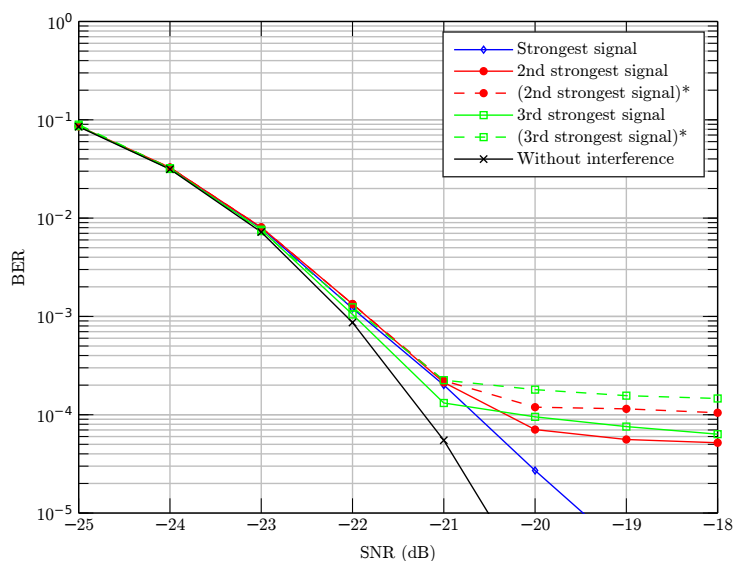


Figure 3.13: BER evolution with $PR = 6$ dB, $SF = 12$ and $U = 3$

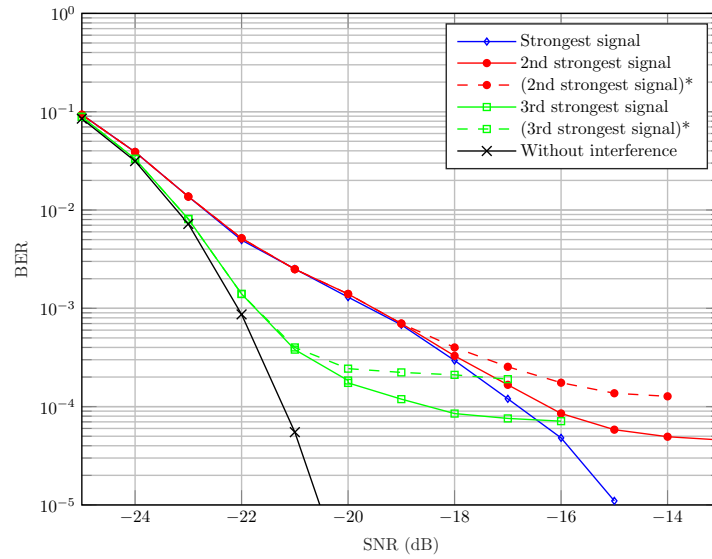


Figure 3.14: BER evolution with $PR = 3$ dB, $SF = 12$ and $U = 3$

We note that each dashed curve in both figures represents the BER of a received signal when all steps of our algorithm are performed, except for the processing of superimposed peaks. It can be seen that the decoding performance are enhanced (red and green solid curves) when we implement our algorithm to process the latter critical case.

Furthermore, based on [55], the solid blue curves in both figures show that the decoding performance of the strongest signal is almost identical to the case where only one same- SF interfering signal having a received power ratio of 3 dB and 6 dB is met. This result is explained by the fact that the contribution of the second strongest signal interferes more on the decision of the strongest signal symbols. In addition, we notice that its SNR threshold value, in Fig. 3.13 (resp. Fig. 3.14) is increased by almost 1 dB (resp. 5.3 dB) compared to the absence of interference case.

Once the latter signal is decoded, its contribution is removed to process the remaining signals. The solid red curves show that the decoding performance of the second strongest signal is slightly affected by comparing with the BER of strongest one. But, if the SNR is greater than -20 dB (resp. -15 dB) in Fig 3.13 (resp. Fig. 3.14) the BER remains almost constant. These results are explained by:

- the errors that occur when decoding the strongest signal and removing its contribution,
- the issue of superimposed peaks which can not be totally solved,
- the presence of the third strongest signal as an interfering signal with $PR = 6$ dB (resp. $PR = 3$ dB) in Fig. 3.13 (resp. Fig. 3.14).

Finally, the receiver has to process the remaining signal. The solid green curves show that the decoding performance of the weakest signal is slightly affected compared to the BER of one LoRa signal without interference. However, with a SNR ≥ -20 dB the BER remains almost constant. These results are also explained by the errors occurring when removing the previous signals. Nevertheless, in this case, the errors introduced by the SIC are more accentuated since two signals are already removed.

Based on the latter results, we can observe that our receiver can decode accurately 3 superposed signals with $SF = 12$ if we guarantee 6 dB as a minimum power ratio between them.

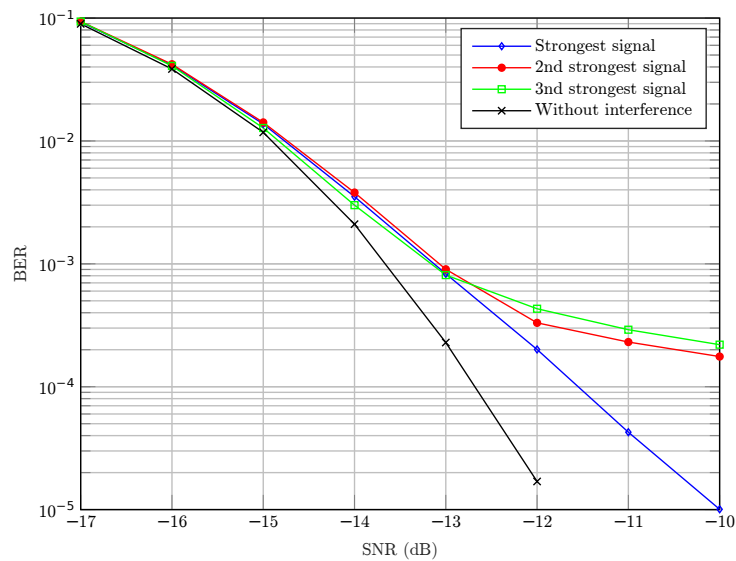


Figure 3.15: BER evolution with $PR = 6$ dB, $SF = 9$ and $U = 3$.

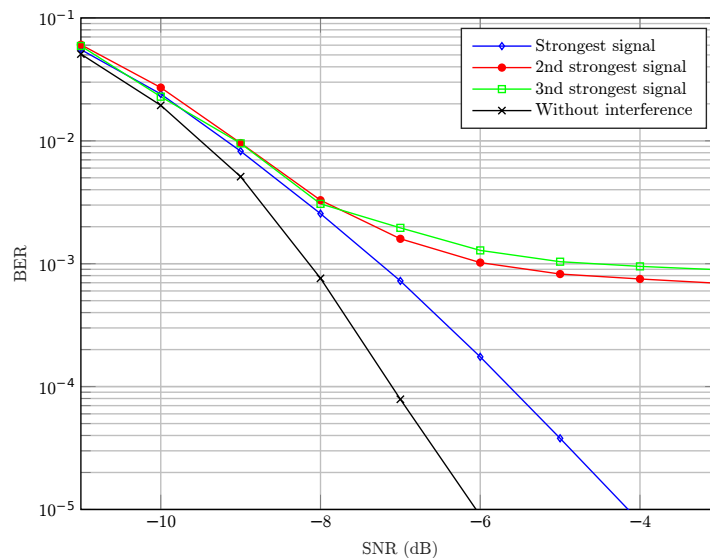


Figure 3.16: BER evolution with $PR = 6$ dB, $SF = 7$ and $U = 3$.

In all the latter simulations, we used $SF = 12$ which has the longest time on air and is

likely to involve collisions [115]. To show the impact of decreasing the SF on the decoding performance of our receiver, we represent in Fig. 3.15 the BER evolution of the received signals with $SF = 9$. It can be seen that we obtain almost the same results as in Fig. 3.13 with slightly degradation of the decoding performance of the second and the third received signals, which remain acceptable since a BER of 2×10^{-4} is reached at $SNR = 10$ dB for both signals. Similarly in Fig. 3.16, the latter performance degradation are more accentuated when the $U = 3$ superposed signals are received with $SF = 7$. Indeed, this degradation can be explained by the issue of superposed peaks which is more likely for the lowest SF since the number of points in the FFT is proportional to the SF .

Thus, our approach is more effective with the highest SF and allows to decode up to four simultaneously received signals as presented in the next simulation.

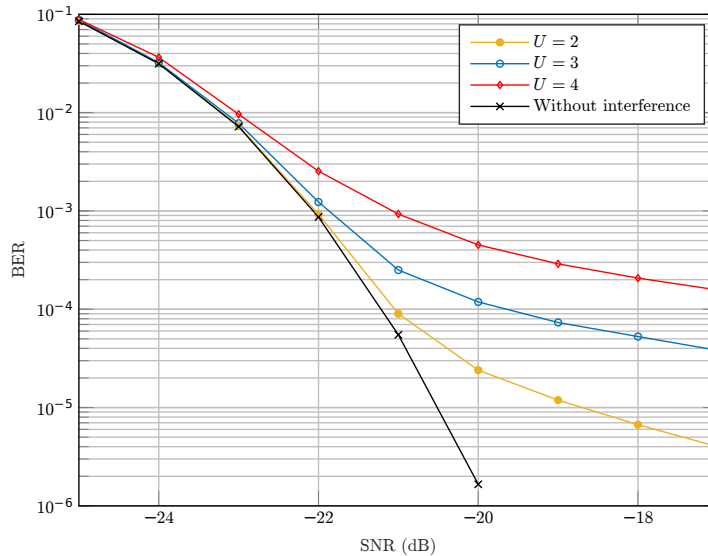


Figure 3.17: BER evolution of the weakest signal with $SF = 12$.

The final simulation test is to evaluate the impact of increasing the number of superposed signals on the decoding performance of our receiver. To this end, we represent in Fig. 3.17 the BER evolution of the weakest received signal during T_B . Here, we assumed that PR is uniformly distributed in $[6, 10]$ dB. In such configuration, we notice that for $U = 2$ the weakest signal is effectively decoded since at the SNR threshold SNR_{th} , the BER is equal to 2×10^{-5} . However, given that errors in decoding the synchronized signal are spread over the residual signals at each iteration, the decoding performance of the weakest signal are more degraded for $U \in \{3, 4\}$. Nevertheless, the latter performance remain acceptable since a BER of 10^{-4} is reached at SNR_{th} for $U = 3$ and a BER of 2×10^{-4} is reached for $U = 4$ at $SNR = -18$ dB.

3.3.3.2 Experimental validation using Software Defined Radio

In this section, we aim to validate our simulation results by considering real LoRa deployments. To that end, we use own-made LoRa nodes and gateways as represented in Fig. 3.18 and detailed in [116].

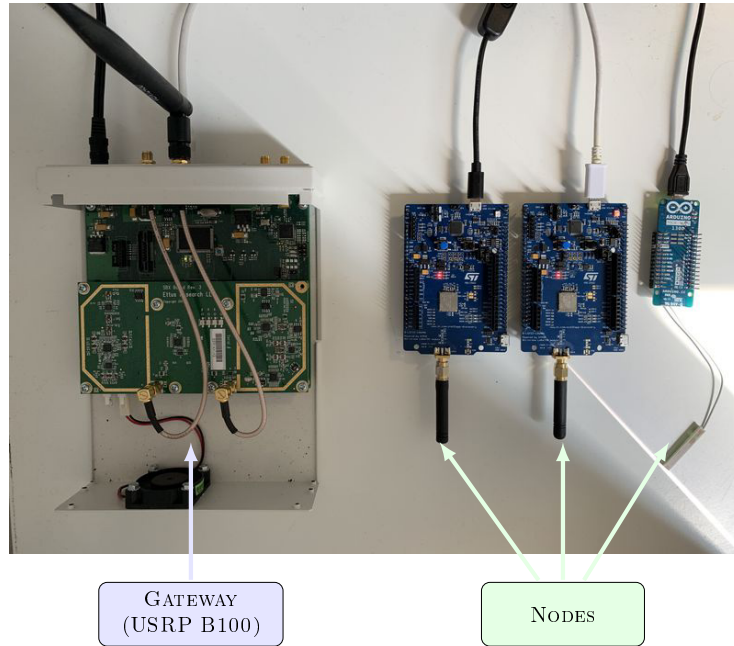


Figure 3.18: Test-bed: Three LoRa node transmitting and one USRP SDR device receiving data.

Three LoRa nodes ($U = 3$) are configured to transmit continuously, with the same SF (here $SF = 12$), the same message every second with a constant power ratio $PR = 6$ dB. Thus, high probability of collision between LoRa signals is obtained. All the nodes send data at a 868.2 MHz carrier frequency with a bandwidth $B = 125$ kHz. We also use Software Defined Radios (SDR) Universal Software Radio Peripheral (USRP) B100 [117] to acquire and process data.

In order to estimate the noise level detected by the receiver (i.e. compute σ_w^2), we start the acquisition on the receiver side when the nodes are on silence. Then, we start the transmission of all the nodes randomly without any previous timing synchronization. To maintain the same power ratio between received signals as configured in the nodes, the latter are placed at the same distance from the USRP.

Fig. 3.19 presents the result of the FFT processing in a p^{th} T -long section, where $U_p = 3$. It represents the capability of our receiver to synchronize on the strongest signal in each iteration and to remove its contribution to process the remaining signals.

The spectrum in Fig. 4.19a shows that, with real LoRa signals, it is difficult to obtain a perfect Dirac for the synchronized signal as the assumption we made in theory. We also notice

that this spectrum is consistent with (3.47), where each non synchronized signal contributes with two cardinal sines.

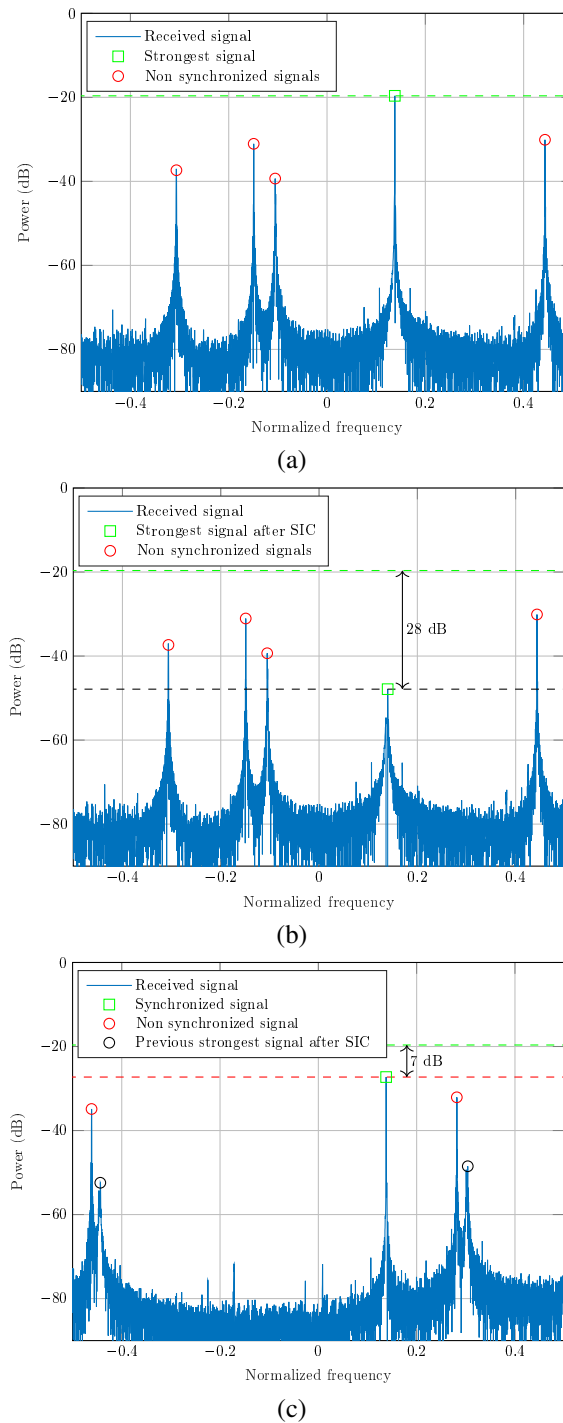


Figure 3.19: Result of the FFT - (a) synchronization on the strongest signal - (b) strongest signal cancellation - (c) synchronization on the second strongest signal.

Furthermore, as we can see in Fig. 3.19b, the contribution of the strongest signal is not perfectly removed but dramatically reduced by 28 dB. This proves that our receiver efficiently

performs time and frequency synchronizations and estimates accurately the frequency, the magnitude and the phase of the latter signal in each T -long section.

Once the contribution of the latter signal is removed, the receiver performs time and frequency synchronizations on the signal having the second highest received power. In Fig. 3.19c, it can be seen that the power ratio between the latter two signals is 7 dB, which is almost equal to the power ratio configured on the transmitting nodes since they are equidistant to the USRP. In addition, removing the contribution of the synchronized signal by almost 28 dB provides a good margin to process the remaining ones.

Finally, thanks to our approach, we were able to synchronize and decode the signal information from the 3 nodes. This result would increase considerably the capacity of LoRa technology-based networks, enhance the spectral efficiency and reduce the energy consumption of the nodes.

The capacity of our algorithm to simultaneously decode several uplink LoRa-like transmission, rises the utility of simultaneous downlink transmissions to send the acknowledgments (ACK) to the end-devices. Thus, we propose in the next paragraph, a downlink approach to deal with simultaneous LoRa-like transmissions over the same channel, with the same SF .

3.4 Proposed downlink approach to help nodes processing the multiple Reception of non-orthogonal LoRa-like signals

In the previous section we focused on packet collision in uplink communications. However, the collision and congestion issues exist in both ways: uplink and also downlink. In this section, we aim to propose to enhance the spectral efficiency of downlink transmission by allowing the simultaneous transmission of multiple packets on the same bandwidth when CSS communication is used. Indeed, we propose to control the time desynchronization of the superposed signals and to allocate different powers to the transmitted packets. The implementation of this solution is helped by the fact that the transmitted signals are received in phase. Based on the FFT size used to demodulate the CSS signals, we show that our proposition is naturally able to demodulate the interfering signals without any additional processing. If this is not the case, we propose to apply an interference cancellation algorithm coupled with a power allocation. Thus, this solution extend our previous work proposed in the previous section for an uplink scenario. Indeed, if the gateway is able to effectively process multiple superposed signals with the same Spreading Factor (SF), then it would require to send multiple and superposed acknowledgments in order to comply with the transmission protocol such as LoRaWAN [118]. Thereby, the connected

devices also need to be able to demodulate packets that can be in collisions. The relevance of our approach is demonstrated by simulations results in various scenarios when 2 packets are simultaneously transmitted.

3.4.1 System model

We consider a downlink communication system where several CSS signals are simultaneously transmitted on the same channel and with the same symbol time T . As an example, this situation can happen if the gateway receives in uplink several superposed signals and is able to decode all of them thanks to a dedicated algorithm such as the one presented in the Section 3.3. Indeed, the acknowledgment will be expected by each node on a similar time window. In this case, there is no orthogonal property between those signals. More precisely, the reception of a signal in the downlink case depends on level 2 protocol (MAC layer) for some energy consumption issues. Thus, if we consider a LoRa communications using LoRaWAN, the spectrum listening depends on the chosen communication class at the node level: A, B or C. In Class A, after sending messages, nodes expect an ACK from the network server during two pre-agreed time-slots known as receive windows (RW). Figure 3.20 depicts the RWs of Class A operating mode. Frequency and data rate of the first RW is the same as the uplink transmission parameters whereas the second slot operates on pre-agreed parameters to improve the robustness of message transmissions.

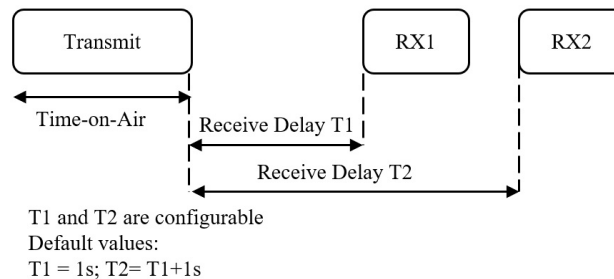


Figure 3.20: Receive Windows - Class A LoRaWAN

As explained previously, receiving simultaneously two or more signals with the same symbol time leads to a loss of orthogonality and may cause the destruction of all the packets. In the following, we express the construction of the signal that we propose to send in order to be able to decode the simultaneous reception of two interfering signals.

3.4.1.1 Model of transmitted signals

We consider a downlink communication system composed of two LoRa nodes and one gateway. If we note $s_1(t)$ and $s_2(t)$ the complex envelope of the payload transmitted by the gateway to

the first and second LoRa node, respectively, the transmitted signal is expressed as follows:

$$s_t(t) = \sqrt{P_1}s_1(t) + \sqrt{P_2}s_2(t - \delta t_{1,2}) \quad (3.38)$$

Where $\delta t_{1,2} \in [0, T)$ corresponds to the time desynchronization between packets destined to nodes 1 and 2, P_i is the power allocated to the i th node and $s_i(t)$, $i \in \{1, 2\}$ is defined as in (2.3).

In order for the receiver to detect and synchronize on $s_t(t)$, we propose that node 1 and 2 share the same preamble. Thus, a preamble signal $s_{train}(t)$ of duration T_t similar for both nodes is added. Finally, the signal transmitted by the gateway can be expressed as:

$$x_t(t) = \sqrt{P}s_{train}(t)\mathbb{1}_{[0, T_t]}(t) + s_t(t - T_t)\mathbb{1}_{[T_t, T_t + T_{st})}(t) \quad (3.39)$$

with $P = P_1 + P_2$ and T_{st} is the duration of (3.38).

3.4.1.2 Model of received signals

The received signal on the i th node, sampled at $T_s = \frac{1}{uB}$ ($u \geq 1$), is given by:

$$r_i(n) = x_t(n - \Delta n_i)e^{j2\pi n T_s \Delta f_i + j\theta_i} + w_i(n) \quad (3.40)$$

Where $w_i(n) \sim \mathcal{N}_{\mathbb{C}}(0, \sigma_w^2)$ is the additive white Gaussian noise (AWGN). Δn_i and Δf_i stand for the time and frequency desynchronization respectively while θ_i represents the initial phase.

To detect the reception of LoRa-like signals, the receiver has to be in a listening mode. A step by step method to detect and synchronize LoRa-like signal is described in the previous chapter.

Once synchronized, the CSS demodulator needs to perform a de-chirping operation such as explained in [83]. Then, it needs to estimate the most likely symbol by looking for the index which maximize a FFT absolute value. However, given the proposed communication strategy, some additional processing must be implemented so that the nodes can correctly demodulate all the superposed signals sent by the gateway. In the next section, we propose an original way to perform the demodulation of two interfering LoRa-like signals.

3.4.2 Proposed receiver

Without loss of generality, we propose to develop the receiver equations for the simultaneous reception of two packets to nodes 1 and 2.

The synchronization of nodes 1 and 2 will be performed in a similar way since they both share the same training message $s_{train}(t)$. Nevertheless, as their intended information are transmitted in a non-orthogonal way, each node needs to find its own data by removing the ISI or by using the time delay introduced by the gateway to synchronize alternatively on both nodes without interference. We consider that one bit of control is dedicated to the identification of the node. Then, the node will know on which signal it needs to synchronize and decode the information. Thereafter, we detail the processing on the node level and the requirements of the transmitted signal.

After synchronizations, the received signal for each node, sampled at $T_s = 1/B$, can then be written as follows:

$$y_1(n) = \sqrt{P_1}s_1(n) + \sqrt{P_2}s_2(n - \delta n_{1,2}) + w_1(n) \quad (3.41)$$

$$y_2(n) = \sqrt{P_1}s_1(n + \delta n_{1,2}) + \sqrt{P_2}s_2(n) + w_2(n) \quad (3.42)$$

With $\delta n_{1,2} = \frac{\delta t_{1,2}}{T_s} \in \{0, \dots, M - 1\}$.

Then, the processing of CSS signal is composed of two main steps: 1) dechirping and 2) symbol estimation based on FFT processing.

Thus, the signal obtained after the FFT and which corresponds to the processing of p th symbol of node 1 is equal to:

$$Y_1[k, p] = \frac{1}{\sqrt{M}} \sum_{n=0}^{M-1} \underbrace{(y_1(n, p) \overline{x_{ref}(n)})}_{z_1(n, p)} e^{-j2\pi \frac{nk}{M}} \quad (3.43)$$

where $y_1(n, p) = y_1(n + pM) \forall n \in [0, \dots, M - 1]$. Based on [52] and after some calculations:

$$\begin{aligned} z_1(n, p) &= \sqrt{P_1} e^{j2\pi \frac{nS_p^1}{M}} + \sqrt{P_2} e^{j2\pi \frac{n\bar{S}_{p-1}^2}{M}} \mathbb{1}_{[0, \delta n_{1,2}-1]}(n) \\ &+ \sqrt{P_2} e^{j2\pi \frac{n\bar{S}_p^2}{M}} \mathbb{1}_{[\delta n_{1,2}, M-1]}(n) + \tilde{w}_1(n) \end{aligned} \quad (3.44)$$

Where S_i^p $i \in \{1, 2\}$ is the p^{th} transmitted symbol by the i^{th} node and with

$$\bar{S}_p^2 = (S_p^2 - \delta n_{1,2}) \mod M \quad (3.45)$$

and

$$\bar{S}_{p-1}^2 = (S_{p-1}^2 - \delta n_{1,2}) \mod M \quad (3.46)$$

Based on (3.44), $Y_1[k, p]$ can be written as follows:

$$Y_1[k, p] = \sqrt{P_1 M} \delta(k - S_p^1) + Y_{1,p-1}[k, p] + Y_{1,p}[k, p] + \tilde{W}_1[k] \quad (3.47)$$

Where $\tilde{W}_1[k] \sim \mathcal{N}_{\mathbb{C}}(0, \sigma_w^2)$ is the FFT of the noise $\tilde{w}_1(n)$ and $Y_{1,p}[k, p]$ represents the FFT of the part of the chirp transmitted by node 2 and associated to the p th symbol S_p^2 . After some manipulations it is straightforward to demonstrate that:

$$Y_{1,p-1}[k, p] = \sqrt{\frac{P_2}{M}} e^{\theta_{p-1}} \delta n_{1,2} \frac{\text{sinc}\left(\pi \frac{\bar{S}_{p-1}^2 - k}{M} \delta n_{1,2}\right)}{\text{sinc}\left(\pi \frac{\bar{S}_{p-1}^2 - k}{M}\right)} \quad (3.48)$$

and

$$Y_{1,p}[k, p] = \sqrt{\frac{P_2}{M}} e^{\theta_p} (M - \delta n_{1,2}) \frac{\text{sinc}\left(\pi \frac{\bar{S}_p^2 - k}{M} (M - \delta n_{1,2})\right)}{\text{sinc}\left(\pi \frac{\bar{S}_p^2 - k}{M}\right)} \quad (3.49)$$

The two cardinal sines (3.48) and (3.49) represent the ISI from node 2 on node 1. It should be noted that since the arguments θ_p and θ_{p-1} are unnecessary in the following, they are not developed. A similar development can be achieved for $y_2(n)$.

In order for nodes to be able to demodulate the symbols intended for them, it is necessary to minimize or even eliminate the ISI. Thus, we propose the following two strategies.

3.4.2.1 Strategy based on the power diversity

The first strategy is to transmit the signals with the same power, $P_1 = P_2$ and to desynchronize them temporally by $\delta t_{1,2} = T/2$. Indeed, we can see from (3.48) and (3.49) that for $\delta n_{1,2} = \frac{M}{2}$, both cardinal sines peaks have the same power which corresponds to half the initial power i.e. a 6 dB loss. As a result, if $s_1(t)$ and $s_2(t)$ are delayed by $\delta t_{1,2} = \frac{T}{2}$ the power diversity gain is maximized. This result is interesting since we could transmit both signals at the same power on the gateway side and use only the time delay $\delta t_{1,2}$ to create a power diversity. Thus, this parameter would seem enough to directly demodulate the signal of interest without the needs to perform an interference cancellation. Fig. 3.21 shows the frequency representation of the received signals when a perfect synchronization on node 1 is assumed. We can clearly notice the two cardinal sines for the node 2 and the Dirac comb for the node 1. We can also see that, when $\delta t_{1,2} = T/2$, the power diversity on the spectrum is maximized and that the two cardinal sines are lowered at the same level.

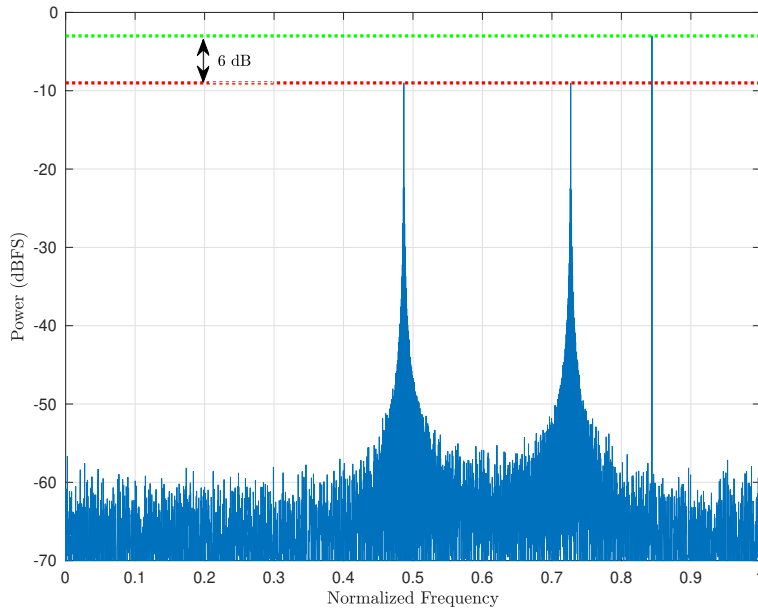


Figure 3.21: Observation used to demodulate a symbol when $\delta n_{1,2} = M/2$ and $SF = 12$

3.4.2.2 Strategy based on the power diversity and a SIC approach

The second strategy involves allocating different powers and implementing a successive interference cancellation (SIC) algorithm. Indeed, for a low value of SF , the power ratio obtained by setting $\delta t_{1,2} = T/2$ is not sufficient to limit the effect of the ISI. We then propose to allocate more power to a node. Thus, we limit the effect of the ISI on this node. Its demodulation is thus facilitated making it possible to cancel its contribution in the received signal. More precisely, when the interference cancellation is implemented, we consider the power ratio between the two nodes as follows: $PR = 10 \log_{10}(\frac{P_1}{P_2}) \geq 0$ dB. In this case node 2 has to cancel the contribution of node 1 before starting the decoding process of its frame. To this end, after the synchronization to the beginning of the payload of node 1, node 2 estimates, in each T -long sequence, the frequency, the magnitude and the phase of the main peak in the FFT. Then, it reconstructs the information of node 1 and removes it from the synchronized dechirped signal. After canceling the contribution of node 1, node 2 can identify easily the start of its frame by knowing the time delay $\delta n_{1,2}$.

In the next paragraph, we present some simulation results in order to study the relevance and the performance of our proposed solution.

3.4.3 Results and Discussions

The simulation results we present are obtained from the LoRa signal simulator that we developed in Matlab, where the interleaving and de-interleaving blocks, but also the channel coding/decoding parts are included.

In the following, the used signal to noise ratio (SNR) is defined for the i th node as $\text{SNR} = P_i / \sigma_w^2$. In addition, when time and frequency synchronization are performed, Δf_i and Δn_i are uniformly distributed in $\pm \frac{B}{4}$ and $[0, \dots, 10 \times T]$, respectively.

3.4.3.1 Impact of the Power Ratio and the SIC

We first consider the case of $SF = 7$ and study the decoding performance for different power ratio with or without the SIC algorithm.

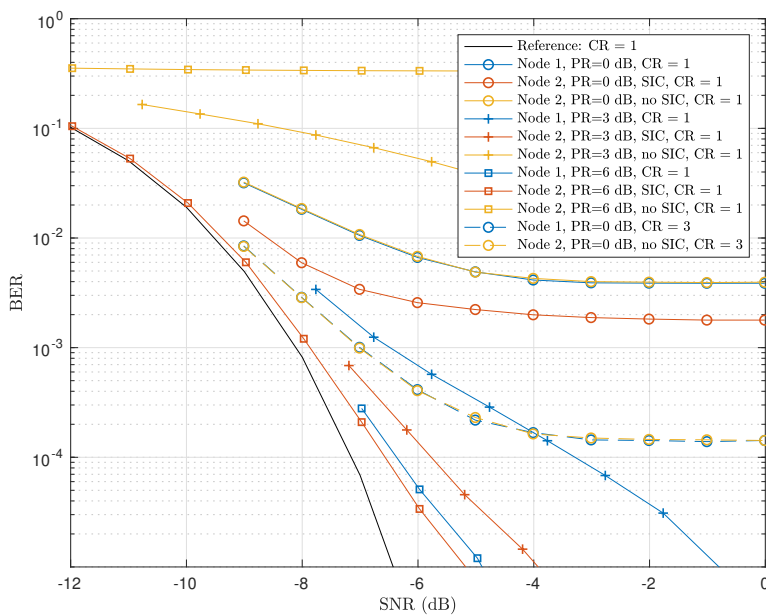


Figure 3.22: BER curves for node 1 and 2, $SF = 7$ and perfect time/frequency synchronizations

We can see in Fig. 3.22 the bit error rate (BER) evolution when perfect time and frequency synchronizations are considered. We can notice that the performance depends on the power ratio fixed between the two nodes at the gateway. Combined with the time delay $\delta t_{1,2} = T/2$ which creates another power diversity, we are able to perform the interference cancellation under certain conditions. Indeed, we can see that the best results are obtained for a larger PR i.e. PR=6 dB in our case. With $\delta t_{1,2} = T/2$, it means there is a gap of 12 dB between the peaks in FFT module which is enough to properly demodulate the first signal, to remove its contribution and to demodulate the other node. The decoding performance of node 2 are slightly degraded

for a lower PR, as it can be seen when PR=3 dB. Indeed, for a BER= 10^{-4} , compare to the reference performance (i.e the BER evolution without interference on AWGN channel) we have a loss of 0.6 dB for PR=6 dB whereas 1.3 dB are lost for PR=3 dB. In addition, we can see that for PR=0 dB (i.e. by only using the diversity introduced by $\delta t_{1,2}$), the SIC algorithm does not work properly since it appears there is not enough margin between the peak to properly demodulate the signals. We also represent the packet error rate (PER) results in Fig. 3.23 for packet length of 55 bytes.

We can notice that the results for PR=0 dB are close with or without SIC. Even though the performance are not completely satisfactory, we can see the BER floor can be reduced by enhancing the coding rate at CR = 3.

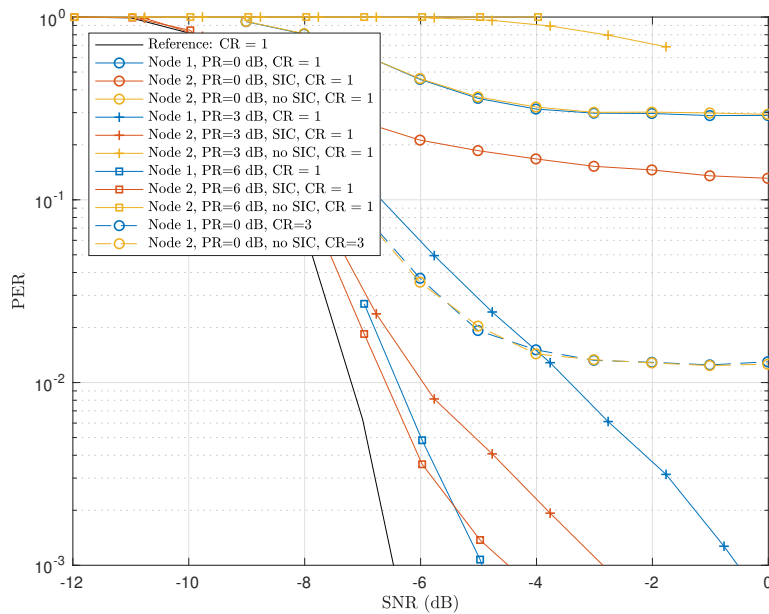


Figure 3.23: PER curves for node 1 and 2, $SF = 7$ and perfect time/frequency synchronizations

In the following paragraph, we propose to analyze the impact of SF and the coding rate on the performance of our proposal.

3.4.3.2 Impact of the SF and the coding rate

We now only consider the case of PR=0 dB i.e. by only using the power diversity introduced by the time delay $\delta t_{1,2}$ and study the impact of the SF when CR = 3. In Fig. 3.24, we can see that the SF has a direct impact on the decoding performance without using a SIC algorithm. Indeed, the greater the SF is, the lower is the BER floor. Moreover, although we saw in Fig. 3.22 that a coding rate increase enhances the performance for $SF = 7$, we can see here that the coding rate has a greater impact for larger SF s with performance close to the reference

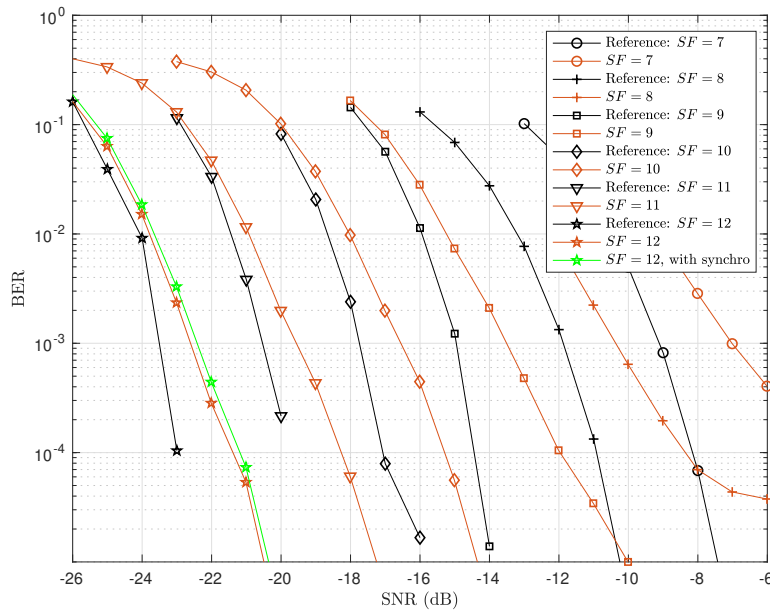


Figure 3.24: BER curves for node 2, different SF s, $CR = 3$, no SIC ($PR=0$ dB) and perfect time/frequency synchronizations unless stated otherwise

curve for $SF > 8$. In addition, we can see for $SF = 12$ that the performance remain excellent even when we activate the time and frequency synchronization algorithms. This fact is also confirmed by Fig. 3.25 which represents the BER performance only for $SF = 12$. We can see that, for this high SF , the SIC at $PR=6$ dB is much less necessary compared to no SIC at $PR=0$ dB whether for $CR = 1$ and especially for $CR = 3$ which was not the case in Fig. 3.22 for a low $SF = 7$.

It is also interesting to compare the results without SIC to the ones obtained with SIC and $PR=6$ dB. We chose here to present them through PER results in Table ???. We can see that these results confirm our first observation: The SIC with $PR=6$ dB can be interesting for low SF s such as $SF = 7$ and $SF = 8$ with a deviation even at ∞ for $SF = 7$ due to the PER floor. However, when we reach greater SF s, the SIC is no longer competitive since the results are close to the ones with no SIC at $PR=0$ dB. Moreover, we can see that the synchronization is well performed and does not degrade too much the performance. These results show that we are able, for certain SF ($SF > 8$), to properly decode the information of both nodes without interference cancellation with an appropriated coding rate. For lower SF s ($SF = 7$ and $SF = 8$), we need to add more power diversity at the gateway and so need to perform a SIC algorithm at the receiver side.

Our proposed approaches to deal with same- SF interference in uplink and downlink scenarios would improve the capacity of LoRa-based networks, and would make this technology more suited for LEO satellite communications. It is therefore important to implement a packet

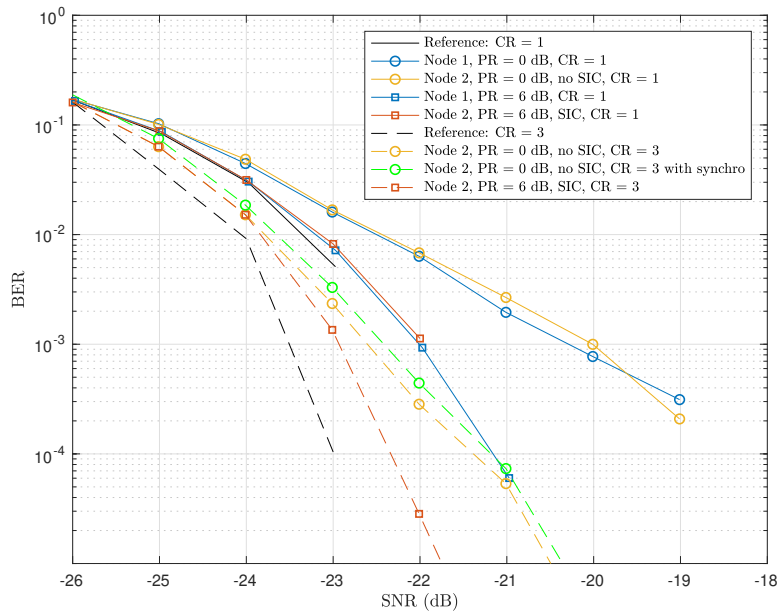


Figure 3.25: BER curves for node 1 and 2, $SF = 12$ and perfect time/frequency synchronizations unless stated otherwise

detection algorithm that can cope with this massive connectivity.

3.5 Proposed packet detection algorithm based on chirped signals

As already explained, the FoV of LEO satellite leads to connect a huge number of end-devices, that transmit their information without any previous synchronization using LPWAN technologies. The first task that the receiver must handle in this massive connectivity scenario is the packet detection. Subsequently, we propose in this chapter, an original preamble detection algorithm, using chirp-based signals. This work is a part of a project developed in a collaboration with Eutelsat, thus, several constraints, such the preamble duration and deployed bandwidth, are imposed by the former company. Furthermore, LEO satellite should cover highly dense urban areas as well as mountains, oceans, etc, where the coverage of terrestrial gateways is very limited. Thus, the proposed algorithm should have good performance in low and high connectivity scenarios.

3.5.1 Eutelsat specifications

Deploying LEO satellite as a gateway for IoT communications entails two possible strategies to process the received signals. The first one consists in demodulating the received packets in

the satellite and then send back the content of these signals to a ground station (GS), when the latter is in the visibility of the satellite. Whereas, the second approach consists in recording all the information received in a defined frequency bandwidth, then send the recorded data to the GS for further processing. In the case of this collaboration with Eutelsat, we considered the second approach to offload the complexity of the demodulation from their satellites and allow them to be independent from the technology used by the end-devices. Hence, it is important to implement an accurate packet detection algorithm that allow to validate the presence of desired signals in the recorded buffer that will be sent to the GS. Moreover, the waveform used in the preamble must be compatible with the different chips of the popular LPWAN technologies. Thus, this waveform should be integrated in LoRa and LR-FHSS chips such as SX1261 and SX1262 [53], and in Sigfox chips such S2-LPQTR and S2-LPCBQTR [119]. By looking in the data-sheets of the latter chips, we decide to adopt chirp based preambles. This choice is motivated also by the good performance of the detection method presented in Section 3.3.

Eutelsat proposed also to consider a frequency channel dedicated only for preamble detection. In other terms, the preamble and the payload messages are not transmitted over the same channel. This processing would reduce the impact of interference, generated by the payloads of other packets, on the preamble detection.

Finally, Eutelsat has imposed some constraints on the preamble duration and the channel bandwidth, dedicated for the detection purpose, that should be respectively lower than 150 ms and 10 kHz.

3.5.2 Structure of the preamble

The preamble is an overhead signal that does not contain useful information. It is usually used for packet detection and for further synchronization algorithms if needed. By respecting the aforementioned specifications introduced by Eutelsat, we propose to use chirp-based preamble, constituted by only raw chirps. As already explained, this choice is motivated by the good detection performance of the method presented in Section 3.3 and the compatibility of the former waveform with the chips of LPWANs, that would potentially be deployed for LEO satellite communications. Hence, we consider a preamble composed of N_p raw chirps, with the choice of N_p is constrained by the choice of SF , B and the preamble duration T_p . The complex envelop of the former preamble can be written as:

$$s_p(t) = \sum_{p=1}^{N_p} e^{j\phi_p(t-(p-1)T)} \mathbb{1}_{[(p-1)T, pT)}(t) \quad (3.50)$$

where $\phi_p(t)$ is defined as in (2.4), carrying the transmitted symbols $S_p = 0, \forall p \in \llbracket 1, N_p \rrbracket$.

Giving this structure of preamble, we propose in the next paragraph an original approach for the multiple packets detection that will be deployed at the satellite.

3.5.3 Proposed algorithm

We present, in this paragraph, our detection algorithm giving the aforementioned specifications. This algorithm is based on the one presented in Section 3.3, by introducing several additional processing in order to be able to detect the maximum possible of packets received in the data buffer.

The signals received in a defined data buffer can be expressed as:

$$y_r(t) = \sum_{i=1}^{N_R} \sqrt{P_i} x_i(t - t_{s,i}) e^{j(2\pi(\Delta f_i + \frac{c_{d,i} t}{2})t + \varphi_{0,i})} + w(t) \quad (3.51)$$

where

- N_R is the number of received signals in the recorded buffer,
- $P_i, t_{s,i}, \Delta f_i, c_{d,i}$ and $\varphi_{0,i}$ are respectively the power, the beginning time, the CFO, the DR and the initial phase of the i^{th} received signal,
- $x_i(t)$ is the complex envelop of the i^{th} received signal and can be written as:

$$x_i(t) = s_{p,i}(t) \mathbb{1}_{[0, T_p]}(t) + r_i(t - T_p) \mathbb{1}_{[T_p, T_p + T_{pkt}^i]}(t) \quad (3.52)$$

with $r_i(t)$ (resp. $s_{p,i}(t)$) being the complex envelop of the frame (resp. preamble) of the i^{th} received signal and T_{pkt}^i being its duration. To note that $r_i(t)$ is transmitted by end-devices using different LPWAN technologies like LoRa, Sigfox and LR-FHSS. Also the preambles are transmitted with a SF uniformly chosen in a set of possible ones.

In the next paragraph, we detail our detection algorithm without considering the impact of interference, which will be addressed later. In this case if two or more preambles are simultaneously received with the same SF , only one can be detected. Also, a preamble with a SF different than the intended one could be detected.

3.5.3.1 Preambles detection without interference

In order to increase the probability of packet detection, the preambles are transmitted with different SFs , which allows to take advantage of their quasi orthogonality. As already explained, we considered the use-case consisting in dedicating a frequency channel for packets detection. Thus, the baseband signals received in the channel dedicated for this purpose are sampled at the

rate $T'_s = \frac{1}{\alpha \times B_p}$, with B_p is the bandwidth dedicated for the preamble transmissions, and can be expressed as:

$$y_r(n) = \sum_{i=1}^{N_R} \sqrt{P_i} s_{p,i}(n - n_{s,i}) e^{j(2\pi(\Delta f_i + \frac{c_{d,i} n T'_s}{2}) n T'_s + \varphi_{0,i})} + w(n) \quad (3.53)$$

where $n_{s,i} = \lfloor \frac{t_{s,i}}{T'_s} \rfloor = K_{s,i} \alpha M + \tau_{s,i}$, with $\tau_{s,i}$ (resp. $K_{s,i}$) being the STO (resp. the index of T -long sequence given the beginning) of the i^{th} received signal.

To detect the presence of valid preambles, the receiver proceeds as follows:

1. Dechirp the samples recorded in the buffer for each deployed SF , using the dechirping sequence as in (3.42), sampled at the rate T'_s .
2. Compute the FFT in each T -long sequence of $y_r(n)$, after the dechirping process, as depicted in (3.21).
3. Compute the averaging function $T(k, p)$ as given in (3.24), with $k \in \llbracket 0, M - 1 \rrbracket$, $p \in \{1, \dots, N_B\}$ and N_B being the number of T -long sequences in the stored buffer.

To note that all the latter processing are done for each possible preamble, giving the configurations of SF and N_p . In addition, these treatments are performed with an oversampling $\alpha > 1$ since the CFO can reach important values in such communications (e.g. the maximum Doppler shift in Fig. 1.3 is 19 kHz) and can exceed the narrow bandwidth dedicated for preamble detection. Moreover, the oversampling enhances the detection probability since it entails the increase of the FFTs magnitudes.

By following the former steps, the result of the averaging function $T(k, p)$, $k \in \llbracket 0, M - 1 \rrbracket$ and $p \in \{1, \dots, N_B\}$ as function of $k \times p$, when processing packets received with $SF = 7$ (i.e. using dechirping sequence with $SF = 7$) and $N_p = 8$, is given in Fig. 3.26.

Hence, as we can see in the latter figure, a specific pattern allowing us to identify the desired preamble is obtained. Giving the expression of $T(k, p)$, if the oversampling is not considered (i.e. $\alpha = 1$), it is expected to find $2N_p - 1$ peaks per pattern, where the distance between each two consecutive peaks is equal to αM . In other terms, for the i^{th} received signal, $\forall p \in \{K_{s,i} - N_p + 1, \dots, K_{s,i} + N_p - 1, \}$, one peak should be detected in $T(k, p)$. Whereas, the highest peak of the latter pattern is obtained for $p = K_{s,i}$, since in this case all the FFT in the averaging function belong to the desired preamble. Nevertheless, when computing the FFTs with αM points, with $\alpha > 1$, each of them will contribute by two peaks, distant by $\pm M$, even in a perfect time synchronization without interference [58]. Subsequently, to confirm the presence of a valid preamble the previous pattern should be identified. However, the magnitude of the maximum of $T(k, p)$ is much greater for $p = K_{s,i}$ than for $p \in \{K_{s,i} - N_p + 1, K_{s,i} + N_p - 1, \}$.

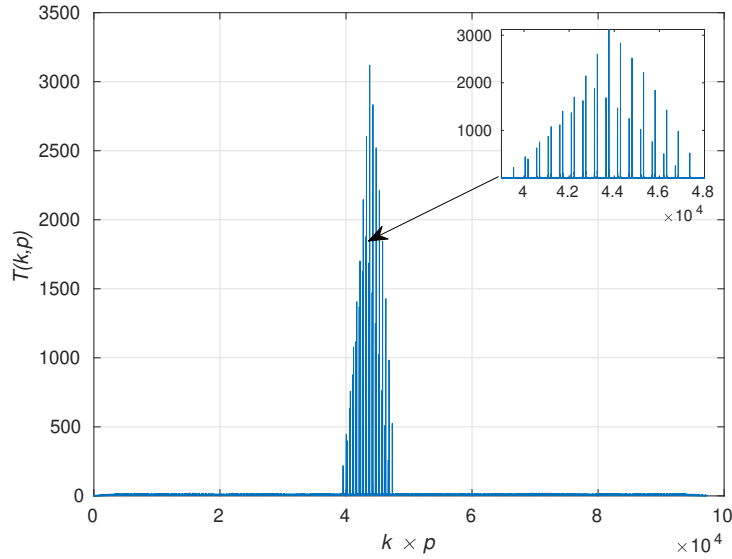


Figure 3.26: Result of $T(k, p)$, in the case without interference, allowing to detect received signals with $SF = 7$, $B_p = 7.8$ kHz and $N_p = 8$.

Thus, to increase the probability of detecting the i^{th} received signal, it is much better to reduce the number peaks per pattern that should be identified in order to confirm the presence of a valid packet. Thus, after computing $T(k, p)$, $k \in \llbracket 0, M - 1 \rrbracket$ and $p \in \{1, \dots, N_B\}$, the next step of our algorithm is to identify a reduced pattern by:

- computing the function $M(p)$, $p \in \{1, \dots, N_B\}$ as defined in (3.25),
- searching all the peaks of $M(p)$ that exceed the threshold Th as defined in (3.28) by respecting a minimum distance of N_p between each two consecutive of them to ensure selecting the maximum of two different pattern. In other terms, it consists in finding the vector Ls such that $Ls = \{\hat{K}_{s,i}, i \in \{1, \dots, N_R\}\}$,
- verifying the existence of a peak that exceed the threshold in each of the T -long sequences $K_{s,i} - 1$ and $K_{s,i} + 1$ located at the same FFT bin as the maximum in the T -long sequence $K_{s,i}$.

This method is efficient only if there are no time overlapping between the received preambles. In this case, when a high number of signals are received in the data buffer, it is very likely that false detections are produced. Thus, it is necessary to enhance this algorithm in order to manage the multiple packets reception, which is the purpose of the next paragraph.

3.5.3.2 Management of the multiple packets reception

To enhance the accuracy of our proposed preamble detection algorithm, it is mandatory to manage the reception of multiple packets in the same buffer by tackling the issues of inter- SF as well as same- SF interference.

- **Inter- SF interference**

In order to increase the number of end-devices that could be connected to the satellite, we can use several orthogonal waveforms in the deployed preambles. To this end, we take advantage of the quasi-orthogonality of LoRa-like signals with different SF , by considering that each preamble is transmitted with an SF randomly chosen from a set of possible ones. The latter set of SF s is defined such that we maintain the same preamble duration T_p , given the number of chirps N_p in the and the bandwidth B_p of the latter preamble.

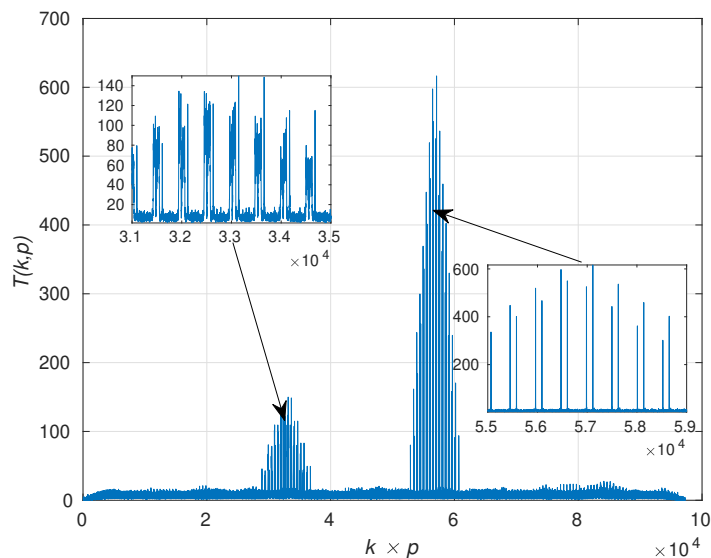
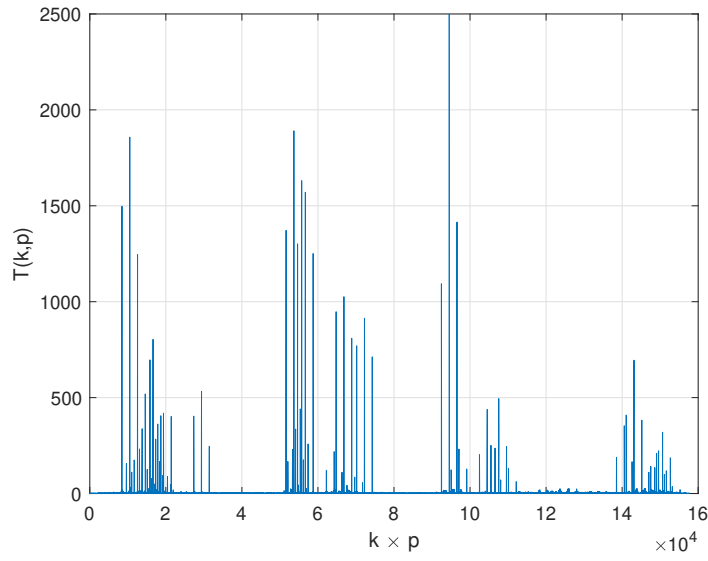


Figure 3.27: Result of $T(k, p)$ allowing to detect received signals with $SF = 7$, $B_p = 7.8$ kHz and $N_p = 8$.

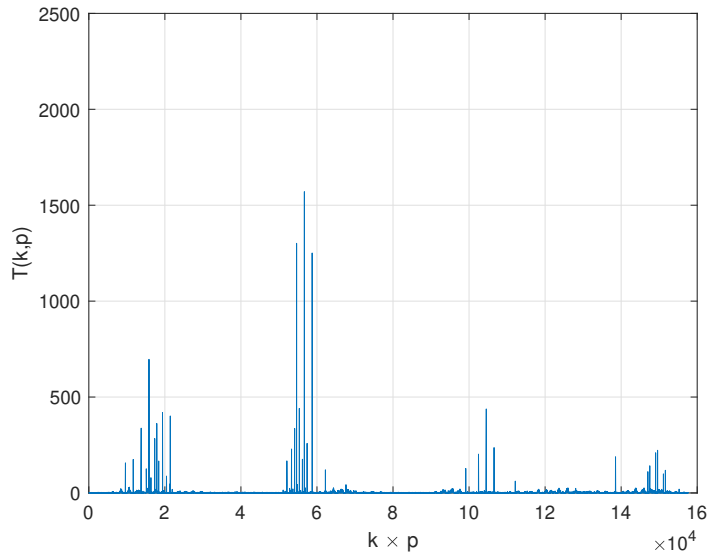
To understand the impact of inter- SF interference on our preamble detection algorithm, we represent in Fig. 3.27, the results of $T(k, p)$, $k \in \llbracket 0, M - 1 \rrbracket$ and $p \in \{1, \dots, N_B\}$ as function of $k \times p$, when processing packets received with $SF = 7$ and $N_p = 8$. We can easily identify in the latter figure, the presence of the pattern corresponding to a valid preamble transmitted using the latter configuration. Moreover, we can notice the presence of a second preamble, which does not have same proprieties as the intended ones (i.e transmitted with $SF = 7$ and $N_p = 8$). The former preamble, is transmitted with $SF = 9$ and $N_p = 2$, yet, it can verify the conditions of a valid detected packet as defined in the latter paragraph. We notice also that this interfering

preamble does not contribute by only two peaks when computing $T(k, p)$ in a defined T -long sequence of the pattern. Thus, to avoid the detection of preamble having an other SF than the intended one, we propose to add the constraint of peak to average ratio that should exceed a defined threshold. In other terms, the ratio $\frac{\max_k(T(k,p))}{\text{mean}_k(T(k,p))}$, $p \in \{K_{s,i} - 1, K_{s,i}, K_{s,i} + 1\}$ should be greater than the latter threshold.

- **Same- SF interference**



(a)



(b)

Figure 3.28: Result of $T(k, p)$ allowing to detect received signals with $SF = 9$, $B_p = 7.8$ kHz and $N_p = 2$ - (a) initial state - (b) after one iteration.

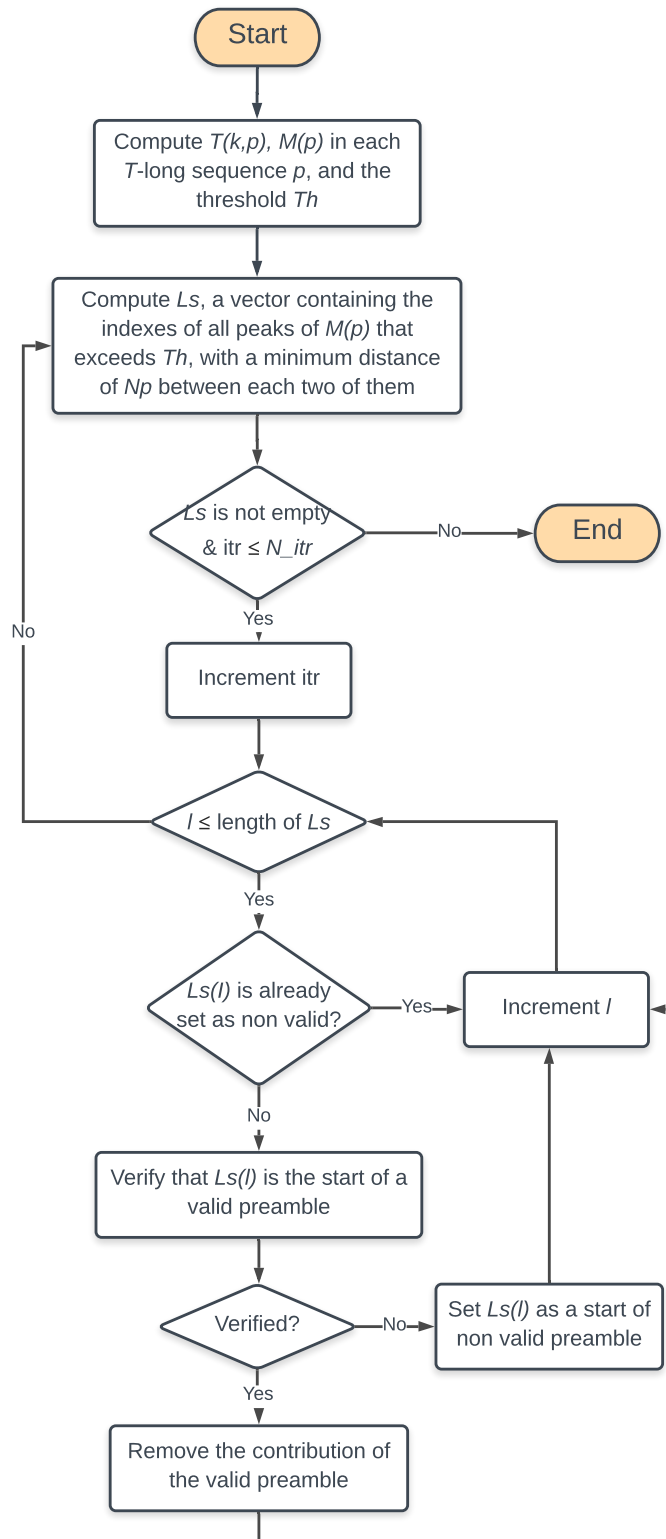


Figure 3.29: Preamble detection algorithm.

As already explained, LEO satellite is able to connect a huge number of end-devices, thus, it is very likely to simultaneously receive several preambles with the same- SF . As we can

notice in Fig. 4.28a, several preambles, transmitted with $SF = 9$ and $N_p = 2$, are overlapped. Thereby, if we do not add an approach to deal with such interference, our algorithm could not detect more than one preamble from the ones in collision. To tackle this issue, the contribution of each valid detected preamble should be removed in order to process the remaining overlapped packets. To cancel the contribution of a valid preamble, all the peaks of the identified pattern are set to zero. In this way, we propose an iterative algorithm allowing to detect all the possibly-identified valid preambles in each iteration, remove their contributions, then process the reminding ones until no more valid preambles are detected in the buffer or the maximum number of iterations N_{itr} is exceeded. The results of the averaging function in the second iteration of our algorithm are depicted in Fig. 3.28b. We can easily notice that several valid preambles was detected and removed in the first iteration, which allows the processing of the ones in collision.

Finally, all the previous steps of our proposed algorithm are summarized in the flowchart shown in Fig. 3.29.

To validate the performance of our aforementioned algorithm, simulation results are represented and commented in the next paragraph.

3.5.4 Results and Discussions

The objective of this paragraph is to evaluate the detection performance of our algorithm in different system loads. Here, we define the system load as $\frac{N_R T_p}{T_B}$, with $T_B = N_B T$ is the duration of the data buffer (i.e. the buffer size is equal to $\frac{T_B}{T_s}$). Given the constraint of bandwidth dedicated for preamble detection imposed by Eutelsat (i.e. lower than 10 kHz), we propose to use the lowest bandwidth that is supported in LoRa chipsets [59], which is equal to 7.8 kHz. Yet, reducing the bandwidth, causes an increase in the duration of preamble deployed for the detection purpose. Thus, in order to maintain the duration lower than the constraint imposed by Eutelsat (i.e. lower than 150 ms), we propose to employ the following configuration, as depicted in Table 3.4.

Table 3.4: Preamble configurations

SF	7	8	9
B_p (kHz)	7.8	7.8	7.8
N_p	8	4	2
T_p (s)	0.131	0.131	0.131

In the upcoming simulations, we consider that the number of packets received in a buffer follows the Poisson distribution. Also, the distance between LEO satellite and end-devices change during the window of visibility. Thus, the packets are received with powers uniformly

distributed in the set $[P_{mean} - PS, P_{mean} + PS]$, with $P_{mean} = \frac{1}{N_R} \sum_{i=1}^{N_R} P_i$ is the mean received power and PS is the power spreading. More details on the simulation parameters are illustrated in Table. 3.5.

Table 3.5: Simulation parameters

Carrier frequency f_c (MHz)	868
Preamble bandwidth B_p (kHz)	7.8
Maximum CFO Δf_{max} (kHz)	20
Maximum DR DR_{max} (Hz/s)	300
Power spreading PS (dB)	5
Mean SNR (dB)	0
Oversampling factor α	{2, 4}
Probability of false alarm P_{fa}	10^{-3}
Buffer duration T_B (s)	5
Number of algorithm iterations N_{itr}	{2, 3, 4}
Number MC simulations	10000

To note that the mean SNR is equal to $\frac{P_{mean}}{\sigma_w^2}$ and the CFO (resp. the DR) is uniformly distributed in $[-\Delta f_{max}, \Delta f_{max}]$ (resp. $[-DR_{max}, DR_{max}]$). Moreover, we considered a typical value of power spreading of 5 dB, when communicating with LEO satellite of altitude of 550 km. This value was provided by Eutelsat after some measurements.

The first test consists in evaluating the effect of varying the number of iterations N_{itr} and the oversampling factor α of our algorithm on detection performance. To this end, we represent respectively in Fig. 3.30 and Fig. 3.31 the good detection and the false detection probabilities as function of the system load. For $\alpha = 4$, it can be easily seen that increasing N_{itr} allows to enhance the good detection rate and slightly increase the probability of false detection, especially for low system load. We notice also for low system loads, almost all the packet are accurately detected. The detection accuracy is maintained also for high system loads, especially for $N_{itr} > 2$. Indeed, for a system load of 2.6 (i.e. on average 100 preambles are received in buffer of duration $T_B = 5$ s), the good detection probability is equal to 0.92 (resp. 0.9) for $N_{itr} = 4$ (resp. $N_{itr} = 3$). Whereas, for the same value of α , the false detection probability is lower than 2×10^{-3} , when the system load is greater than 1.4, with all the values of N_{itr} . Also for low system loads (i.e. lower than 0.6), our algorithm maintains the low values of the former probability, which does not exceed 0.025 in the worst case. It should be noted that the false detections are essentially caused by inter- SF interference and the detection of the same preamble in multiple iterations of our algorithm (i.e. valid preamble not perfectly removed).

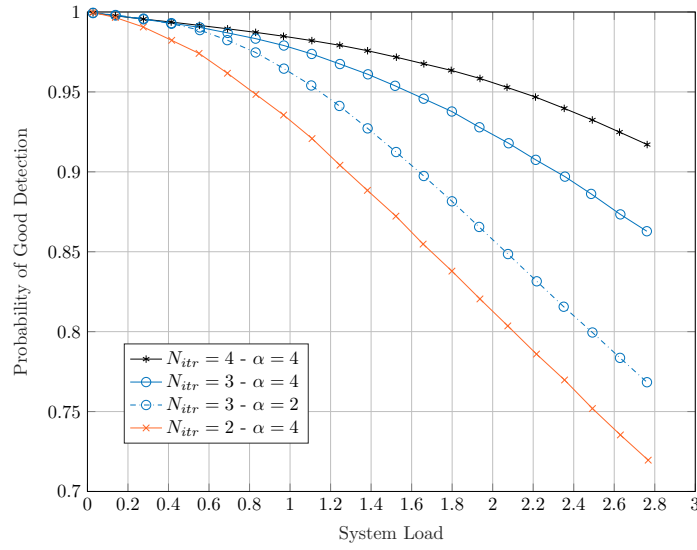


Figure 3.30: Good detection probabilities for different N_{itr} and α values.

Moreover, the impact of the oversampling factor α on the good and false detection performance is illustrated by blue curves of the latter two figures. When considering $N_{itr} = 3$, we can notice, in Fig. 3.30, that the good detection probability is enhanced when increasing α , especially for high system loads. In fact, for a system load of 2.6, the former probability is equal to 0.79 for $\alpha = 2$ and 0.88 for $\alpha = 4$. Whereas, the increase of α results in a higher number of false detections for all the system loads. For instance, as we can see in Fig. 3.31, for a load of 0.03 (i.e. on average 1 preamble is received in buffer of duration $T_B = 5$ s), the false detection probability is equal to 0.002 for $\alpha = 2$ and 0.024 for $\alpha = 4$. Thus, based on these results we can propose to use an oversampling factor $\alpha = 4$ since it has better good detection performance and causes a small number of falsely detected preambles.

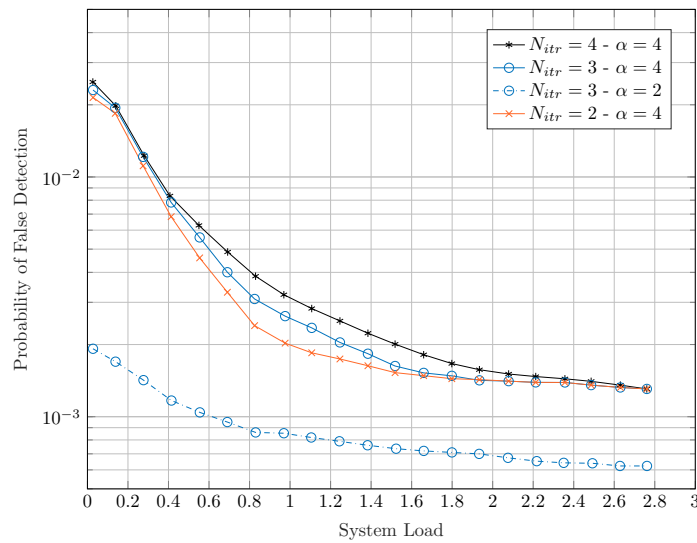


Figure 3.31: False detection probabilities for different N_{itr} and α values.

Finally, we show, in Fig. 3.32, the probability of good detection for each deployed SF , with $N_{itr} = 3$ and $\alpha = 4$. It is easy to see that the detection performance are inversely proportional to the increase of SF . This result is explained by the number of chirp in the preamble N_p , which is doubled by increasing the SF by one in order to maintain the same preambles duration.

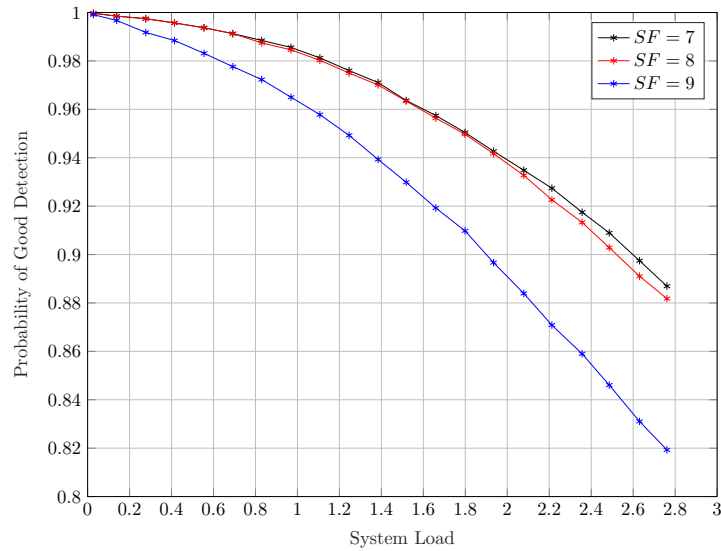


Figure 3.32: Good and false detection probabilities for each SF with section $\alpha = 4$ and $N_{itr} = 3$.

3.6 Conclusion

In this chapter, we focused on the packet collisions in LoRa-like communications, which is a serious issue when considering uplink transmissions to LEO satellites. These collisions are caused by inter as well as intra technology interference. First, we modeled the impact of UNB interfering signals on LoRa-like communications, since the majority of LPWAN technologies in ISM bands other than LoRa employ UNB transmissions. Based on the latter models, we provided simulation results that prove the robustness of chirp-based signals to UNB interference. We proved also that the impact of the former interfering signals is proportional to their bandwidth B_{nb} and inversely proportional to the symbol time T of the desired signal.

After that, we concentrate on the second type of interference caused by packets collisions from same technology. We start by formalizing the impact of inter as well as same SF interference on LoRa-like communications. In this context, it was proved in the literature that LoRa signals with different SF 's are not perfectly orthogonal, but, a very low SIR can guarantee accurate demodulation process. Whereas, currently when two or more signals are simultaneously received in the same channel with the same SF only the strongest signal can be accurately decoded if it has a power 6 dB greater than the second powerful interfeferer. The latter process

is usually called the capture effect. This type of interference is the major cause that limits the throughput of LoRa-based networks and would very likely occur when communicating with LEO satellites. Hence, we proposed in Section 3.3, a novel algorithm allowing to decode several superposed LoRa-like signals based the SIC. Indeed, we showed through mathematical models, simulation results and experimental validation that simultaneously received LoRa-like signals with the same SF could be processed and we were able to extract the information from the transmitting nodes. As a result, our novel approach would reduce the energy consumption of the nodes and enhance the capacity of LoRa technology-based networks since it decreases the number of re-transmitted packets. Our solution has also the advantage of using the commercialized LoRa chip to process collisions. Thus, it can be easily implemented to an existing network to enhance spectral efficiency.

Furthermore, in such network congestion, we showed that the latter destructive collisions are likely to occur in downlink communications, and thus we proposed a novel approach to deal with this issue in LoRa-based networks. Indeed, In the case of a gateway communicating with two nodes using the same SF , we showed in Section 3.4 that we were able to adapt our previous interference cancellation algorithms to this specific case by employing power diversity at the gateway and by introducing a time delay so that the received power are optimized to perform the demodulation. Moreover, we showed that a power diversity at the transmitter was not necessary and that the SIC was not necessarily needed when the signals are sent at the same power. This solution was validated through simulations which tend to show that this method can be applied in existing IoT networks and thus enhance the spectral efficiency.

Finally, we proposed in Section 3.5, a packet detection algorithm using a chirp-based preambles that can be implemented on a LEO satellite. The goal of this work is to detect the maximum possible of packets transmitted by node using different LPWAN technologies in ISM bands. Thereby, the information transmitted by the latter nodes are continuously recorded in data buffers and then forwarder the a GS for further processing.

By using our algorithm, we showed that we are able to almost detect all the received signals in low system loads for all the tested use-cases, while keeping low false detection probabilities. As explained earlier, the latter false detections are caused by inter- SF interference and the detection of the same preamble in several iterations, thus, it will not trigger the starting of the data recording when no signal is actually received. Moreover, in high system loads, simulation results prove that our algorithm has a high good detection rates and the probability of false detection is very low, especially when increasing α and N_{itr} . Thus, thanks to its good performance in low and high system loads, our algorithm was validated by Eutelsat and will be tested with real recorded data from their satellite.

Conclusion and perspectives

Conclusion

In this thesis, we have investigated LEO satellite communications using LoRa-like signals. The goal of our works in this PhD thesis is to make this waveform suited for such communications. Hence, with our propositions, it would be possible to achieve world-wide coverage for LoRa-based networks and serve their IoT applications via LEO satellites. This choice of technology is motivated by the popularity of the LoRaWAN protocol and the several industry trends to employ it for satellite IoT given its capacity to establish extremely long range communications and maintain low energy consumption of the nodes. As we have explained in this dissertation, currently, using this LPWAN technology for satellite IoT applications faces two main challenges. The first one is caused by the significant Doppler effects due to the extremely high speed of such satellites. In this context, the low data rates in LoRa, that close link budget of LEO satellites, are very sensitive to the DR. Moreover, the current synchronization algorithms deployed in LoRa receivers cannot perform accurately if the CFO is greater than the quarter of the bandwidth. The second challenge of such communications is entailed by the FoV of LEO satellites, which allow to connect huge number of nodes. This massive connectivity would increase the probability of packet collision, especially known the random access protocols to the frequency channel as used in LoRa-based networks.

In Chapter 1, we discussed some principals of LEO communications and we provided the requirements of being LPWAN and we gave an overview on several of them. We presented also a brief study on the capacity of each of latter LPWANs to cope with the requirements of LEO satellite communications in terms of link budget and robustness to Doppler effects and interference. We showed that in LoRa only the lowest data rates can close the link budget of LEO communications, but, the latter are very sensitive to the DR.

Chapter 2 presented, at first, the impact of synchronization errors on the LoRa symbol estimation in the context of LEO communications. We proved that synchronization algorithms used in LoRa receivers lead to a maximum CFO estimable of the quarter of the bandwidth.

To bypass this constraint and enhance the robustness of LoRa-like signals to Doppler effects, especially the DR, we proposed a modification to the LoRa PHY layer, referred to as DCSS. We demonstrated that DCSS has much better robustness to the DR than the CSS modulation. Hence, based on the DCSS waveform and two synchronization algorithms, we proved the possibility to deploy LoRa-like signals, with the lowest data rates, in order to communicate with LEO satellite.

Finally, in Chapter 3, we exploited the structure of LoRa-like signals in order to propose several approaches to detect and decode superposed signals, simultaneously received over the same channel and with same SF . In the uplink context, based on the SIC algorithm, we proved the capacity of our proposed receiver to accurately decode up to four superposed signals according to the considered configuration. In the downlink, we demonstrated the possibility to decode two superposed LoRa-like signals without performing the SIC algorithm. Finally, we proposed a novel approach for packet detection purpose using chirp-based preambles. We proved that our algorithm has good performance in massive and low connectivity scenarios, which perfect for further deployment in a LEO satellite.

With all our enhancements, LoRa technology could be more suited to establish global connectivity via LEO satellites. In the next paragraph we provide some perspectives of our works.

Perspectives

In this PhD thesis, we focused only on the LoRa PHY and we proposed several enhancements to make it more suited for LEO satellite communications. A more detailed study on the robustness of other LPWAN technologies to Doppler effects and interference than the one presented in the Chapter 1 could be performed. Moreover, in all simulations in this dissertation, we considered AWGN channel. This choice is realistic given the narrow band of LoRa-like transmission. Nevertheless, other type of channels could be tested as future works in the context of LEO satellite communications.

In Chapter 2, we plan to test our two proposed synchronization algorithms in real-time communication with Eutelsat satellites. The first algorithm, as depicted in Section 2.5, was developed with C++ in software defined radios B100 and is ready to be tested in such scenario.

In Chapter 3, we plan to enhance our approach of dealing with destructive LoRa-like collisions in uplink context by improving our SIC algorithm, especially for the lowest SF 's where the issue of superposed peaks in the FFTs is more likely than in the case of the highest ones. We will incorporate as well the DR estimation and compensation in our algorithm.

We intend also to enhance our approach to deal with downlink destructive collision by proposing an optimization of the power diversity distribution using the received SNR for the uplink

communication and to analyze the capacity of the receiver to process more than two users. Also it is possible to accurately decode four superposed payloads by modulating two of them with up chirps, whereas down chirp modulation is performed for the other two.

Finally, we plan to evaluate our packet detection presented in Section 3.5 with real recorded data by Eutelsat satellites.

List of Publications

Journal Articles

- [J-1] M. A. Ben Temim, G. Ferré, B. Laporte-Fauret, D. Dallet, B. Minger and L. Fuché, "An Enhanced Receiver to Decode Superposed LoRa-Like Signals," in IEEE Internet of Things Journal, vol. 7, no. 8, pp. 7419-7431, Aug. 2020.
- [J-2] M. A. Ben Temim, G. Ferré and R. Tajan, "A New LoRa-like Transceiver Suited for LEO Satellite Communications," in Sensors 2022 (major revision).

Conference Papers

- [C-1] B. Laporte-Fauret, M. A. Ben Temim, G. Ferré, D. Dallet, B. Minger and L. Fuché, "An Enhanced LoRa-Like Receiver for the Simultaneous Reception of Two Interfering Signals," 2019 IEEE 30th Annual International Symposium on Personal, Indoor and Mobile Radio Communications (PIMRC), 2019, pp. 1-6.
- [C-2] M. A. Ben Temim, G. Ferré and R. Tajan, "Analysis of the Coexistence of Ultra Narrow Band and Spread Spectrum Technologies in ISM Bands," in Ubiquitous Networking. Springer International Publishing, 2020, pp. 5667.
- [C-3] M. A. B. Temim, G. Ferré, R. Tajan and B. Laporte-Fauret, "A Novel Approach to Process the Multiple Reception of Non-Orthogonal LoRa-Like Signals," ICC 2020 - 2020 IEEE International Conference on Communications (ICC), 2020, pp. 1-6.
- [C-4] M. A. Ben Temim, G. Ferré and R. Tajan, "A Novel Approach to Enhance the Robustness of LoRa-Like PHY Layer to Synchronization Errors," GLOBECOM 2020 - 2020 IEEE Global Communications Conference, 2020, pp. 1-6.
- [C-5] G. Ferré, B. Laporte-Fauret and M. A. Ben Temim, "A Downlink Non Orthogonal Multiple Access for Chirp Spread Spectrum Communications," 2020 IEEE Latin-American Conference on Communications (LATINCOM), 2020, pp. 1-6.
- [C-6] G. Ferré and M. A. Ben Temim, "A Dual Waveform Differential Chirp Spread Spectrum

Transceiver for LEO Satellite Communications," ICC 2021 - IEEE International Conference on Communications, 2021, pp. 1-6.

List of Figures

1.1	Description of the Elliptical orbit from [18]	24
1.2	Ellipse and the circumscribed auxiliary circle from [18].	26
1.3	Doppler shift and Doppler rate evolution from an Eutelsat nano-satellite with a typical altitude of 550 km and given the carrier frequency of 868 MHz	30
1.4	BER of NB-IoT using the uncoded QPSK modulation	37
1.5	The range of NB-IoT with different transmission modes	39
1.6	BER Sigfox DBPSK on AWGN channel	41
1.7	Range of Sigfox uplink transmissions as function of the satellite antenna gain G_{RX} , with $B_{sig} = 100$ Hz and $EIRP = 14$ dBm.	43
1.8	LoRa CSS modulation; raw up chirps representation for $SF \in \{7, \dots, 12\}$ with a bandwidth of 125 kHz. From the left to the right the SF is increased by 1.	45
1.9	BER of CSS in a perfect synchronization case	46
1.10	Range of LoRa uplink transmissions as function of the satellite antenna gain G_{RX} , with $B = 125$ kHz and $EIRP = 14$ dBm.	47
1.11	BER of possible modulations used in LR-FHSS.	50
1.12	Geographical distribution of the industrial IoT LEO constellation projects	51
2.1	Symbol \rightarrow chirp association process - (a) up raw chirp - (b) process principle - (c) associated chirp.	58
2.2	Illustration of LoRa PHY transmission and reception chains [70].	62
2.3	Time desynchronization illustration	63
2.4	Result of $\sqrt{M} Y[k, p] $ when $S_p = 0$ ($SF = 7$) without AWGN for different CFO values.	65
2.5	Spectrogram of the LoRa frame obtained by recording real LoRa data, using raw up chirps in the preamble	68

2.6	Rx Frequency error Tolerance for $SF=7$, a bandwidth of 125kHz, 25°C	73
2.7	Comparison of bit error probabilities of LoRa and DCSS technologies before channel decoding.	77
2.8	Impact of synchronization errors on the BER of DCSS with $SF = 7$	78
2.9	Robustness of DCSS against Doppler rate with $SF = 12$, $B = B_{ref}$ and $N_{pay} = 51$ bytes.	79
2.10	Comparison of robustness of CSS and DCSS technologies to DR over AWGN channel with $SF = 12$, $B = B_{ref}$ and $N_{pay} = 51$ bytes.	80
2.11	Spectrogram of the transmitted signal.	81
2.12	Proposed receiver architecture.	87
2.13	Fractional CFO estimation error ϵ_ν	89
2.14	Beginning time estimation ϵ_{n_s}	90
2.15	PER of CSS and DCSS receivers as function of the CFO with $SF = 7$, SNR = -5 dB and $B = B_{ref}$	90
2.16	PER of CSS and DCSS receivers for different DR values, with $SF = 9$, $B = \frac{B_{ref}}{2^3}$, $N_{pay} = 51$ bytes and $CR = 1$	91
2.17	PER evolution of the proposed DCSS receiver with $CR = 3$	92
2.18	Evolution of the SNR (dB) and elevation angle as function of time for Eutelsat satellite.	93
2.20	BER evolution with $SF = 7$ and $B = \frac{B_{ref}}{2^5}$	98
2.19	Time estimation error ϵ_{n_s} with $SF = 7$ and $B = \frac{B_{ref}}{2^5}$	98
3.1	interference model between UNB and CSS symbols.	103
3.2	Impact of a UNB signal on LoRa-like communication - $SF = 10$, $B = 125$ kHz, $B_{nb} = 100$ Hz and $\gamma_l = 10 \log_{10}(\frac{P}{P_{nb}})$	107
3.3	Impact of UNB interference on LoRa-like $\frac{E_b}{N_0}$ sensitivity threshold Γ_l as function of $\gamma_l = 10 \log_{10}(\frac{P_{wb}}{\sum_{i=1}^{N_{int}} P_{nb,i}})$ - $SF = 10$	108
3.4	Result of the FFT in the presence of same- SF interference with SIR = 3 dB, $SF = 7$ and $L_\tau = 55$	113
3.5	SNR threshold for a target FER of 10^{-1} as a function of the SIR for a packet length of $N_{pay} = 20$ LoRa symbols for $SF = 7$ for coherent and non-coherent receiver [108].	113
3.6	Test-bed for U LoRa transmissions simultaneously received by a LEO satellite.	116
3.7	LoRa-Like symbol detection principle.	118

3.8	Result of the FFT processing when the preamble of the strongest signal is superimposed with two interfering signals ($U_p = 3$).	120
3.9	Preamble detection process ($U = 3$).	121
3.10	Adopted algorithm.	126
3.11	Start of frame detection with $SF = 12$ and $U = 3$	127
3.12	Evolution of the de-chirped block with $PR = 3$ dB, $SF = 12$ and $U = 3$ - (a) initial state - (b) after two iterations.	128
3.13	BER evolution with $PR = 6$ dB, $SF = 12$ and $U = 3$	129
3.14	BER evolution with $PR = 3$ dB, $SF = 12$ and $U = 3$	130
3.15	BER evolution with $PR = 6$ dB, $SF = 9$ and $U = 3$	131
3.16	BER evolution with $PR = 6$ dB, $SF = 7$ and $U = 3$	131
3.17	BER evolution of the weakest signal with $SF = 12$	132
3.18	Test-bed: Three LoRa node transmitting and one USRP SDR device receiving data.	133
3.19	Result of the FFT - (a) synchronization on the strongest signal - (b) strongest signal cancellation - (c) synchronization on the second strongest signal.	134
3.20	Receive Windows - Class A LoRaWAN	136
3.21	Observation used to demodulate a symbol when $\delta n_{1,2} = M/2$ and $SF = 12$	140
3.22	BER curves for node 1 and 2, $SF = 7$ and perfect time/frequency synchronizations	141
3.23	PER curves for node 1 and 2, $SF = 7$ and perfect time/frequency synchronizations	142
3.24	BER curves for node 2, different SF_s , $CR = 3$, no SIC ($PR=0$ dB) and perfect time/frequency synchronizations unless stated otherwise	143
3.25	BER curves for node 1 and 2, $SF = 12$ and perfect time/frequency synchronizations unless stated otherwise	144
3.26	Result of $T(k, p)$, in the case without interference, allowing to detect received signals with $SF = 7$, $B_p = 7.8$ kHz and $N_p = 8$	148
3.27	Result of $T(k, p)$ allowing to detect received signals with $SF = 7$, $B_p = 7.8$ kHz and $N_p = 8$	149
3.28	Result of $T(k, p)$ allowing to detect received signals with $SF = 9$, $B_p = 7.8$ kHz and $N_p = 2$ - (a) initial state - (b) after one iteration.	150
3.29	Preamble detection algorithm.	151
3.30	Good detection probabilities for different N_{itr} and α values.	154

3.31 False detection probabilities for different N_{itr} and α values. 154

3.32 Good and false detection probabilities for each SF with section $\alpha = 4$ and
 $N_{itr} = 3$ 155

List of Tables

1.1	NB-IoT Parameters	38
1.2	Receiver sensitivity and link budget for NB-IoT transmission.	38
1.3	Sigfox Parameters	42
1.4	Receiver sensitivity for each SF ,	45
1.5	Link budget for LoRa signal with $B = 125$ kHz and EIRP = 14 dBm.	46
1.6	LR-FHSS main specifications and parameters for EU and US regions [60, Table. 1].	48
1.7	Industrial IoT LEO Deployments	53
1.8	Related works comparison	55
2.1	Simulation parameters	88
2.2	Receiver sensitivity S dBm for different SF and B values	93
3.1	SINR threshold in dB [11].	110
3.2	Simulation parameters	127
3.4	Preamble configurations	152
3.5	Simulation parameters	153

Bibliography

- [1] Eutelsat, “Satellite IOT: A Compliment To Cellular,” 2020. [Online]. Available: <https://www.eutelsat.com/en/blog/satellite-iot-complementing-cellular.html>
- [2] Swarm. [Online]. Available: <https://swarm.space/>
- [3] Semtech, “LoRa modem design guide: Sx1272/3/6/7/8,” 2013. [Online]. Available: <https://www.semtech.com/>
- [4] —, “Semtech and Swarm Deliver Satellite Communications With LoRa,” 2021. [Online]. Available: <https://fr.semtech.com/company/press/semtech-and-swarm-deliver-satellite-communications-with-lora>
- [5] Sigfox, “Sigfox - The Global Communications Service Provider for the Internet of Things (IoT),” 2018. [Online]. Available: <https://www.sigfox.com/en>
- [6] —, “Admiral LEO World-wide coverage service of satellite and terrestrial IoT,” 2019. [Online]. Available: https://www.sigfox.com/sites/default/files/2019-11/Flyer_sigfoxLEO.pdf
- [7] D. Zucchetto and A. Zanella, “Uncoordinated access schemes for the iot: Approaches, regulations, and performance,” *IEEE Communications Magazine*, vol. 55, no. 9, pp. 48–54, 2017.
- [8] A. A. Boulogeorgos, P. D. Diamantoulakis, and G. K. Karagiannidis, “Low power wide area networks (lpwans) for internet of things (iot) applications: Research challenges and future trends,” *CoRR*, vol. abs/1611.07449, 2016. [Online]. Available: <http://arxiv.org/abs/1611.07449>
- [9] O. Afisiadis, “Physical layer aspects of lora and full-duplex wireless transceivers,” Ph.D. dissertation, École Polytechnique Fédérale de Lausanne, 2020.
- [10] IEEE Spectrum, “Satellites Can Be a Surprisingly Great Option for IoT,” 2021. [Online]. Available: <https://spectrum.ieee.org/satellites-great-option-iot>

- [11] J. Markkula, K. Mikhaylov, and J. Haapola, "Simulating lorawan: On importance of inter spreading factor interference and collision effect," in *ICC 2019 - 2019 IEEE International Conference on Communications (ICC)*, May 2019, pp. 1–7.
- [12] D. Magrin, M. Centenaro, and L. Vangelista, "Performance evaluation of lora networks in a smart city scenario," in *2017 IEEE International Conference on Communications (ICC)*, 2017, pp. 1–7.
- [13] C. Goursaud and J.-M. Gorce, "Dedicated networks for iot: Phy / mac state of the art and challenges," *EAI Endorsed Transactions on Internet of Things*, vol. 1, p. 150597, 10 2015.
- [14] Chris Daehnick, Isabelle Klinghoffer, Ben Maritz, and Bill Wiseman, "Large LEO satellite constellations: Will it be different this time?" 2020. [Online]. Available: <https://www.mckinsey.com/industries/aerospace-and-defense/our-insights/large-leo-satellite-constellations-will-it-be-different-this-time>
- [15] Tariq Malik, "How to spot SpaceXs 60 new Starlink satellites in the night sky," 2019. [Online]. Available: <https://www.space.com/>
- [16] M. Morelli, "Doppler-rate estimation for burst digital transmission," *IEEE Transactions on Communications*, vol. 50, no. 5, pp. 707–710, 2002.
- [17] ScienceDirect, "Low earth orbit." [Online]. Available: <https://www.sciencedirect.com/topics/engineering/low-earth-orbit>
- [18] W. Emery and A. Camps, "Chapter 7 - orbital mechanics, image navigation, and cartographic projections," in *Introduction to Satellite Remote Sensing*, W. Emery and A. Camps, Eds. Elsevier, 2017, pp. 565–596. [Online]. Available: <https://www.sciencedirect.com/science/article/pii/B9780128092545000075>
- [19] H. D. Curtis, "Orbital mechanics for engineering students (fourth edition)," ser. Aerospace Engineering. Butterworth-Heinemann, 2020, p. iv. [Online]. Available: <http://www.sciencedirect.com/science/article/pii/B9780081021330099852>
- [20] Z. Katona and A. Donner, "On mean visibility time of non-repeating satellite orbits," in *2008 IEEE International Workshop on Satellite and Space Communications*, 2008, pp. 247–251.
- [21] —, "On mean visibility time of non-repeating satellite orbits," 11 2008, pp. 247 – 251.

- [22] C. Cao and S. Zhai, “The influence of LEO satellite doppler effect on LoRa modulation and its solutio,” *Journal of Physics: Conference Series*, vol. 1883, no. 1, p. 012071, apr 2021. [Online]. Available: <https://doi.org/10.1088/1742-6596/1883/1/012071>
- [23] I. Ali, N. Al-Dhahir, and J. E. Hershey, “Doppler characterization for leo satellites,” *IEEE Transactions on Communications*, vol. 46, no. 3, pp. 309–313, March 1998.
- [24] D. Barbari, J. Vukovi, and D. Babic, “Link budget analysis for a proposed cubesat earth observation mission,” in *2018 41st International Convention on Information and Communication Technology, Electronics and Microelectronics (MIPRO)*, 2018, pp. 0133–0138.
- [25] G. Maral and M. Bousquet, *A Satellite Communication Systems: Systems, Techniques and Technology*. 5th ed. John Wiley and Sons, 2009.
- [26] U. Raza, P. Kulkarni, and M. Sooriyabandara, “Low power wide area networks: An overview,” *IEEE Communications Surveys Tutorials*, vol. 19, no. 2, pp. 855–873, 2017.
- [27] —, “Low Power Wide Area Networks: An overview,” vol. 19, no. 2, pp. 855–873, Jan. 2017.
- [28] O. Afisiadis, A. Burg, and A. Stimming, *Physical Layer Aspects of LoRa and Full-Duplex Wireless Transceivers*. Ecole Polytechnique Fédérale de Lausanne, 2020. [Online]. Available: <https://books.google.fr/books?id=6vXHzQEACAAJ>
- [29] B. Reynders and S. Pollin, “Chirp spread spectrum as a modulation technique for long range communication,” in *2016 Symposium on Communications and Vehicular Technologies (SCVT)*, 2016, pp. 1–5.
- [30] M. Saelens, J. Hoebeke, A. Shahid, and E. D. Poorter, “Impact of eu duty cycle and transmission power limitations for sub-ghz lpwan srds: an overview and future challenges,” *EURASIP Journal on Wireless Communications and Networking*, vol. 2019, pp. 1–32, 2019.
- [31] ETSI, “Electromagnetic compatibility and radio spectrum matters (erm); short range devices (srd); radio equipment to be used in the 25 mhz to 1 000 mhz frequency range with power levels ranging up to 500 mw; part 1: Technical characteristics and test methods,” *Tech. Rep. EN 300 220-1 V2.4.1*, Jan. 2012.
- [32] G. Ferré and M. A. Ben Temim, “A dual waveform differential chirp spread spectrum transceiver for leo satellite communications,” in *ICC 2021 - IEEE International Conference on Communications*, 2021, pp. 1–6.

- [33] B. Chaudhari, M. Zennaro, and S. Borkar, "Lpwan technologies: Emerging application characteristics, requirements, and design considerations," *Future Internet*, vol. 12, p. 46, 03 2020.
- [34] R. Ratasuk, N. Mangalvedhe, Y. Zhang, M. Robert, and J.-P. Koskinen, "Overview of narrowband iot in lte rel-13," in *2016 IEEE Conference on Standards for Communications and Networking (CSCN)*, 2016, pp. 1–7.
- [35] M. Centenaro, C. E. Costa, F. Granelli, C. Sacchi, and L. Vangelista, "A survey on technologies, standards and open challenges in satellite iot," *IEEE Communications Surveys Tutorials*, vol. 23, no. 3, pp. 1693–1720, 2021.
- [36] M. Conti, S. Andrenacci, N. Maturo, S. Chatzinotas, and A. Vanelli-Coralli, "Doppler impact analysis for nb-iot and satellite systems integration," in *ICC 2020 - 2020 IEEE International Conference on Communications (ICC)*, 2020, pp. 1–7.
- [37] K. Mekki, E. Bajic, F. Chaxel, and F. Meyer, "A comparative study of lpwan technologies for large-scale iot deployment," vol. 5, pp. 1–7, 03 2019.
- [38] GSMA, "What is the Difference in Data Throughput between LTE-M/NB-IoT and 3G or 4G?" [Online]. Available: <https://www.gsma.com/iot/resources/what-is-the-difference-in-data-throughput-between-lte-m-nb-iot-and-3g-or-4g/>
- [39] S. Dey, A. Professor, and B. B. Sahoo, "Link budget of leo satellite (sky bridge) for communication operated at ku band frequency range (12-14) ghz."
- [40] ESA. [Online]. Available: https://www.esa.int/ESA_Multimedia/Images/2020/03/Low_Earth_orbit.
- [41] Z. Zhuang, L. Feng, P. Yu, and W. Li, "Uplink resource scheduling for power wireless private network based on nb-iot and lte hybrid transmission," in *2017 IEEE International Conference on Computational Science and Engineering (CSE) and IEEE International Conference on Embedded and Ubiquitous Computing (EUC)*, vol. 2, 2017, pp. 77–84.
- [42] U. Mengali, "Synchronization techniques for digital receivers," in *Springer*, 1997.
- [43] S. Cluzel, L. Franck, J. Radzik, S. Cazalens, M. Dervin, C. Baudoin, and D. Dragomirescu, "3gpp nb-iot coverage extension using leo satellites," in *2018 IEEE 87th Vehicular Technology Conference (VTC Spring)*, 2018, pp. 1–5.
- [44] M. Conti, S. Andrenacci, N. Maturo, S. Chatzinotas, and A. Vanelli-Coralli, "Doppler impact analysis for nb-iot and satellite systems integration," in *ICC 2020 - 2020 IEEE International Conference on Communications (ICC)*, 2020, pp. 1–7.

- [45] Z. Shi, J. Huang, Z. Zhang, and Y. Sang, "Analyze and comment on spectral efficiency of vmsk modulation," in *2006 International Conference on Wireless Communications, Networking and Mobile Computing*, 2006, pp. 1–4.
- [46] S. Zhang, "Spectrum analyses of unb modulation formats," in *2013 3rd International Conference on Consumer Electronics, Communications and Networks*, 2013, pp. 594–597.
- [47] Sigfox, "Sigfox Technical Overview," 2018. [Online]. Available: <https://www.avnet.com/wps/wcm/connect/onesite/03aebfe2-98f7-4c28-be5f-90638c898009/sigfox-technical-overview.pdf?MOD=AJPERESCVID=magVa.NCVID=magVa.NCVID=magVa.N>
- [48] M. Anteur, N. Thomas, V. Deslandes, and A.-L. Beylot, "On the performance of unb for machine-to-machine low earth orbit (leo) satellite communications," *International Journal of Satellite Communications and Networking*, vol. 37, 10 2018.
- [49] T. J. Abatzoglou, "Fast maximum likelihood joint estimation of frequency and frequency rate," *IEEE Transactions on Aerospace and Electronic Systems*, vol. AES-22, no. 6, pp. 708–715, 1986.
- [50] LoRa Alliance, "LoRaWAN[®] Specification v1.1," 2017. [Online]. Available: <https://loralliance.org/resource-hub/lorawanr-specification-v11>
- [51] Semtech, "What are LoRa and LoRaWAN?" [Online]. Available: <https://loradevelopers.semtech.com/documentation/tech-papers-and-guides/lora-and-lorawan>
- [52] G. Ferré and A. Giremus, "LoRa Physical Layer Principle and Performance Analysis," in *2018 25th IEEE International Conference on Electronics, Circuits and Systems (ICECS)*, Dec 2018, pp. 65–68.
- [53] "Semtech sx1262." [Online]. Available: <https://www.semtech.com/products/wireless-rf/lora-core/sx1262>
- [54] T. Elshabrawy and J. Robert, "Analysis of BER and Coverage Performance of LoRa Modulation under Same Spreading Factor Interference," in *2018 IEEE 29th Annual International Symposium on Personal, Indoor and Mobile Radio Communications (PIMRC)*, Sep. 2018, pp. 1–6.
- [55] O. Afisiadis, M. Cotting, A. P. Burg, and A. Balatsoukas-Stimming, "Lora symbol error rate under non-chip- and non-phase-aligned interference," *ArXiv*, vol. abs/1905.00439, 2019.

- [56] R. Fernandes, R. Oliveira, M. Luís, and S. Sargento, "On the real capacity of lora networks: The impact of non-destructive communications," *IEEE Communications Letters*, vol. 23, no. 12, pp. 2437–2441, 2019.
- [57] D. Croce, M. Gucciardo, S. Mangione, G. Santaromita, and I. Tinnirello, "Impact of lora imperfect orthogonality: Analysis of link-level performance," *IEEE Communications Letters*, vol. 22, no. 4, pp. 796–799, April 2018.
- [58] G. Colavolpe, T. Foggi, M. Ricciulli, Y. Zanettini, and J. Mediano-Alameda, "Reception of lora signals from leo satellites," *IEEE Transactions on Aerospace and Electronic Systems*, pp. 1–1, 2019.
- [59] LoRa Alliance, "RP2-1.0.2 LoRaWAN Regional Parameters," 2020. [Online]. Available: https://lora-alliance.org/resource_hub/rp2-102-lorawan-regional-parameters/
- [60] G. Boquet, P. Tuset-Peiro, F. Adelantado, T. Watteyne, and X. Vilajosana, "Lr-fhss: Overview and performance analysis," 2020.
- [61] G. Forney, "The viterbi algorithm," *Proceedings of the IEEE*, vol. 61, no. 3, pp. 268–278, 1973.
- [62] Proakis, *Digital Communications 5th Edition*. McGraw Hill, 2007.
- [63] "Lorawan protocol expands network capacity with new long range frequency hopping spread spectrum technology." [Online]. Available: <https://blog.semtech.com/lorawan-protocol-expands-network-capacity-with-new-long-range-frequency-hopping-spread-spectrum-technology>
- [64] [Online]. Available: <https://celestrak.com/satcat/search.php>
- [65] L. Vangelista, "Frequency shift chirp modulation: The lora modulation," *IEEE Signal Processing Letters*, vol. 24, no. 12, pp. 1818–1821, Dec 2017.
- [66] C. Bernier, F. Dehmas, and N. Deparis, "Low complexity lora frame synchronization for ultra-low power software-defined radios," *IEEE Transactions on Communications*, pp. 1–13, 2020.
- [67] O. Seller and N. Sornin, "Low complexity, low power and long range radio receiver," Mar. 7 2018, uS Patent App. 14/170,170. [Online]. Available: <https://patents.google.com/patent/EP3264622B1/en>
- [68] M. Xhonneux, D. Bol, and J. Louveaux, "A low-complexity synchronization scheme for lora end nodes." *arXiv: Signal Processing*, 2019.

- [69] M. Xhonneux, O. Afisiadis, D. Bol, and J. Louveaux, "A low-complexity lora synchronization algorithm robust to sampling time offsets," *IEEE Internet of Things Journal*, pp. 1–1, 2021.
- [70] O. Afisiadis, A. Burg, and A. Balatsoukas-Stimming, "Coded lora frame error rate analysis," 06 2020, pp. 1–6.
- [71] O. Seller and N. Sornin, "Low power long range transmitter," feb. [Online]. Available: <http://www.google.com/patents/US20140219329>
- [72] A. Marquet, N. Montavont, and G. Z. Papadopoulos, "Towards an sdr implementation of lora: Reverse-engineering, demodulation strategies and assessment over rayleigh channel," *Computer Communications*, vol. 153, 02 2020.
- [73] M. Knight and B. Seeber, "Decoding LoRa: Realizing a Modern LPWAN with SDR," *Proceedings of the GNU Radio Conference*, vol. 1, no. 1, 2016. [Online]. Available: <https://pubs.gnuradio.org/index.php/grcon/article/view/8>
- [74] J. Tapparel, O. Afisiadis, P. Mayoraz, A. Balatsoukas-Stimming, and A. Burg, "An open-source lora physical layer prototype on gnu radio," in *2020 IEEE 21st International Workshop on Signal Processing Advances in Wireless Communications (SPAWC)*, 2020, pp. 1–5.
- [75] M. A. B. Temim, G. Ferré, B. Laporte-Fauret, D. Dallet, B. Minger, and L. Fuché, "An enhanced receiver to decode superposed lora-like signals," *IEEE Internet of Things Journal*, pp. 1–13, 2020.
- [76] J. Tapparel, O. Afisiadis, P. Mayoraz, A. Balatsoukas-Stimming, and A. Burg, "An open-source lora physical layer prototype on gnu radio," in *2020 IEEE 21st International Workshop on Signal Processing Advances in Wireless Communications (SPAWC)*, 2020, pp. 1–5.
- [77] T. M. Schmidl and D. Cox, "Robust frequency and timing synchronization for ofdm," *IEEE Trans. Commun.*, vol. 45, pp. 1613–1621, 1997.
- [78] B. Quinn, "Estimation of frequency, amplitude, and phase from the dft of a time series," *IEEE Transactions on Signal Processing*, vol. 45, no. 3, pp. 814–817, 1997.
- [79] E. Jacobsen and P. Kootsookos, "Fast, accurate frequency estimators [dsp tips amp; tricks]," *IEEE Signal Processing Magazine*, vol. 24, no. 3, pp. 123–125, 2007.

- [80] C. Yang and G. Wei, "A noniterative frequency estimator with rational combination of three spectrum lines," *IEEE Transactions on Signal Processing*, vol. 59, no. 10, pp. 5065–5070, 2011.
- [81] Semtech, 2019, [accessed on 28.03.2019]. [Online]. Available: https://www.semtech.com/uploads/documents/PicoCellGW_V1.0_RF_Performance_Report_V1.0.pdf
- [82] Y. Liao, "Phase and frequency estimation: High-accuracy and low-complexity techniques," 2011.
- [83] G. Colavolpe, T. Foggi, M. Ricciulli, Y. Zanettini, and J. Mediano-Alameda, "Reception of lora signals from leo satellites," *IEEE Transactions on Aerospace and Electronic Systems*, pp. 1–1, 2019.
- [84] Eutelsat. [Online]. Available: <https://www.eutelsat.com/en/satellites/leo-fleet.html>
- [85] M. A. Ben Temim, G. Ferré, and R. Tajan, "A novel approach to enhance the robustness of lora-like phy layer to synchronization errors," in *GLOBECOM 2020 - 2020 IEEE Global Communications Conference*, 2020, pp. 1–6.
- [86] LoRa Alliance, "LoRaWAN 1.1 Regional Parameters," 2017. [Online]. Available: https://lora-alliance.org/sites/default/files/2018-04/lorawantm_regional_parameters_v1.1rb_-_final.pdf
- [87] A. Mitra, "On pseudo-random and orthogonal binary spreading sequences," *International Journal of Electronics and Communication Engineering*, vol. 2, no. 12, pp. 2836 – 2843, 2008. [Online]. Available: <https://publications.waset.org/vol/24>
- [88] Z. Matouek, M. Babjak, and J. Ochodnický, "Walsh-hadamard sequences for binary encoding of radar signals," in *International Conference on Military Technologies (ICMT) 2015*, 2015, pp. 1–6.
- [89] M. A. Ben Temim, G. Ferré, and R. Tajan, "Analysis of the coexistence of ultra narrow band and spread spectrum technologies in ism bands," in *Ubiquitous Networking*. Springer International Publishing, 2020, pp. 56–67.
- [90] M. C. Bor, U. Roedig, T. Voigt, and J. M. Alonso, "Do lora low-power wide-area networks scale?" in *Proceedings of the 19th ACM International Conference on Modeling, Analysis and Simulation of Wireless and Mobile Systems*, ser. MSWiM '16. New York, NY, USA: Association for Computing Machinery, 2016, p. 5967. [Online]. Available: <https://doi.org/10.1145/2988287.2989163>

- [91] T. Voigt, M. Bor, U. Roedig, and J. Alonso, “Mitigating inter-network interference in lora networks,” ser. EWSN 17. USA: Junction Publishing, 2017, p. 323328.
- [92] J. Haxhibeqiri, F. Van den Abeele, I. Moerman, and J. Hoebeke, “Lora scalability: A simulation model based on interference measurements,” *Sensors*, vol. 17, no. 6, 2017. [Online]. Available: <https://www.mdpi.com/1424-8220/17/6/1193>
- [93] P. Ferrari, A. Flammini, M. Rizzi, E. Sisinni, and M. Gidlund, “On the evaluation of lorawan virtual channels orthogonality for dense distributed systems,” in *2017 IEEE International Workshop on Measurement and Networking (MN)*, 2017, pp. 1–6.
- [94] D. Croce, M. Gucciardo, I. Tinnirello, D. Garlisi, and S. Mangione, “Impact of spreading factor imperfect orthogonality in lora communications,” in *Digital Communication. Towards a Smart and Secure Future Internet*, A. Piva, I. Tinnirello, and S. Morosi, Eds. Cham: Springer International Publishing, 2017, pp. 165–179.
- [95] D. Croce, M. Gucciardo, S. Mangione, G. Santaromita, and I. Tinnirello, “Impact of lora imperfect orthogonality: Analysis of link-level performance,” *IEEE Communications Letters*, vol. 22, no. 4, pp. 796–799, 2018.
- [96] L. Feltrin, C. Buratti, E. Vinciarelli, R. De Bonis, and R. Verdone, “Lorawan: Evaluation of link- and system-level performance,” *IEEE Internet of Things Journal*, vol. 5, no. 3, pp. 2249–2258, 2018.
- [97] T. Elshabrawy and J. Robert, “Capacity planning of lora networks with joint noise-limited and interference-limited coverage considerations,” *IEEE Sensors Journal*, vol. 19, no. 11, pp. 4340–4348, 2019.
- [98] —, “Capacity planning of lora networks with joint noise-limited and interference-limited coverage considerations,” *IEEE Sensors Journal*, vol. 19, no. 11, pp. 4340–4348, 2019.
- [99] A. Mahmood, E. Sisinni, L. Guntupalli, R. Rondón, S. A. Hassan, and M. Gidlund, “Scalability analysis of a lora network under imperfect orthogonality,” *IEEE Transactions on Industrial Informatics*, vol. 15, no. 3, pp. 1425–1436, 2019.
- [100] G. Zhu, C.-H. Liao, M. Suzuki, Y. Narusue, and H. Morikawa, “Evaluation of lora receiver performance under co-technology interference,” in *2018 15th IEEE Annual Consumer Communications Networking Conference (CCNC)*, 2018, pp. 1–7.
- [101] U. Noreen, L. Clavier, and A. Bounceur, “LoRa-like CSS-based PHY layer, Capture Effect and Serial Interference Cancellation,” in *European Wireless 2018; 24th European Wireless Conference*, May 2018, pp. 1–6.

- [102] N. E. Rachkidy, A. Guitton, and M. Kaneko, “Decoding Superposed LoRa Signals,” *CoRR*, vol. abs/1804.00503, 2018. [Online]. Available: <http://arxiv.org/abs/1804.00503>
- [103] Z. Qin and J. A. McCann, “Resource efficiency in low-power wide-area networks for iot applications,” in *GLOBECOM 2017 - 2017 IEEE Global Communications Conference*, 2017, pp. 1–7.
- [104] B. Reynders, W. Meert, and S. Pollin, “Power and spreading factor control in low power wide area networks,” in *2017 IEEE International Conference on Communications (ICC)*, 2017, pp. 1–6.
- [105] M. Chiani and A. Elzanaty, “On the lora modulation for iot: Waveform properties and spectral analysis,” *CoRR*, vol. abs/1906.04256, 2019. [Online]. Available: <http://arxiv.org/abs/1906.04256>
- [106] O. Afisiadis, M. Cotting, A. Burg, and A. Balatsoukas-Stimming, “On the error rate of the lora modulation with interference,” *IEEE Transactions on Wireless Communications*, vol. 19, no. 2, pp. 1292–1304, 2020.
- [107] O. Afisiadis, M. Cotting, A. Burg, and A. Balatsoukas-Stimming, “Lora symbol error rate under non-aligned interference,” in *2019 53rd Asilomar Conference on Signals, Systems, and Computers*, 2019, pp. 1957–1961.
- [108] O. Afisiadis, S. Li, A. Burg, and A. Balatsoukas-Stimming, “On the advantage of coherent lora detection in the presence of interference,” 10 2020.
- [109] M. Ni, M. Jafarizadeh, and R. Zheng, “On the effect of multi-packet reception on redundant gateways in lorawans,” in *ICC 2019 - 2019 IEEE International Conference on Communications (ICC)*, May 2019, pp. 1–6.
- [110] Y. Qian, L. Ma, and X. Liang, “Symmetry chirp spread spectrum modulation used in leo satellite internet of things,” *IEEE Communications Letters*, vol. 22, no. 11, pp. 2230–2233, 2018.
- [111] —, “The performance of chirp signal used in leo satellite internet of things,” *IEEE Communications Letters*, vol. 23, no. 8, pp. 1319–1322, 2019.
- [112] A. A. TESFAY, E. P. SIMON, G. FERRÉ, and L. CLAVIER, “Serial interference cancellation for improving uplink in lora-like networks,” in *2020 IEEE 31st Annual International Symposium on Personal, Indoor and Mobile Radio Communications*, 2020, pp. 1–6.

- [113] A. A. Tesfay, E. P. Simon, I. Nevat, and L. Clavier, “Multiuser detection for downlink communication in lora- like networks,” *IEEE Access*, vol. 8, pp. 199 001–199 015, 2020.
- [114] R. Ghanaatian, O. Afisiadis, M. Cotting, and A. Burg, “Lora digital receiver analysis and implementation,” *CoRR*, vol. abs/1811.04146, 2018. [Online]. Available: <http://arxiv.org/abs/1811.04146>
- [115] G. Ferré and E. P. Simon, “Packet collision analysis when heterogeneous unlicensed IoT technologies coexist,” *IET Networks*, May 2018. [Online]. Available: <http://digital-library.theiet.org/content/journals/10.1049/iet-net.2018.0026>
- [116] G. Ferré, F. Rivet, R. Tajan, and E. Kerhervé, “Design and Deployment of an IoT Network Based on LoRa,” in *EAEIE (European Association for Education in Electrical and Information Engineering)*, Grenoble, France, Jun. 2017.
- [117] Ettus Knowledge Base, “B100 — Ettus Knowledge Base,” 2016. [Online]. Available: <https://kb.ettus.com/index.php?title=B100oldid=2983>
- [118] J. P. Shanmuga Sundaram, W. Du, and Z. Zhao, “A survey on lora networking: Research problems, current solutions, and open issues,” *IEEE Communications Surveys Tutorials*, vol. 22, no. 1, pp. 371–388, 2020.
- [119] STMicroelectronics, “Ultra-low power, high performance, sub-1 GHz transceiver,” 2021. [Online]. Available: <https://www.st.com/resource/en/datasheet/s2-lp.pdf>